Galaxias Satélites en Simulaciones Numéricas: Poblaciones de Fusionados, Sobrevivientes y en Escape

por Laura Virginia Sales

Presentado ante la Facultad de Matemática, Astronomía y Física como parte de los requerimientos para la obtención del grado de Doctor en Astronomía de la

UNIVERSIDAD NACIONAL DE CORDOBA
Abril, 2007

Director: Dr. Diego G. Lambas

Laura Virginia Sales: *Satellite Galaxies in Numerical Simulations: Merged, Surviving and Escaping Populations*

April 2007

SATELLITE GALAXIES IN NUMERICAL SIMULATIONS: MERGED, SURVIVING AND ESCAPING POPULATIONS

Laura Virginia Sales

UNIVERSIDAD NACIONAL DE CORDOBA
Argentina, April 2007

Y morirme contigo si te matas
y matarme contigo si te mueres
porque el amor cuando no muere mata
porque amores que matan nunca mueren
(Joaquín Sabina, Contigo)

RESÚMEN

Se analizan las propiedades principales de la población de satélites de galaxias primarias $\sim L_*$ en el modelo ΛCDM usando simulaciones cosmológicas N−cuerpos/SPH de alta resolución y la muestra semi−analítica de galaxias de la simulación *Millennium Run*. El análisis está enfocado en el rol fundamental de los satélites en el proceso de formación de galaxias, como asi también en la información que nos ofrecen como trazadores de la materia oscura de los halos que habitan. Se encuentra que existe un sesgo (*bias*) muy pequeño entre las posiciones y la cinemática de las partículas de materia oscura y la población de satélites sobrevivientes. La posición de los satélites puede ser utilizada para inferir la distribución radial de materia oscura en los halos primarios para distancias $r > 0.2r_{vir}$. En projección, se espera a partir de catálogos sintéticos (*mock catalogs*) un perfil radial proyectado de número de satélites consistente con una ley de potencia con pendiente $\alpha = -1.5$. Se seleccionaron satélites del catálogo Sloan Digital Sky Survey encontrando $\alpha = -1.4$, en buen acuerdo con las predicciones teóricas extraídas de las simulaciones. La dispersión de velocidad de los satélites es también un buen indicador de la velocidad virial del halo primario. Se encuentra $\sigma_{sat}/V_{vir} = 0.9 \pm 0.2$, que aplicado al Grupo Local da: $V_{vir}^{MW} \sim 109 \pm 22$ km/s y $V_{vir}^{M31} \sim 138 \pm 35$ km/s para la Vía Láctea y la galaxia de Andrómeda respectivamente, sugiriendo que la velocidad virial en las galaxias podría ser sustancialmente menor que la velocidad de rotación de sus discos.

Por otro lado, existen diferencias apreciables entre la población de satélites y el halo estelar de las galaxias, el cual consiste principalmente de los *escombros* estelares de satélites que han sido destruídos. Estas estrellas muestran una distribución radial más concentrada y movimientos orbitales más eccéntricos. La población de satélites *sobrevivientes* es diferente de los satélites *fusionados* que construyeron la galaxia, y muestra un sesgo apreciable hacia objetos de baja masa que han sido acretados más recientemente por la galaxia. Nuestros resultados pueden reconciliar las diferencias sistemáticas entre las estrellas en el halo de la Vía Láctea y los satélites de nuestra Galaxia.

Los halos primarios son ambientes hostiles para los satélites, quienes sufren modificaciones fuertes de sus masas y órbitas iniciales. La fricción dinámica con el halo primario circulariza las órbitas de los satélites y contínuamente reduce sus apocentros. Sin embargo, alrededor de un tercio de la población de satélites *sobrevivientes* se encuentra en órbitas no ortodoxas, con apocentros que exceden sus radios de *turn−around*. Estos satélites intrigantes son mayormente el miembro más débil de un par, y fueron expulsados a dichas órbitas de altas energías debido a mecanismos de interación de tres cuerpos durante sus primeros pasajes por el pericentro. Se especula sobre la posibilidad de que algunas galaxias enanas del Grupo Local deban sus cinemáticas peculiares a este proceso, como el caso de Leo I, las aisladas Cetus y Tucana como asi también los satélites con altas velocidades descubiertos recientemente

alrededor de Andrómeda: AndXII y AndXIV.

ABSTRACT

We analyze the main properties of the satellite population of L_* primary galaxies in the ΛCDM model using high resolution N−body/gasdynamical simulations and the semi−analytical sample of galaxies from the *Millennium Run* simulation. We focus on the fundamental role of satellites in the galaxy formation process as well as on the important insights they offer as tracers of the dark matter in host halos. We find that there are little spatial or kinematical biases between the dark matter particles of hosts and their surviving satellite population. Positions of satellites may be used to infer the dark matter radial distribution of host halos in distances $r > 0.2r_{vir}$. In projection, we expect from simulated mock catalogs a power−law for the satellite *projected* number density profile with slope $\alpha = -1.5$. We select satellites from the Sloan Digital Sky Survey finding $\alpha = -1.4$, in good agreement with the theoretical predictions from simulations. The velocity dispersion of satellites is also a good indicator of the virial velocity of their host. We find $\sigma_{sat}/V_{vir} = 0.9 \pm 0.2$, that applied to the Local Group galaxies gives: $V_{vir}^{MW} \sim 109 \pm 22$ km/s and $V_{vir}^{M31} \sim 138 \pm 35$ km/s for the Milky Way and Andromeda galaxy respectively, suggesting that the virial velocities of galaxies might be substantially lower than the rotation speed of their disk components.

On the other hand, substantial differences exist between the satellite population and the stellar halo of galaxies, which mainly consists of the stellar debris of disrupted satellites. These stars show a more concentrated radial distribution and more eccentric orbital motions. The *surviving* satellite population is not reminiscent of the *merged* satellites that build-up the galaxy, but shows a significant bias toward low−mass systems that have been accreted more recently by the galaxy. Our results can reconcile the systematic differences between stars in the halo of the Milky Way and in the Galactic satellites.

Host halos are hostile environments for satellites who suffer strong modifications to their initial masses and orbits. Dynamical friction with the host halo circularize the satellite orbits and also continuously shrinks their apocenters. Nevertheless, about *one-third* of the *surviving* satellites are on unorthodox orbits, with apocenters that exceed their turn−around radius. This intriguing satellites are typically the faint member of a pair that were ejected onto highly−energetic orbits due to three−body interaction mechanisms during their first pericenter passage. We speculate that some Local Group dwarfs owe their outstanding dynamics to this process, such as LeoI, the isolated Cetus and Tucana as well as the newly−discovered high−speed satellites around Andromeda: AndXII and AndXIV.

Gracias a la vida que me ha dado tanto
Me dio dos luceros que cuando los abro
Perfecto distingo lo negro del blanco
Y en el alto cielo su fondo estrellado

ACKNOWLEDGMENTS

Un simple "gracias" palidece frente a lo inmenso que aportaron todos ustedes en mi vida. Sepan que lo que he escrito a continuación es solo una pequeñísima fracción de la gratitud y cariño que en realidad siento. Como imposible escribir la luz de una mirada, el sonido de un beso, el calor de un abrazo, he aqui algunas frases que intenten demostrar lo indemostrable. Principalmente agradezco a:

Muy especialmente, al Dr. Julio Navarro, a quien debo gran parte de esta tesis. Gracias "jefe" por tu paciencia y dedicación, por demostrarme que lo importante siempre es *aprender* algo de cada cosa que hacemos, y que aun asi queda un mar inmenso de cosas por sorprendernos. Gracias por enseñarme que solo el máximo esfuerzo garantiza plena satisfacción al final, por el estímulo a superarme dia a dia, por las ganas, la pasión y el entusiasmo infinito que siempre me contagiás. Me quedo con el placer de estos tres años de trabajo juntos, y con mi admiración y respeto infinito que te supiste ganar.

Al Dr. Mario Abadi, también encargado de guiarme estos años. Por su disponibilidad a mis continuas preguntas y su predisposición a ayudarme. Por ser "malo" algunas veces e incentivarme a mejorar. Gracias también por tus correcciones y comentarios en la tesis, que en cierta forma evitaron mi colapso mental en los ultimos dias... Por hacerme sentir fuerte, por haber crecido y aprendido muchísimo a tu lado, por los cafe con leche batidos de todas las mañanas y por sobretodo Abadi, gracias por tu fe en mi.

A Diego, por su generosidad cuando termine la Licenciatura y quise entrar al mundo de las simulaciones numéricas, por darme la libertad de hacer lo que realmente me gusta y me hace feliz. Tambien gracias Dgl por tu esfuerzo incondicional por el IATE y por tu apoyo emocional y consejos en épocas difíciles.

Tambien a: J.J. Clariá, Hernán Muriel, Carlos Valotto y Mariano Domínguez por su buena predisposición a mis preguntas y dudas científicas. A Ariel Z. y Manuel Merchán por ayudarme en cuestiones computacionales.

A gente del IATE que pude conocer quizás un poco más este ultimo tiempo y en quienes encontré mucha ayuda, confianza y amistad. Principalmente a Vale, por su preocupación acerca de mi obsesión por el trabajo, por su compañía y por escucharme cada vez que necesité hablar... A Julián, por algunas charlas y consejos que me hicieron muy bien; gracias también por estar dispuesto a ayudarme con el Binney & Tremaine y por cada uno de tus esfuerzos Martínez en convertirme en xeneize (aunque muy infructíferos claro...). A Ariel Z. por su musica que me acompañó en las

largas y solitarias noches de trabajo en la oficina. Tambien a Anita por aguantarme en su oficina este ultimo tiempo y soportar el estrés de los dias finales previos a la entrega de la tesis. Finalmente a Cin, Euge y Manuel y todos los anteriores por lindas reuniones y risas compartidas.

A Ele, por supuesto!, amiga del alma y compañera en los primeros 3 años de estudio en la Famaf. Gracias por tu incondicionalidad y apoyo, por tus consejos y visión objetiva de la vida.

A mis alumnas de patin del club Ameghino con quienes compartí momentos imborrables, a quienes aprendi a querer y a extrañar locamente. A muchas las vi crecer desde piojitas y llegar a lo mas alto, y dar todo por ello. Muchas me llenaron de orgullo en cada torneo, con cada esfuerzo, con cada meta cumplida. Guardo en mi corazón los sonidos de sus risas, la picardía de sus ojitos, el cariño de sus abrazos. Las voy a extrañar millones chicas, pero un poquito de ustedes les juro se quedará conmigo siempre. También gracias a la familia Cativelli, a Mary, Carlos, Sabri, Dani y Fede por ser mis "papas" y "hermanitos" postizos, por el cariño inmenso recibido.

To people in the Kapteyn Institute, where I found so much kindness and friendship. I would like to thank specially to my friends that didn't forget me in spite of the distance: to Rajat, Mati, Vibor, Panos, JP, Pablo and Peter, who made my stay there a great time plenty of happy moments, smiles and lot of fun. I have really missed you all this time and I look forward to see all you again very soon!

My special thanks to macha (Rajat), who shares with me a huge passion for astronomy and from who I enjoyed all his comments and scientific disscusions. Also for listening and helping me in the days I was sad like crazy, either in Groningen or here, after I came back to Córdoba. Macha, thanks for all the chats and phonecalls to machi in the moments she needed you!.

I am deeply grateful to Dr. Simon White, Dr. Darren Croton, Dr. Matthias Steinmetz and Dr. Amina Helmi for several suggestions and disscusions from which I really learned a lot.

Y a vos mami, por tu paciencia y fortaleza; por estar siempre conmigo y mimarme. Perdón por mis silencios y ojos tristes, fue siempre importante para mi tenerte a mi lado aunque muchas veces no lo dijera.

CONTENTS

LIST OF FIGURES

LIST OF TABLES

1 INTRODUCTION

Galaxies are fascinating objects that combine the beauty of their appearance with the complexity of the processes that drive their formation and evolution. Since their discovery galaxies have challenged our theories of formation of structures in the Universe, seducing and capturing our attention with the questions they pose and mysteries they harbor. Less than a century ago we gave our first steps towards the understanding of galaxies with the famous Shapley−Curtis debate (1920)[1]. The confirmation that "nebulae" were indeed objects like our Galaxy but lying beyond its limits promted joint observational and theoretical efforts designed to improve our knowledge of these *Island Universes*.

1.1 Galaxies in the ΛCDM scenario

The galaxies we know today are intricate systems of stars, gas and dust inhabiting a much extended and massive dark matter halo. We believe that the seeds of present−day galaxies began as very small fluctuations in the almost uniform early Universe. WMAP satellite mission has recently measured such departures from full homogeneity, and reliable estimates of the initial spectrum of density fluctuations have become available (Spergel et al. 2001,2006). Linear theory (Peebles 1980) predicts that these density fluctuations grow under the influence of their self−gravity and eventually became large enough to capture and retain the gas that fueled star formation. *Dissipative* processes cool and precipitate the gas at the bottom of the potential wells provided by the dark matter generating a substantial segregation between the luminous and the dark component of galaxies (White and Rees 1978). On the other hand, *collisionless* physics dominate the mass growth and the clustering of galaxies determining the global distribution of objects in the Universe.

Although the precise nature of the dark matter is still unknown, current observations suggest Cold Dark Matter (CDM) as the favorite model describing our Universe. The mass assembly history of objects in this model is *bottom−up*, meaning that small objects form first and then merge with others to build up the large structures we observe today. Basically, it follows the *Spherical Collapse* prescriptions where a given region around an initial overdensity decouples from the general expansion of the universe, reach their maximum extension (the turnaround radius) and then collapse, virializing as bound objects. Subsequent studies showed that this process has no preferred scale, guaranteeing the self−similarity of dark matter halos. .

As halos are assembled in this hierarchical scenario, the inner regions of early virialized objects often survive accretion onto a larger system, thus originating a

1 During which the existence of other *external* galaxies different from our own was discussed

population of subhalos. The self−similarity mentioned above makes galactic halos look like scaled versions of the cluster−sized ones (Moore et al 1999 , Gao et al 2004 , Diemand et al. 2004). Objects that cross the virial radius of a more massive system are immediately exposed to a hostile environment where the dynamical friction, tidal forces and impulsive collisions could determine their final destiny (the merging with the central host). The fate of subhalos after entering the host depend on intrinsic (central concentrations and masses) as well as on external (infall times, orbit eccentricities, mass of the host) factors that determine whether a given subhalo survives until the present epoch (surviving population) or merges with the central host (merged population). The N−body numerical simulations of Moore et al, Gao et al. and Diemand et al. mentioned before have shown that dark matter halos host at $z = 0$ several hundreds of such surviving subhalos, and that these account for $\sim 10\%$ of the total mass of the system.

These predictions are difficult to reconcile with the ~ 20 satellite galaxies discovered so far around the Milky Way and Andromeda, and other external galaxies. This emphasizes that the mapping between the dark and the luminous components of satellite galaxies is highly non−linear. Possible resolutions of this “satellite crisis” have been discussed by a number of authors, and there is reasonably broad consensus that it originates from inefficiencies in star formation caused by the combined effects of energetic feedback from evolving stars and by the diminished supply of cold gas due to reionization (see, e.g. Kauffmann & White 1993 , Bullotck et al. 2000 , Somerville et al 2001 , Benson et al 2002). These effects combine to reduce dramatically the star formation activity in substructure halos, and can reconcile, under plausible assumptions, the substructure halo mass function with the faint end of the satellite luminosity function (Stoher et al. 2002, Kazantzidis et al. 2004, Peñarrubia et al. 2007) .

Besides their contribution to a better understanding of how galaxy formation proceeds in smaller objects, satellite galaxies may be thought of as the visible fossil relics of the hierarchical process that in the past formed their host galaxy. They are the remnants of the series of accretion events that shaped the primary galaxy; the *surviving* members of a much larger population of satellites that once crossed the virial radius of their host. Sometimes, they also offer us the chance of studying on−going mergers, showing spectacular signatures of disruption. These resulting "tidal−tails" are also important proofs of the hierarchical build−up of galaxies, one of the cornerstones of the currently accepted models for our Universe.

1.2 Three Fundamental Tools of Satellite Studies

Historically, interest in satellite galaxies began in the early ’70th, when the available observational and numerical techniques first allowed for systematic studies. Satellites are typically faint and low mass objects, and in the past both observations and numerical simulations have been affected by small number statistics. However, the advent of large spectroscopic surveys of galaxies, of detailed studies of structures in the Milky Way and Andromeda galaxies as well as improvements in the dynamic range of numerical simulations and the implementation of semi−analytical models of galaxy evolution have enabled the observation, prediction and characterization of

satellite galaxy properties. Here we present a brief review of the principal tools used in the studies of satellite galaxies.

1.2.1 *Observations of satellites of external galaxies: a statistical approach*

Satellite studies in external galaxies have traditionally been hampered by small number statistics, with typically less than 5 objects detected per host. Statistical samples constructed by stacking the satellites of many primaries partially overcome this problem and have been extensively used in the past. Furthermore, it is desirable to use satellites as true "tracers" of the potential of the host in order to minimize complications in the interpretation of their dynamical properties. Most studies accomplish this by imposing "isolation" criteria; typically a brightness difference exceeding ~ 2 mag is required between the host and its brightest companion within ~ 500 kpc, which results in most primaries having one or two satellites bright enough to render them amenable to observation. Following the pioneering work of Holmberg (1969), Zaritsky et al (1993, 1997) compiled perhaps the first statistically sound sample of satellite−primary systems with accurate kinematics, and were able to provide persuasive evidence that the dark matter halos hinted at by the rotation curves of spiral galaxies are indeed rather massive and extend to several hundred kpc away. This kind of studies have entered a new realm since the advent of large redshift surveys, such as the 2dFGRS (Colless et al 2001) and the SDSS (York et al 2000 , Strauss et al 2002), which have increased many−fold the number of primary−satellite systems known. Studies based on these datasets have corroborated and extended the results of Zaritsky et al, and predictions about the abundance, distribution, and dynamics of satellites now appear robust (McKay et al 2002, Prada et al. 2003, Brainerd 2004a,b, 2005, Sales & Lambas 2005, van den Bosch 2005a,b, Agustsson & Brainerd 2006, Yang et al 2006, Chen et al. 2006) .

1.2.2 *Satellites on Numerical Simulations and Semi-analytical models*

N−body simulations are extensively used to study the evolution of cosmic structures. Nevertheless, it has only recently been possible to apply N−body techniques to the study of the satellite dynamics. Early attempts in this field were unable to follow the evolution of subhalos once they fall onto a larger halo. This artificial destruction of the DM subhalos arises from numerical artifacts due to the low number particles and the poor resolution of the forces involved (Klypin et al. 1997, Moore et al. 1999). In the late 90's significant improvements in the numerical codes and computational power revealed that halos contain a significant population of substructures able to survive during several orbital times (Ghigna et al 1998, Moore et al. 1999, Lewis et al 2000, Jing and Suto 2000, Fukushige & Makino 2001) . Moreover, the inclusion of the dissipative processes associated with baryons may make subhalos more resilient to tidal disruption (Nagai and Kravtsov 2005, Weinberg et al. 2006) .

Present numerical capabilities allow reliable simulation of the dark matter and gas physics on galactic scales, although such simulations are computationally expensive. An alternative approach for studying the formation and evolution of galaxies (and

their satellites) is provided by the semi−analytical methods. These techniques follow the merging and survival of dark matter halos by means of analytical Monte−Carlo prescriptions *or* the results of N−body simulations and combines this with a set of physically−motivated recipes to describe the baryon−driven processes that govern sub−galactic scales. The study of the evolution of substructures is then greatly simplified although we pay the price of dealing with results that may depend on the particular astrophysical recipe implemented (see Baugh 2006 for a comprehensive review) .

Unlike observations, numerical simulations allow a detailed description of the *three−dimensional* spatial and velocity distributions of satellites, as well as the tracking over time of the structural evolutions that they experience after crossing the virial radius of the hosts.

1.2.3 *The Best Laboratory: Satellites in the Local Group*

The satellite population of the Local Group differs considerably from those studied in external galaxies, as the proximity of the satellites allow us to probe much further down their luminosity function than around a typical primary. The Local Group is the only place where we can study stellar properties *individually*, i.e., we observationally resolve each star determining its age, metallicity and dynamics as separate objects. Some of these stars belong to the present−day satellite galaxies orbiting within the local group and still remains gravitationally bound to them at the present. The other set of stars we study is associated to the Galactic components, where the contribution from merged satellites is thought to be important. The comparison of general properties between both stellar populations is extremely relevant to validate our hierarchical picture of how galaxies assemble their masses. In the last decade, observational evidence of the lumpy build−up of the Milky Way and Andromeda galaxy has emerged. Examples of the important role of these minor mergers in shaping our galaxy are: the disrupting Sagittarius dwarf (Ibata, Gilmore & Irwin 1994), the Arcturus stream (Eggen 1996, Navarro, Helmi & Freeman 2004), the Monoceros ring (Yanny et al 2003), the Canis Major dwarf (Martin et al. 2004) and the Orphan stream (Belokurov et al 2007).

The study of Local Group satellite galaxies has been revolutionized recently by digital imaging surveys of large areas of the sky. More than a dozen new satellites have been discovered in the past couple of years (Zucker et al. 2004, 2006; Belokurov et al. 2006, 2007; Irwin et al. 2007; Majewski et al. 2007), due in large part to the completion of the Sloan Digital Sky Survey and to concerted campaigns designed to image in detail the Andromeda galaxy and its immediate surroundings (Ibata et al. 2001, Ferguson et al. 2002, Reitzel & Guhathakurta 2002; McConnachie et al. 2003; Rich et al. 2004; Guhathakurta et al. 2006; Gilbert et al. 2006; Chapman et al. 2006; Ibata et al. 2007 submitted). The newly discovered satellites have extended the faint−end of the galaxy luminosity function down to roughly $\sim 10^3$ $L_\odot$, and are likely to provide important constraints regarding the mechanisms responsible for "lighting up" the baryons in low-mass halos. These, in turn, will serve to validate (or falsify) the various theoretical models attempting to reconcile the wealth of "substructure" predicted in

cold dark matter (CDM) halos with the scarcity of luminous satellites in the Local Group mentioned in Section 1.

1.3 What we know (and do not know!) about Satellites

The implementation of the above described techniques to study satellite galaxies has led to substantial improvements in our understanding of low mass galaxies. We summarize in several points the main findings obtained so far regarding satellites, some of them being the source of motivation for the present Thesis.

- *The angular distribution of satellites*
  Primary−satellite samples in observational surveys are used to search for correlations between the position angle of the host galaxy and that of the satellites, since anisotropies in the satellite distribution around the host would signal a possible flattening of the surrounding halo; a preferential direction of accretion; and/or the secular effect of orbital decay. The intriguing observation by Holmberg (1969) that satellites tend to align with the minor axis of disk galaxies (the "Holmberg effect", see also Zaritsky et al 1997) has now been revisited by several authors and some degree of consensus has been reached in the opposite direction: structures tend to align with the disk (major axes) of the hosts (Brainerd et al. 2005 , Agustsson & Brainerd 2006 , Yang et al. 2006). Regardless of the resolution of this controversy, it is clear that in the case of our own Galaxy, the Milky Way, some kind of "Holmberg effect" is present (Lynden−Bell 1982 , Majewski 1994). This peculiar arrangement seems to apply as well to M31 once a particular type of dwarfs are selected (Hartwick 2000 , Koch & Grebel 2006), and is at odds with what would be expected from fair tracers of the dark matter halo, which is thought to be only mildly triaxial (Kroupa et al 2005). This stresses that further interplay between numerical simulations and observations is needed to bring observations and theoretical predictions into agreement.

- *The radial distribution of satellites*
  In absence of no other luminous tracers, satellite galaxies place important constraints on the density profiles of host halos beyond $\sim$ 100 kpc. Recent numerical simulations of galactic and clusters scales have shown that the number density profile of subhalos is shallower in the inner regions than the one corresponding to the smooth dark matter component (Ghigna et al. 2001, Gao et al. 2004b, Diemand et al. 2004) Nevertheless, when some semi−analytical prescription is added to mimic the galaxy satellites inhabiting within these subhalos, the match between the dark matter and the satellites profiles is improved (see also Nagai & Kravtsov 2005). Statistical constraints may also be drawn from the analysis of large redshift surveys, although the results have remained inconclusive due to the high fraction of interlopers[2] usually found in these primary−satellite systems (van den Bosch et al. 2005, Sales & Lambas 2005, Chen et al. 2006).

2 Spurious satelites physically unbound to the primary, that are misclassified as "satellites" in projected data contaminating the samples of "real" primary-satellite systems

- *Satellite velocities and the mass of the host halos*
  For the Local Group galaxies, the ~ 10 brightest dwarf galaxies associated to each, the Milky Way and Andromeda galaxies, have been combined with other luminous tracer to estimate the mass of these galaxies (Wilkinson & Evans 1999, Evan & Wilkinson 2000, Sakamoto et al. 2003, Battaglia et al. 2005) . In external systems, following the early works of Zaritsky and White (1994), the dynamics of satellite galaxies have been used to put constrains on the shape and mass of the host halos. The evidence suggests that early−type galaxies are surrounded by halos about twice as massive as late−type systems of similar luminosity (see Brainerd 2004a).

- *Structural changes induced in satellite galaxies due to tides*
  Satellites orbiting in external gravitational fields experience harmful forces that may drive its disruption and/or merging with the host as soon as the satellite approaches the primary. If the satellite manages to survive, its structural properties (mass, morphological type, intrinsic velocity dispersion of stars) would be altered depending on the amount of mass that have been removed. In the case of close pericenter passages, where tidal forces are maximum, the dwarf galaxy may develop a bar instability able to transform faint spirals or irregulars onto dwarf spheroidals (Mayer et al. 2001a,b). This may also explain the morphological segregation of Local Group satellites that shows satellite galaxies with considerable gas content are located preferentially in the outskirts of the system.

- *Tidal debris of satellites and the formation of galactic components*
  Once a satellite finally merges with the host its stars are incorporated to the central primary galaxy. A satellite contribution to either galaxy component (thin/thick disk, bulge, stellar halo) depends mainly on its orbit and on the degree to which dynamical friction circularizes the orbit before disruption (Abadi et al. 2003b). Satellites on nearly circular orbits are expected to contribute to the disk components, specially if the plane of the orbit is roughly coincident with the plane of the disk. In this picture, extended disks as that observed for the Andromeda galaxy (Ibata et al. 2005) might be a common feature of hierarchical models (Peñarrubia, McConnachie & Babul 2006). The oldest stars in galaxies might therefore have been brought in by the population of satellites that merged in the past with the host.

1.4 Outline of this Thesis

This Thesis is based on two main approaches to study the satellite population of galaxies: a statistical analysis of a large semi−analytical catalog of galaxies (Part I), and a dynamical study of N−body/SPH simulations of galaxy formation (Part II). The first Part is aimed at characterizing *statistically* primary−satellites galaxy systems in a ΛCDM Universe. In Chapter 2, we present an analysis of the properties of the satellite galaxies at $z = 0$ identified in the N−body *Millennium Run* with the help of a semi−analytical code (Springel et al. 2005, Croton et al. 2006). This is the largest

resolution simulation able to resolve galaxies as faint as the Large Magellanic Cloud in a box size of 500 h^{-1}Mpc side. It allows a comprehensive analysis of the satellite spatial and velocity distributions around isolated hosts based on a robust statistical sample. This chapter evaluates to what extent satellite galaxies might be considered faithful tracers of the hosts's dark matter distribution. It also provides insight into how the cosmological predictions of ΛCDM models should be interpreted in observational samples. In Chapter 3, we use the dependence on mass of the color−magnitude relation of isolated hosts galaxies found in the *Millennium Run* analysis to propose a new algorithm for selecting satellites from large redshift surveys. This method builds on lowering the fraction of interlopers in the sample, and after testing in a mock catalog, we apply the algorithm to the Sloan survey and explore the projected radial density profile of satellites in observations.

In the second Part we also focus on numerical simulations, although the approach is less statistical and more dynamical. It is mainly based on the analysis of 8 high resolution N−body/gasdynamical simulations of galaxy formation in a ΛCDM Universe. In Chapter 4 we concentrate on the time evolution of satellite populations, specially on the differences that characterize *surviving* and *merged* satellites. We find that the interaction with the host potential substantially alters the orbits and mass contents of satellite galaxies. This motivates our last chapter where we focus our attention on a particular subset of satellite that, as a result of three−body interactions end up on highly energetic orbits, escaping from the host after their first pericenter passage. These satellites are quite reminiscent of some high−velocity dwarfs of the Local Group, and we speculate about its possible origin linked to this effect. Finally, Chapter 6 summarizes the main results.

Part I

STATISTICAL ANALYSIS OF SATELLITE GALAXIES IN THE MILLENNIUM RUN

2

SPATIAL AND VELOCITY DISTRIBUTION OF SATELLITE GALAXIES IN THE MILLENNIUM RUN

2.1 Abstract

We study the spatial distribution and kinematics of satellites galaxies selected from the *Millennium Run* N−body simulation + semi−analytic galaxy catalog (Springel et al. 2005, Croton et al. 2006). A sample of ~ 80000 isolated host galaxies have been selected that expand almost three decades in dark matter halo mass. This allows us to study the typical satellite properties predicted by the ΛCDM model in a wide range of local low−density environments. We find that satellite galaxies are radially distributed according to an NFW profile of average concentration parameter $c \sim 5.6$. Satellite galaxies are reasonable good tracers of the dark matter content of their hosts in the range $0.2r_{200} < r < 2r_{200}$. However, the large majority of satellites within $\sim 0.5r_{200}$ have been stripped of their own dark matter subhalos, causing strong radial biases between the smooth dark matter background in hosts and the distribution of the dark matter clumps. Satellite populations are segregated according to their color indices and magnitudes, with a tendency for redder and more luminous satellites to be more concentrated towards the center of the hosts. We also explore satellite velocities, finding evidence of a strong infall pattern beyond the virial radius of hosts, with typical infall velocity dispersions $\sigma_r \sim 0.15 - 0.25V_{200}$. Within the virial radii, velocities are well represented by Gaussian distributions, with dispersions that decay from center outwards by a factor of ~2 at r_{200}. The general $L^{host} - \sigma$ relation follows a double power−law behavior, with a change of slope at $\sigma_{1D} \sim 200$ km/s, which can be interpreted as a transition region between single galactic halos to fossil group−like systems. Blue host galaxies do not show this break, supporting our previous hypothesis. Regarding satellite orbits, we find a clear tendency of satellites to move in pro−grade sense compared to the host angular momentum, in agreement with the CDM model predictions. The angular distribution of satellites shows certain degree of anisotropy, with an excess of satellites in the direction perpendicular to the angular momentum of the hosts, confirming previous numerical and observational findings.

2.2 Introduction

The present Chapter aims to explore the spatial distribution and kinematics of satellites orbiting isolated host galaxies in a ΛCDM universe. The Millennium simulation plus a semi−analytical code run on top of it (Springel et al. 2005, Croton et al. 2006) allow us to resolve galaxies as faint as the Large Magellanic Cloud within a cubic region of $500h^{-1}$ Mpc on a side. A total of $\sim 2x10^6$ galaxies can be identified at $z = 0$, providing an unprecedented simulated catalog to study satellite galaxies in a statistical way. The fundamental difference between this work and previous studies of satellites in numerical simulations is the large number of galaxy systems here analyzed, $\sim$ 80 thousand, where previous studies rely on less than a couple of dozen hosts.

As highlighted in Chapter 1, how satellites are radially distributed within host halos is a fundamental question still under debate. Since several conclusions from observations are obtained based on the hypothesis that satellite galaxies are faithful tracers of the underlying dark matter distribution, this point surely deserves to be carefully addressed. It seems like N−body simulations of different scales are converging to a scenario where dark matter subhalos have a notably shallower distribution than the dark matter in CDM halos (Ghigna et al. 2000, Diemand, Moore & Stadel 2004, Gao et al. 2004a) while more realistic treatments that includes SPH or semi−analytical modeling of baryon physics produce satellite galaxies that are more similar to the dark matter profile. Springel et al. (2001) suggest that the relation between galaxy luminosity and virial mass of the subhalo depends on clustercentric distance. Since luminosity is related mostly to stellar mass, and stars are concentrated on a few central kpc of subhalos, the tidal stripping that substructures experience when orbiting in the host halo affects the stellar mass less than the dark matter contents of subhalos. Therefore, substructure in DM only simulations may miss objects that have lost a significant fraction of their dark matter, but still could survive as a dwarf due to the almost unperturbed bound core of baryons. Taking this into account, also Gao et al. 2004b found no spatial bias between dark matter and modeled galaxies in cluster−sized dark matter halos. Similarly, Kravtsov, Gnedin & Klypin (2004) reconcile the galaxy and the dark matter radial distribution on Milky Way−sized halos by modeling galaxy formation in such a way that today visible satellite galaxies are not the most massive subhalos at z=0, but they are the descendant of the most massive subhalos at higher redshifts. Also numerical simulations that includes baryons have been explored. Recent works (Maccio et al. 2006, Sales et al., submitted) using a SPH modeling found that satellites closely follows dark matter distribution of a host galactic halo $M_{vir} \simeq 10^{12} M_\odot$, and this is mainly due to the inclusion of dissipative processes that enlarge the survival times of subhalos. Similar conclusions were obtained previously by Nagai & Kravtsov (2004) in galaxy cluster halos.

The discussion above highlights the importance of the study of satellite spatial distribution, but also satellite velocities reveal important properties about host halos. Satellite dynamics are largely determined by the host potential well, and therefore we can constrain not only the total amount of mass within the host, but also we learn how concentrated its distribution is. Notice that both of these parameters are impossible to get directly from observations and then satellite velocities may help to constrain them.

Nevertheless, it only becomes possible if we are able to quantify precisely how well satellite dynamics reflect the dark matter properties of host halos. This constitutes the main motivation for studying 3D satellite velocities in numerical simulations, trying to determine whether there exist a bias or not between velocity dispersion of substructure and dark matter particles within the halos. Ghigna et al. 2000 and Diemand et al. 2004 find that although velocity dispersion of satellites is not the same than dark matter particles of hosts, their anisotropy parameter $\beta = 1 - \sigma_t^2/(2\sigma_r^2)$ (where σ_t and σ_r are the tangential and radial velocity dispersion) seems not to differ significantly. This is an important result, that allow us to use formalisms, such as that of Jeans, to put constrains on host halo concentrations starting from 3D satellite velocities. But careful attention must be paid to this offset between substructure and host dark matter halo, since several mass determinations of galaxy systems on observations rely on the hypothesis of satellites as un−biased tracers of the host halo potential.

In the following section we briefly describe the *Millennium Run* simulations, the selection criteria applied and the final host and satellite samples. Section § 2.4 describes our main results and the partial conclusions drawn from this Chapter are shown in section § 2.5. Throughout this Chapter we assume a Hubble constant $H_0 = 100h$ km/s Mpc^{-1} with $h = 0.73$. Masses, scales and velocities are expressed in $M_\odot h_{70}^{-1}$, h^{-1}kpc and km/s respectively unless contrary stated. Virial values are computed at the distance where their mean spherical overdensity is 200 times the critical density of the universe. This defines implicitly the virial mass, M_{200}, virial radius, r_{200} and the circular velocity, V_{200}, of halos.

2.3 The Catalog

This Chapter describes several properties of satellite galaxies selected from the *Millennium Run* N−body simulation + semi−analytical code (Springel et al. 2005, Croton et al. 2006). In the following two subsections we provide a brief review of the *Millennium Run* simulation and the semi−analytic model (focusing mainly on those points more relevant in satellite galaxies) and we also describe in Section 2.3.2 the selection criteria applied to build the samples.

2.3.1 *The Millennium Run and the Semi−analytic Model*

The *Millennium Run* is one of the projects of the Virgo Consortium [1], aimed to have an unprecedented high mass resolution combined with a large box size. It follows the evolution of almost 10 billion particles spread on a box of 500 h^{-1} Mpc on a side. The particle mass is 8.6 x $10^9 h^{-1} M_\odot$, giving a spatial resolution of 5 h^{-1} kpc. The simulation adopts parameters consistent with the WMAP1 results (Spergel et al. 2003; Seljak et al. 2005): $\Omega_m = 0.25$, $\Omega_\Lambda = 0.75$, $h = 0.73$, $n = 1$, and $\sigma_8 = 0.9$ (for details see Springel et al. 2005).

The output of this collisionless simulation is combined with a semi−analytical code (Croton et al. 2006) that provides astrophysical quantities such as Sloan magnitudes

1 http://www.virgo.dur.ac.uk/new/index.php

ugriz, star formation rate, mass in stars and cold gas, bulge and disk masses, etc. Also a careful treatment of processes like radiative cooling, star formation, growth of supermassive black holes, metal enrichment, feedback, morphological transformation of galaxies and effects due to a reionising UV background are included.

Some of the above mentioned physical processes are extremely important at the faint end of the luminosity function, and therefore in the satellite galaxies we will study later in Section 2.4. It is the case of the implementation of the supernova feedback, the reionization and the mass evolution and merging of subhalos. It is then worth to keep in mind how these three relevant points are particularly modeled in our catalog, although we refer the reader to Croton et al. 2006 for a much more comprehensive description of the code:

- *Supernova feedback*
  Star formation activity and the evolution of the high mass stars involve an injection of energy and metals to the surroundings at the end of their lives. This mechanism is usually referred as "supernova feedback" and represents an effective way of heating the gas that fuel the star formation activity, decreasing the efficiency with which gas turns into stars in galaxies.

  The amount of gas reheated by supernova ejecta ($\Delta m_{reheated}$) is proportional to the mass of stars formed during a given time−interval Δm_*:

  $$\Delta m_{reheated} = \epsilon_{disk} \Delta m_*$$

  where the proportionality constant ϵ_{disk} is one of the free parameters of the semi−analytical code and has been fixed to 0.35 in the model. The energy released by this depends on $\Delta m_{reheated}$ and on the mean energy in supernova ejecta per unit mass of stars formed ($0.5 V_{SN}^2$) through the efficiency with which this energy is able to reheat the disk gas (ϵ_{halo}) as:

  $$\Delta E_{SN} = 0.5 \epsilon_{halo} \Delta m_* V_{SN}^2$$

  with $\epsilon_{halo} = 0.35$ and $V_{SN} = 630$ km/s based on supernova theoretical estimations. If all the reheated gas were added to the hot halo, its thermal energy would change by:

  $$\Delta E_{hot} = 0.5 \Delta m_{reheated} V_{200}^2$$

  And therefore the ejection of gas from the halo is determined by the sign of the difference between ΔE_{SN} and ΔE_{hot}:

  $$\Delta m_{ejected} = \frac{E_{SN} - E_{hot}}{E_{hot}} m_{hot} = \left(\epsilon_{halo} \frac{V_{SN}^2}{V_{200}^2} - \epsilon_{disk} \right) \Delta m_*$$

  where the total energy in the hot halo is $E_{hot} = 0.5 m_{hot} V_{200}^2$. If $(E_{SN} - E_{hot}) < 0$ the energy transferred with the reheated gas is insufficient to eject any gas

out of the halo; on the other hand, if $(E_{SN} - E_{hot}) > 0$ an amount $\Delta m_{ejected}$ of the original m_{hot} is removed from the halo into an external reservoir from where it can be re−accreted later under favorable conditions. The last equation shows that for small V_{200} values, the entire hot gas content can be expelled whereas for halos exceeding ~ 200 km/s this mechanism is very inefficient. As shown, supernova feedback has a fundamental role in shaping the faint end of the luminosity function of galaxies, and therefore is quite important in the modeling of satellites.

- *Reionization*

  A second process invoked to lower the efficiency of cooling and accretion of gas into low mass halos is the photoionization heating of the intergalactic medium, which suppresses the condensation of baryons in shallow potentials.

  Based on Gnedin (2000) the model adopt a filtering mass $M_F(z)$ below which the baryonic fraction f_b is reduced compared to the universal value:

$$f_b^{halo}(z, M_{200}) = \frac{f_b^{cosmic}}{(1 + 0.26 M_F(z)/M_{200})^3}$$

- Evolution and merging of subhalos

  The substructure identification algorithm is able to track the positions and velocities of all groups of dark matter particles in the simulation that exceed 20 members, or equivalently, halos more massive than $M_{200} = 1.7 \times 10^{10} h^{-1} M_\odot$. When subhalos lose a fraction of their mass and drop below this limit, the positions and velocities of these "galaxies" are thereafter traced by those of the most bound dark matter particle at the last output time before this occurs. At the same time, a typical time−scale for the dynamical friction with the host halo is computed for each one in order to estimate the merging time, t_{merge}, of such satellites. For a satellite of mass m_{sat} orbiting on an isothermal potential of circular velocity V_{200} we have:

$$t_{friction} = 1.17 \frac{V_{200} r_{sat}^2}{G m_{sat} \ln\Lambda}$$

  (Binney & Tremaine 1987), where the Coulomb logarithm is approximated by $\ln\Lambda = \ln(1 + M_{200}/m_{sat})$ and r_{sat} and m_{sat} are the values measured the last time the subhalo was identified. The model then merges the satellite with the central galaxy when a time t_{merged} has passed after its last identification. Depending on the mass ratio between the central and the satellite galaxy the merge can be classified as: "minor" or "major", which involves differences in the bulge−to−disk ratio and star formation activity of the merger remnant.

  We should notice however that the estimated t_{merged} is only a crude approximation to the real time the satellite would take to merge, since the flattening of

the host potential, the mass loss suffered by satellites and the possible circularization acting on their orbits have not been taking into account in the previous formulation. These effects can notably affect t_{merged} (e.g., see Taylor & Babul 2001, Peñarrubia, Just & Kroupa 2004, Zhao 2004) and then the results based on this particular population of satellites without subhalo should be taken with caution and might be subject to a rigorous comparison against the dynamics of satellite galaxies observed in the real data.

2.3.2 *Satellite Selection Criteria*

We have selected from the *Millennium Run* z=0 output a sample of primary and satellite galaxies applying the following selection criteria: an *isolated* is, by definition, a galaxy brighter than r−band absolute magnitude $M_r = -20.5$ where all galaxy companion within a sphere of 1 h^{-1} Mpc is at least 2 magnitude fainter than our isolated galaxy candidate. In this way we assure that the local dynamics are mostly dominated by the potential well of the primary galaxy. Once the sample of isolated galaxies is identified, we search for satellites in the vicinity of each one, considering as *satellites* to all galaxy brighter than $M_r \leqslant -17$ and being at least 2 magnitudes fainter than the associated primary. The number of satellites (NS) we find within the virial radius of each isolated galaxy halo splits the sample into two subsamples: *singles* and *primaries*. If $NS = 0$ the isolated galaxy is labeled as a *single* while, if we find one or more satellites with distance $r < r_{200}$, the galaxy is considered a *primary* or alternatively, a *host*. The probability of being either a single or a host galaxy varies with galaxy luminosity. In table 1 we show the fraction of isolated galaxies in 6 luminosity ranges, together with the fraction of them having at least 1 satellite brighter than $M_r = -17$ within r_{200}. For those brighter than $M_r = -23$ approximately $\sim 23\%$ fulfill the requirements to be isolated and the large majority of them ($\sim 93\%$) host satellites within their virial radii. On the other hand, for the most faint galaxies ($M_r > -21$) the probability of being isolated is $\sim 19\%$ but the chance of having at least one satellite brighter than the LMC ($M_r \leqslant -17$) remarkably drops to $\sim 15\%$. We notice that a galaxy like the Milky Way would be not included in our sample since, due to the proximity and comparable brightness of our neighbor M31, the MW does not fulfill the proposed isolation criteria. Certainly, we could be less restrictive to define isolated galaxies in order to include a larger fraction of galaxies as hosts. However, by doing so we would enlarge the host sample at the expense of including a large number of primaries that are not the *central* galaxy of a given dark matter halo. In other words, we look for systems where the host galaxy is already settled in the center of the host halo potential (i.e. it is a *central* galaxy), trying to avoid considering as hosts those galaxies that are themselves orbiting within another system (e.g., a group or a cluster). Therefore the isolation criteria is always a compromise between having a large number of hosts and maintain as low as possible the number of *non−central* primaries. We have checked that applying the criteria described above the fraction of hosts that are of the *central* type is larger than 99%, which guarantees our results will be not seriously affected by these *non−central* primaries. The sample we analyze here is composed by 258321 isolated galaxies and $\simeq$ 79000 hosts. More than $\simeq$ 178000 satellites have been found

$\log(L/L_\odot)$	M_r	f_{iso} (%)	f_{host} (%)	f_{host}/f_{iso} (%)
$10.0-10.2$	(-20.5,-21.1)	18.8	2.9	15
$10.2-10.4$	(-21.1,-21.6)	22.1	8.3	37.5
$10.4-10.6$	(-21.6,-22.1)	24.8	15.4	62.1
$10.6-10.8$	(-22.1,-22.6)	23.4	19.1	81.6
$10.8-11.0$	(-22.6,-23.1)	25.2	11.5	89.9
>11	<-23.1	24.9	23.05	92.6

Table 1. Fraction of isolated galaxies f_{iso} and of those isolated galaxies having at least 1 satellite within r_{200} brighter than $M_r < -17$, f_{host} in the Millennium Run. We have computed these fractions by a comparison between the number of isolated and host galaxies in each luminosity range in our samples and the total luminosity function computed for all galaxies in the Millennium Run semianalytical catalog (Croton et al. 2006).

orbiting within the virial radii of our hosts, while this number raises to ~ 508000 if we consider satellites within $1h^{-1}$ Mpc radius spheres centered at each host galaxies.

2.4 Characterization of the Satellite Population

2.4.1 *Mass−Luminosity−Color relation for primaries*

Determining the dark matter surrounding galaxies is a difficult observational task. Because of this, numerical simulations have become a very powerful tool to make predictions about the dependencies of DM halo properties on observable quantities such as luminosity, color, environment, etc. Probably, the most widely studied relation of this kind is the virial mass−to−light ratio (M/L); i.e. the relation between the total mass of the halo and the luminosity of its "central" galaxy. This relation shows large scatter, mostly attributed to different galaxy Hubble types, different environments and halo merger histories, among others. We show in panel a) of figure 1 the (*r band*) luminosity−halo virial mass relation (M−L) for the isolated galaxy sample, where the color−coding indicates the number density of points in the plot (see figure caption). It can be seen from this figure that isolated galaxies at fixed luminosity span almost a decade in dark halo virial mass, what indicates that we should not expect strong constrains on M_{200} coming only from their luminosities.

A careful inspection of panel a) of figure 1 reveals the existence of three relatively well−defined sequences of isolated galaxies in the M−L plane. Dotted, solid and dashed lines indicate different constant mass−to−light ratio relations drawn by eye highlighting the three sequences. Starting at the low mass end, there is a tail of objects with quite high luminosity given their M_{200} value (dotted line). These are probably truly low mass galaxies undergoing some kind of starburst. Also noticeable is a main sequence (solid line), with intermediate virial mass halos and luminosities

lower than $L \sim 10^{11} L_{\odot}$ where most of the isolated galaxies tend to reside. And finally the remaining galaxies (dashed line), having typically high virial mass and in some cases with high luminosities exceeding $L > 10^{11} L_{\odot}$. These extremely luminous galaxies are likely to be strongly affected by the AGN heating implementation of the semi−analytical code (Croton et al. 2006), which stops the gas condensation onto central galaxies of massive systems, preventing the formation of new stars. This feedback effect naturally reproduces the red colors associated with elliptical galaxies in massive systems. The dominance of either starburst or feedback processes on both extremes of the primary virial mass distribution suggests that galaxy colors should differ in each of these sequences. Inspired by this and in order to obtain more accurate DM mass estimates from observational data, we have applied simple color cuts to the primary sample according to: $(g-r) \leqslant 0.65$, $0.65 < (g-r) \leqslant 0.95$ and $(g-r) > 0.95$, exploring the M−L relation for each subsample separately (see panels b), c) and d) of figure 1). Although the cuts are somewhat arbitrary, the color restricted subsamples exhibit a better defined sequence in the M−L plane, significantly lowering the scatter of panel a).

The virial masses of systems define implicitly their virial radii, and hence the (projected) sphere we need to define for satellite finding observational algorithms. It is common in the literature to search for satellites within a circular region centered on each primary candidate using a fixed projected radius for all potential hosts (for instance R_{search} ~500 kpc). As shown in figure 1, the virial mass of primary galaxies can significantly vary through the sample, and then, a single R_{search} value produces an under(over)−estimation of the virial radius in low (high) mass systems. We come back to these ideas and findings in Chapter 3 and use them to develop a new identification algorithm of satellites in large redshift surveys.

The next step in our analysis is to compare the mass−luminosity relations for host galaxies (those for which we detect satellites within their r_{200}) to the obtained for isolated without satellites (single galaxies). In figure 2 we show the M_{200} distribution of hosts and single galaxies for 6 luminosity bins, taking into account the color sequences defined previously. Histograms are normalized to the total number of galaxies in each luminosity bin indicating the relative fraction of galaxies in a given color subsample. The first clue about differences between hosts (upper panel) and singles (lower panel) comes from the fraction of red galaxies in each sample. As the upper panel indicates, the relative fraction of red (host) galaxies increases monotonically with host luminosity from 20% to 60%, but remains lower than 20% in the case of single galaxies irrespective of luminosity. This is in agreement with the common expectation of isolated galaxies being on average bluer than galaxies of similar luminosities living in multiple systems. Intermediate color galaxies clearly dominate both samples of galaxies up to $\log(L/L_{\odot}) \simeq 11$, nevertheless, this "main sequence" almost disappears for luminosities brighter than $10^{11} L_{\odot}$. This analysis suggests that such extremely luminous primaries cannot be ordinary galaxies but they are either undergoing starburst events showing blue colors, or they are the central galaxy of high mass systems such as groups, where the accretion of cold gas have been suppressed by primordial AGN feedback turning redder their colors.

The virial mass ranges involved in both distributions (figure 2) although similar

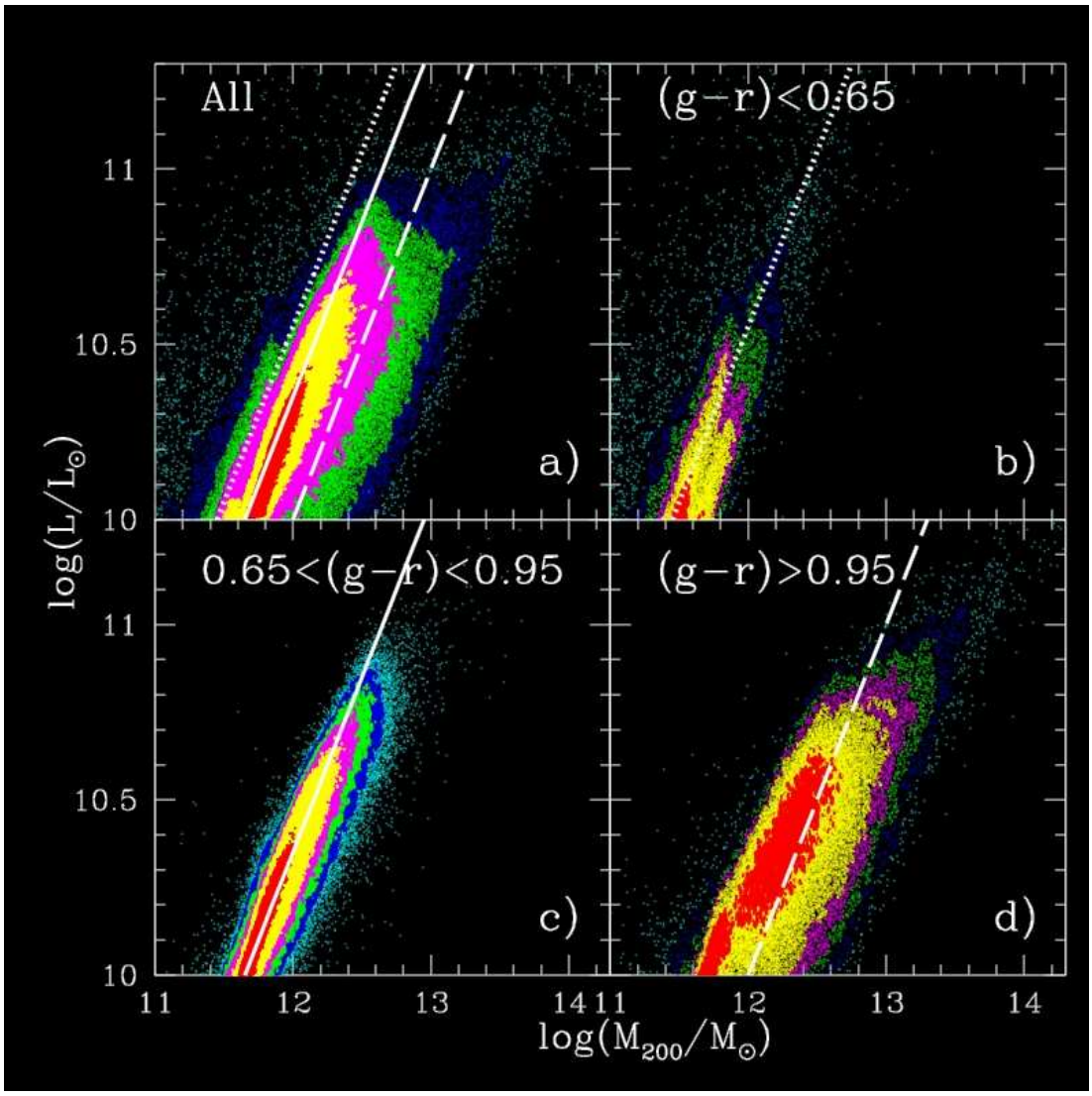

Figure 1. Virial mass−Luminosity (r−band) relation for isolated galaxies. Dotted, solid and dashed white curves show a drawn−by−eye constant mass−to−light ratio. Panel a) shows the general relation where all isolated galaxies are included. Colors show local density of points, so that for panel a) limits are (in units of the $\log(\rho_{points}/\bar{rho}_{points})$): .lt. −4 (cyan), (−4,−3) (blue), (−3,−2) green, (−2,−1) magenta,(−1,0) yellow and densities larger than $\bar{rho}_{points}$ in red. In panels b), c) and d) only blue, intermediate and red isolated galaxies respectively are shown. The limits for the color codding according to the local point densities are: −2.5,−2,−1.5,−1 and 0. Dotted, solid and dashed line indicate constant M/L ratios to guide the eye once color cuts are applied in panels b), c), and d).

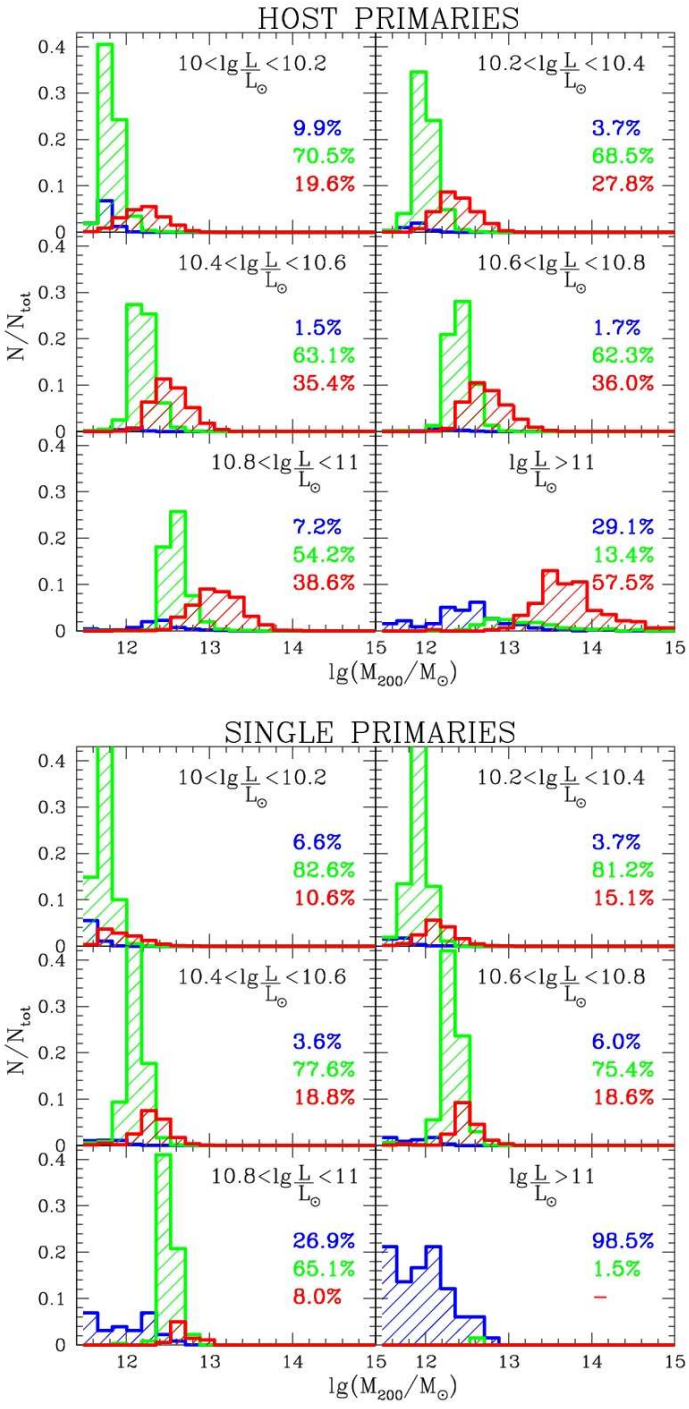

Figure 2. Virial mass distribution in luminosity bins for host (upper panel) and single (bottom panel) galaxies separated according to color cuts of figure 1). Histograms have been normalized to the total number of galaxies in each luminosity bin. Percentages in right rows indicate the fraction of hosts in each color sequence for a given luminosity bin.

for the low luminosity bins, differs appreciably for the brightest primaries. In all luminosity bins, the model predicts that single galaxies tend to live in less massive halos than hosts of similar luminosity. Moreover, our results indicate that there exists an upper limit to the halo virial masses of single galaxies, $M_{200} < 10^{13} M_{\odot}$ regardless of galaxy luminosity beyond that the corresponding amount of baryons available allows the formation of at least one satellite galaxy as bright as or brighter than the LMC.

The probability of a bright galaxy to fulfill the isolation criteria adopted here provides valuable insights to the statistics of *fossil groups* (FGs hereafter). FGs are X−ray bright galaxy groups with an integrated optical luminosity dominated almost totally by the central massive elliptical galaxy and where the magnitude gap between the first and second brightest galaxies is at least two (Jones et al. 2003) . Although we do not have estimate of the X−ray emission of our host systems, the currently adopted limit on the magnitude gap of fossil groups (2 magnitudes) makes our isolated galaxies very comparable to them. Several authors have argued that FGs are the result of an early group formation time, followed by a quiet dynamical evolution after $z \sim 1$ in a relatively low density environment (see for instance D'Onghia et al. 2005). Also highly anisotropic galaxy orbits are expected to favor FGs formation (Sommer−Larsen 2006). The fraction of groups that are fossil−type is an intriguing issue that is still uncertain today. It may depend on group mass, but for comparable mass ranges ($10^{13} - 10^{14} M_{\odot}$) observations suggests that between 10−20% of groups are FG (Jones et al. 2003), while numerical simulations suggests a higher fraction ∼ 33% (D'Onghia et al. 2005). Contrary to this, based on analytical estimations Milosavljevic et al. (2006) uses the extended Press Schechter Formulation (plus some modifications) assuming that the luminosity of galaxies correlate with the mass in which they reside to derive the probability of halos to host a fossil−group like system. Their analysis shows clearly how this probability changes with halo mass, obtaining that in the $10^{13} - 10^{14} M_{\odot}$ range $\sim 10 - 20\%$ of groups are fossil type in good agreement with observations. For the low mass groups it can raise up to $\sim 50 - 60\%$ whereas the fraction of fossil type systems in the cluster-sized halos (masses larger than $10^{14} M_{\odot}$) is significantly lower ($\leqslant 6\%$).

Given the similarities between FGs and our satellite systems, we can compare these fractions with the probability on the Millennium simulation of finding a halo that contain an isolated *red* galaxy. We have used the mass function computed by Springel et al. 2005 to calculate the total number of halos of a given mass, comparing this with the number of isolated galaxies per mass interval in our sample. We show in table 2 the fraction of fossil−like systems in the total sample of isolated galaxies (f_{tot}) as well as splitting them according to their colors as defined in figure 1. In order to compare with previous estimation of the fossil−groups statistics, we use the last column of table 2 referring only to the *red* isolated galaxies. We obtain that ∼ 9.7% and ∼ 7.5 of halos in the mass ranges: $10^{13} - 10^{14}$ $M_{\odot}$ and $10^{14} - 10^{15}$ $M_{\odot}$ respectively can be classified as a fossil−like system, in good agreement with observational and theoretical estimates (Jones et al. 2003, Milosavljevic et al. 2006). In the mass range $10^{12} - 10^{13} M_{\odot}$ we obtain ∼ 35% as possible fossil−group candidates, a lower value than that derived by Milosavljevic et al. (2006), although in these low mass systems the

Mass ($M_\odot$)	f_{tot} (%)	f_{blu} (%)	f_{int} (%)	f_{red} (%)
$10^{11} - 10^{12}$	24.7	1.6	21.2	1.9
$10^{12} - 10^{13}$	72.1	0.6	37.0	34.5
$10^{13} - 10^{14}$	10.1	0.1	0.3	9.7
$10^{14} - 10^{15}$	8.3	0.2	0.6	7.5

Table 2. Fraction of halos per mass interval in the Millennium Run simulation hosting an isolated galaxy. Three last columns show the percentages once applied the color cuts defined in figure 1. The total number of halos as a function of mass has been derived from Springel et al. 2005.

contribution from intermediate color galaxies is important and could help to explain the differences between our estimation and the $\sim 50-60\%$ expected from analytical studies.

2.4.2 *Satellite radial distribution*

Figure 3 shows the number density profile of satellites ($\rho(x)$) obtained by stacking all systems after re−scaling satellite−host relative distances ($x=r/r_{200}$). Error bars correspond to 20 bootstrap re−samplings, but due to the large number statistics they are smaller than the line width. We fit an NFW profile to this curve obtaining the best value for the concentration parameter $c = 5.6 \pm 0.4$, shown as a red dashed line in the figure. Moreover, we find this c value to be nearly independent of host mass and luminosity. A relevant question is to what extent satellites trace the underlying dark matter mass distribution. As it is well known, the concentration of dark matter halos varies with mass, ranging between ~5 to ~20 from cluster−sized to galactic halos. In a recent work, Fausti-Neto et al. (in prep) find that Millennium Run dark matter halos follow the relation $\log(c) = 1.97 - 0.077\log(M_{vir}(M_\odot/h)^{-1})^2$, with a dispersion $\sigma(\log(c)) = 0.148$. We use this formula to estimate the average dark matter concentration expected for our host sample, i.e, from the actual M_{200} of each host halo and using these relations we draw at random a concentration, and obtain the mean dark matter concentration by averaging over all systems. We find a mean concentration of $c = 8.4$ (see red dotted line in figure 3), where we have accounted for the difference between c_{vir} and c_{200} considering $r_{vir} \simeq 1.3 r_{200}$. We notice from figure 3 that the average distribution of satellites closely resembles that of the dark matter for distances $r > 0.2 r_{200}$, whereas inside in the omission of the central galaxy together with a difficult identification of object closer to the primary determine a satellite number density profile slighter shallower than the dark matter in the host halos. The half

2 the *virial* radius, r_{vir}, of a system is defined as the radius of a sphere of mean density, $\Delta_{vir}(z)$ times the critical density for closure. This definition defines implicitly the virial mass, M_{vir}, as that enclosed within r_{vir}, and the virial velocity, V_{vir}, as the circular velocity measured at r_{vir}. The virial density contrast, $\Delta_{vir}(z)$ is given by $\Delta_{vir}(z) = 18\pi^2 + 82f(z) - 39f(z)^2$, where $f(z) = [\Omega_0(1+z)^3/(\Omega_0(1+z)^3 + \Omega_\Lambda))] - 1$ and $\Omega_0 = \Omega_{CDM} + \Omega_{bar}$ (Bryan & Norman 1998).

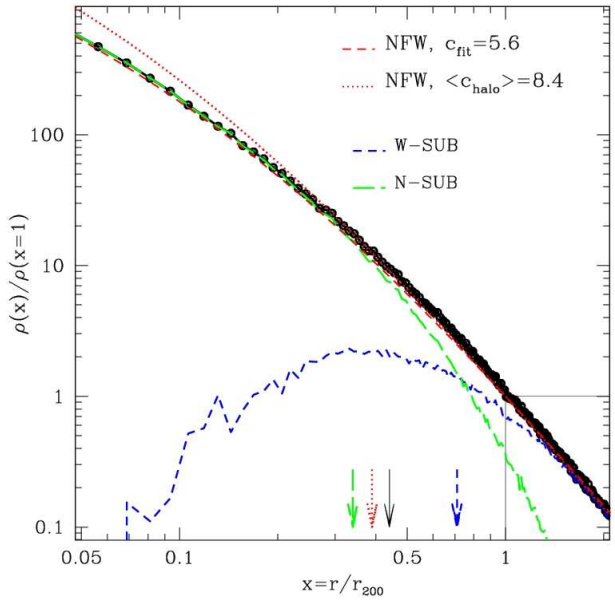

Figure 3. 3D radial distribution of satellites up to $2r_{200}$. Errors are based on 20 bootstrap, but they are smaller than line width. Dashed line shows an NFW profile with best−fit c value of 5.6 ($\pm$0.4). We estimate the dark matter particles profile in the host halos using the $M_{vir} - c$ relation of Fausti−Neto et al. (in prep) finding $c \simeq 8.4$ (see red dotted line). Also quoted in this figure are the number density profiles of satellites that conserve their dark matter substructure (W−SUB satellites, short dashed blue curve) and those that have lost all their dark matter component (N−SUB satellites, long dashed−green line). Vertical arrows show the half mass radii of each sample with the corresponding line and color coding.

mass radii of both distributions are quite similar (see dotted and solid arrows in figure 3): half of the total sample of satellites is contained within $r \sim 0.44r_{200}$, in close agreement with the $r \sim 0.4r_{200}$ that encloses the 50% of the mass of an NFW halo of concentration $c = 8.4$. This reinforces the important role of satellites as tracers of the underlying dark matter distribution in their host halos, specially at large distances, where no other luminous tracers exist.

Galaxies that orbit within systems of larger mass experience several forces that tend to disrupt them, for instance, dynamical friction, tidal stripping, galaxy harassment, evaporation, etc. These effects modify the mass content of galaxies, specially the dark matter and gas components, which are generally less gravitationally bound than stars. In this scenario, a satellite may lose most of its dark matter (sub)halo, but still survive complete disruption due to their central core of stars. The semi−analytical code implemented on the Millennium catalog accounts for this fact by classifying satellite galaxies as type 1 or type 2, depending on whether they retain their dark matter subhalo or have completely lost it, respectively (see Section 2.3). For simplicity, we will refer in what follows as W−SUB satellites to type 1 (with subhalo) satellites

while N−SUB will be used to indicate (no subhalo) type 2 satellites. For N−SUB satellites, their positions and velocities are determined by those of the most bound dark matter particle before subhalo disruption (see Croton et al. 2006 for further details). We explore the radial distribution of satellites with and without subhalos, finding very different profiles (see figure 3). Satellites that retain their subhalo (blue short−dashed line) are located well outside the central regions of their host halos, contributing significantly to the total satellite profile ρ only for distances greater than $\sim 0.7 r_{200}$. On the other hand, satellites without dark matter subhalos (green long−dashed line) fully build−up the general profile up to $\sim 0.5 r_{200}$ from where their contribution to ρ starts to decline. This difference is also reflected in the radius enclosing half of the objects in each subsample: 0.71 and 0.34 for satellites with and without dark matter substructure respectively. We observe that subhalos (W−SUB satellites), due to a combination of both simulation resolution and the previously mentioned satellite mass content variation, become a very biased tracer population of the dark matter profile of hosts. The satellite distribution following a NFW profile arises only as the result of adding up the contribution from dark matter stripped satellites, which are preferentially located in the central regions of host halos.

This segregation between W−SUB and N−SUB satellites has relatively low interest from the observational point of view. Nevertheless, some correlations between the dark matter content and the luminous properties of satellites are likely to be present, making our prediction possible to test in observational samples. We have explored the color distribution of satellites, finding that those with the stripped subhalo are on average redder than those who still retain their dark matter. This can be understood in terms of gas mass content, expected to be more significant for late accretion times and large orbital pericenters. Notice that both conditions are satisfied for satellites located in the outer regions of host halos, precisely the region which we have found to be largely dominated by W−SUB satellites. Figure 4 shows the number density profiles obtained by considering one−third of the bluest (reddest) satellites of the sample (color cuts correspond to: $(g-r) < 0.95$ and $(g-r) > 1.01$). From this figure it is clear that satellites with redder colors are more centrally concentrated than the bluer ones, where the radius that contains half the number of satellites within r_{200} of both subsamples is: $0.32 r_{200}$ and $0.71 r_{200}$ respectively. This trend seems to apply to our own Galaxy, where the population of dwarf galaxies closer to the Milky Way is dominated by red dwarf spheroidals while in the outskirts dwarf irregulars (with important gas mass content and younger stellar populations) are more common. The improvements in the number statistics of satellite systems observed in external galaxies should allow in the near future a detailed study of satellite distribution that confirm (or reject) this theoretical prediction.

On galaxy cluster scales, luminosity segregation of member objects is an important issue still under debate. Prior works have argued in favor of (Yepes et al. 1991, Kashikawa et al. 1998, Girardi et al. 2003, Pracy et al. 2004, Mathews et al. 2004, Coenda et al. 2006) and against of (Bahcall et al. 1973, Pracy et al. 2005) a trend where galaxies near the cluster centers are brighter than those in the outskirts. Although our halos may not be considered as clusters, the comparison of both systems of galaxies would be equally fruitful if we keep in mind possible differences in masses and

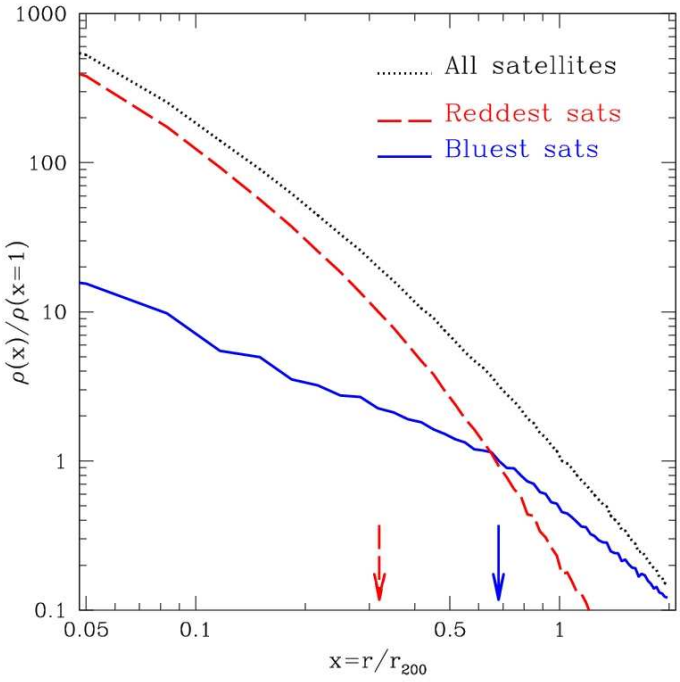

Figure 4. Number density profiles according to satellite colors. We split satellites within $r < r_{200}$ into three roughly equal−number (∼ 84000) subsamples of increasing color indexes. Here we show the profiles corresponding to the 33% bluest (reddest) objects in solid blue (dashed red) curve. Color cuts correspond to $(g-r) < 0.95$ and $(g-r) > 1.01$. Both subsample number densities has been normalized to the total density of satellites at $r = r_{200}$. For comparison we also show in dotted line the profile obtained including all satellites (figure 3). Red satellites are more centrally concentrated with a radius enclosing half of satellites within r_{200} equal to $\sim 0.32 r_{200}$, significantly smaller than the $r \sim 0.71 r_{200}$

environments involved. We have therefore computed the average relative luminosity of satellites, (L^{sat}/L^{host}), as a function of $x = r/r_{200}$. We analyze this relation in different bins of host luminosity, consequently we divide the host sample into faint, intermediate and bright subsample hosts ($\log(L/L_\odot) < 10.3$, $10.3 < \log(L/L_\odot) < 10.6$ and $\log(L/L_\odot) > 10.6$, respectively). Here we must be careful in order to make a fair comparison between these subsamples, since due to the absolute magnitude limit of the satellites ($M_r^{sat} < -17$), we are able to detect fewer satellites in low luminosity primaries. Therefore, we have considered different $\Delta M = M_r^{sat} - M_r^{host}$ intervals: $2 < \Delta M < X$, with X=3.5, 4.5 and 5.5, where only the hosts brighter than $M_r^{host} = -17 - X$ are taken into account in order to obtain unbiased results. We display these curves in figure 5, where cyan, blue and red lines correspond to increasingly bright hosts. We can clearly see by inspection to this figure that satellites closer to the host galaxy tend to be brighter than those located further, although this luminosity segregation becomes evident only when a wide range in ΔM is considered ($\Delta M \geqslant 2.5$). We also notice from this figure that this trend does not depend on host luminosity, once the previously mentioned restrictions to satellite−host relative magnitudes are taken into account. The obtained luminosity segregation of satellites could be possibly explained as a consequence of differential orbital decay induced by dynamical friction. The more massive objects are expected to sink quicker into the central regions of host halos, so that the most luminous satellites, which are likely to be the most massive at the time of first infall onto the host, are the most affected by dynamical friction. A careful de−contamination of background galaxies together with a large magnitude range and a large statistical sample of analyzed systems are likely to be required in order to confirm these results from observational data.

2.4.3 *Satellite Velocities*

As explained in Section 2.3.2, the host galaxy sample includes a small fraction (less than $\sim 1\%$) of primaries that are of non−central type (i.e., they are orbiting within the potential of some larger mass system of galaxies). We exclude in this subsection satellites associated with non−central hosts, since their kinematics respond not only to the host galaxy potential, but also to the potential well of the whole galaxy system where they are orbiting. We shall thereafter consider only satellites associated to central hosts.

Satellite velocity dispersions

We show the satellite radial velocities, V_r as a function of distance in figure 6. Both velocities and distances have been normalized to host virial values V_{200} and r_{200}. The solid line indicates the median of the distribution as a function of $x = r/r_{200}$, while dashed curves indicate the 25% and 75% percentiles. As expected, satellites in the central regions exhibit a large radial velocity dispersion, σ_r, which tends to decline from center outwards. For distances larger than r_{200}, there exists an excess of satellites with negative V_r likely to be objects in their first−infall onto their hosts, which confirms the presence of a strong satellite infall onto host halos on scales $r > 1.5r_{200}$. We show the distribution of radial velocities for different distance ranges

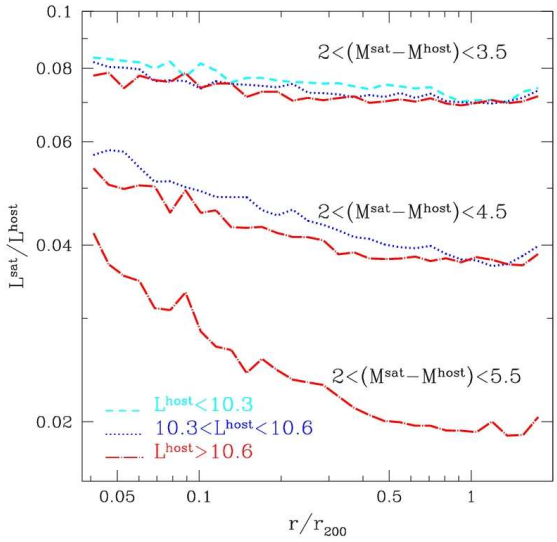

Figure 5. Mean satellite luminosity (in units of L^{host}) as a function of radius. We have taken satellites in different relative−magnitude ranges (see labels on top of lines). In each range ($2 \leqslant \Delta M \leqslant XX$), only hosts brighter than $-17 - XX$ have been considered. This means that in $XX = 4.5$ there exist no hosts with $L \leqslant 10.3$ (cyan line) and in $XX = 5.5$ only hosts with $L \geqslant 10.6$ ($Mr < -22.1$) are considered.

in figure 7. We have fit Gaussian profiles to the distribution of satellite radial velocities which are shown as dashed lines. The distributions show that satellite velocities are well approximated by a single Gaussian only for distances smaller than the virial radius of the host (upper panels). On the contrary, at larger separations ($x \geqslant 1$) it is required a second Gaussian to suitably reproduce the infalling satellite population shown in figure 6. This was performed by adding up a zero−mean Gaussian function with dispersion σ_0 plus a second one with negative mean and dispersion σ_-. The mean values are shown as vertical dotted lines in figure 7 and the dispersions, σ_0 and σ_-, are quoted in all panels. Table 3 also contains the skewness and kurtosis of both distributions in each distance range. As may be seen in figure 7, satellite radial velocity distributions change from wide Gaussian functions in the inner host halo regions to strongly peaked distributions, as the relative importance of satellite infall velocities increases in the external regions. Interestingly, dark matter particles in halos show a very similar velocity behavior (Wojtak et al. 2005).

The presence of this cold population on the external regions of hosts may be related to the existence and possible detection of *caustics* on dark matter halos. The spherically infall model for the collapse of objects in a universe dominated by collisionless particles (Gunn & Gott 1972, Gott 1975, Gunn 1977, Bertschinger 1985) predicts the existence of two well defined regimes, an internal region with a large velocity dispersion, and the external one limited by the turn around radius, characterized by a cold infall of particles. The transition between these two states are determined by very high density boundaries, the caustics. While numerical simulations need to achieve very

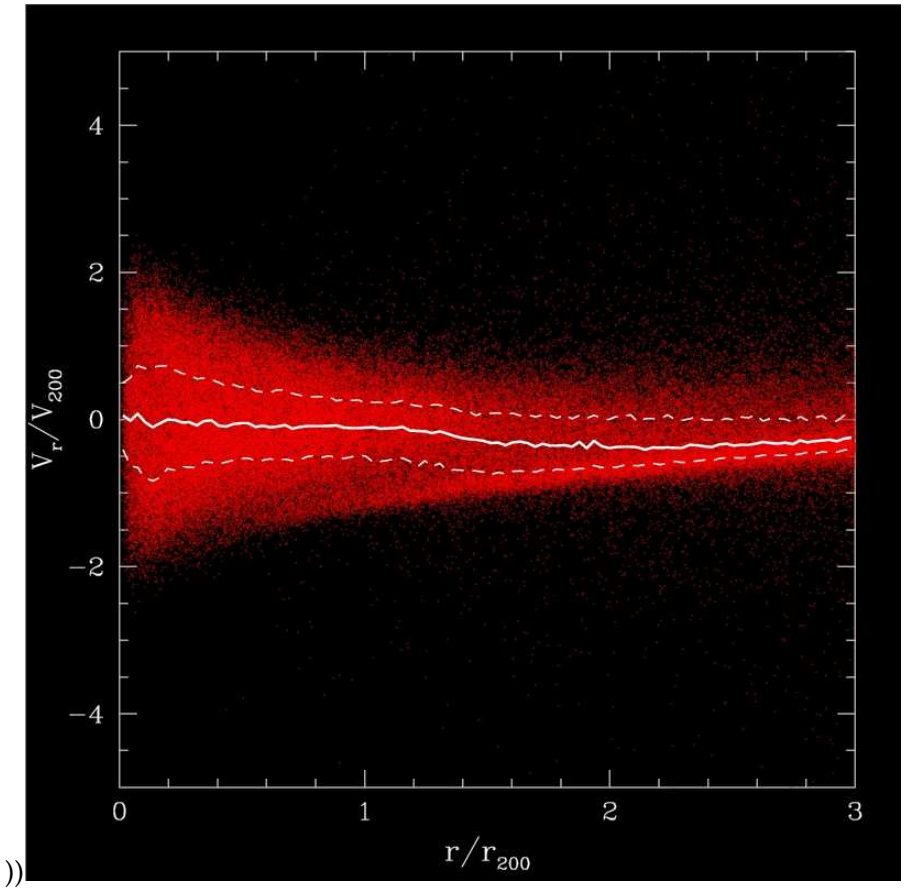

))

Figure 6. V_r/V_{200} as function of r/r_{200} for Millennium satellites. Solid curve shows the median of the distribution, while dashed lines correspond to 25% and 75% percentiles as function of radius.

high spatial and mass resolutions in order to detect these caustics, in observations it can be done through a variety of methods, including overdensities of baryonic matter placed at caustic positions, bumps in galactic rotation curves, an enhanced in the WIMP annihilation signal and also through distortions on gravitational lensing patterns (Natarajan & Sikivie 2005, Mohayaee et al. 2006a and references therein). Unfortunately, projection effects, asymmetries and peculiar velocities make these caustic evidences very difficult to detect. Nevertheless, there still exist some evidence of these caustics coming from observational data. For instance, Mahdavi et al. 2005 using the Canada−France−Hawaii and Keck I telescopes were able to obtain clear evidence of the two distinct velocity dispersion regimes in a group of galaxies. The detection of caustics in numerical simulations has been unsuccessful, due in part for the lack of the numerical resolution needed (Moore 2001, Mohayaee & Shandarin 2006) . Our analysis might shed some light on this regard, since it reveals that cold infall of satellites is a very common feature in the external regions of dark matter halos of isolated primaries, with velocity dispersions ranging from $\sim 20\%$ to $\sim 40\%$ of the infall velocities. However, if satellite velocities does not significantly differ from dark matter particle velocities, we notice that the *coldness* of the infalling matter may not be as high as required (less than 10%, see Moore 2001) in order to make the caustic density enhancements appreciable in dark matter halos.

A full characterization of satellite velocities requires also the analysis of the two remaining spherical components of V^{sat}:, V_ϕ and V_θ. In what follows and in order to simplify the interpretation, we rotate all systems so that the host halo angular momentum lies along the *z−coordinate* axis and define the azimuthal spherical angle ϕ to increase in the same sense as the host rotation. In figure 8 we show V_θ (top) and V_ϕ (bottom) distributions for the same distance bins as in figure 7. Inspired by the radial component analysis, we have divided satellites into two Gaussian subsamples, zero−mean velocity (hereafter *ZMV*) and infalling (hereafter *INF*) satellites. More precisely, we consider for each satellite its V_r component and compute the probability of being a member of either, the *ZMV* or the *INF* Gaussian subsamples resulting from the fits of figure 7. Once more, we compare with Gaussian functions the obtained V_θ and V_ϕ distributions of both satellite subsamples, finding the best−fitting parameters $\bar{V_\theta}$, σ_θ and $\bar{V_\phi}$, σ_Φ respectively. The mean values are shown as vertical dashed lines and the dispersions are quoted in all panels. Skewness and kurtosis are listed in table 3 Notice that for $r < r_{200}$ a double−Gaussian fit to the V_r distribution is not required, so that all satellites are considered to belong to the *ZMV* subsample. In the upper panel of figure 8 we can see that the θ component of satellite velocities is roughly well approximated by Gaussian functions centered on $V_\theta \sim 0$ over almost all distance ranges, although for $r < r_{200}$ the velocity distribution is slightly more peaked than a Gaussian function of the same dispersion.

We repeat this analysis also for V_ϕ (see bottom panel of figure 8). In this case we observe that, contrary to previously studied velocity components, V_ϕ has a highly skewed distribution, showing a clear preference for satellites to co−rotate with the host halo. This is supported also by the positive (non−zero) mean values of the distributions in all distance ranges (see table 3). It is of interest to explore which satellite population is mainly driving this behavior in V_ϕ. By comparing *ZMV* (solid) and *INF* (dashed)

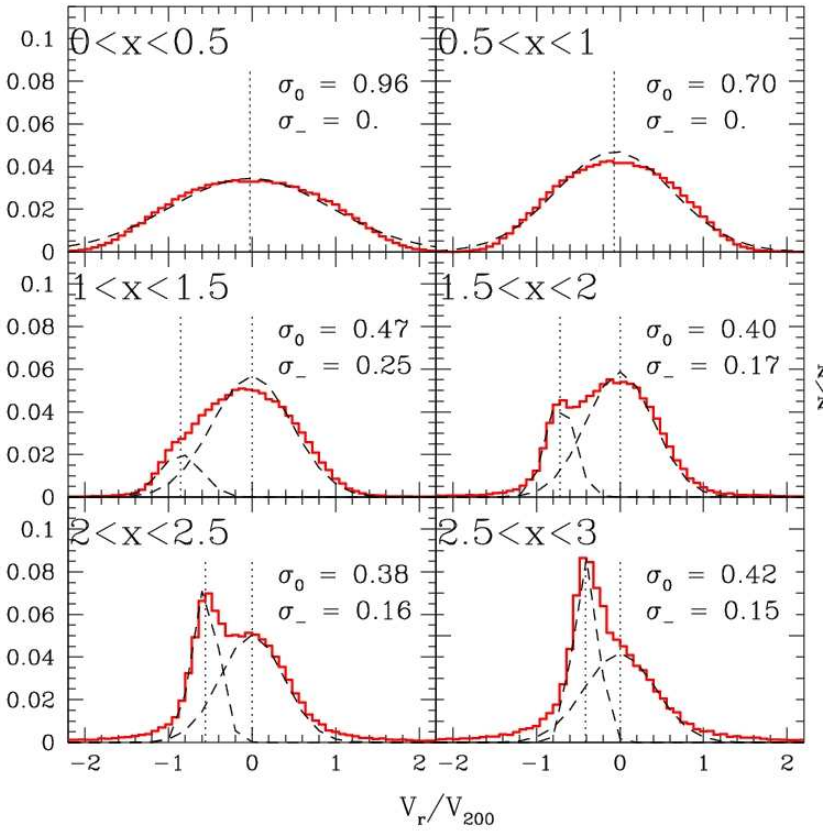

Figure 7. Radial velocity distribution in different distance bins. Only satellites belonging to central hosts have been considered. Upper left labels indicate the x range considered, where $x = r/r_{200}$. In dashed line we show a double−Gaussian fit to the distributions (for $x \geqslant 1$, within the virial radius only 1 Gaussian function is needed). For $x \geqslant 1$, we proceeded as follows: we fit a zero−mean Gaussian, subtract it and then fit another Gaussian to the remainder. Mean values are shown as dotted vertical lines, while dispersion values of both Gaussian are quoted in each panel.

subsamples we can see that those satellites included in the zero−mean velocity subsample have the more skewed distribution, with skewness values almost twice larger than the infalling population, an effect present out to $2.5r_{200}$. On the other hand, infalling satellites are characterized by more symmetrical distributions, with lower velocity dispersions than the *ZMV* population in the external halo regions ($x > 1.5$). Notice that this also occurs in the θ component (top panel of the same figure). We can explain this as a simple consequence of the selection procedure, since by construction infalling satellites are a colder population compared than the *ZMV* subsample (with velocity dispersions up to ∼2.5 times lower), and therefore, we should expect this behavior not only on V_r but also in the other two spherical components θ and ϕ.

The anisotropy parameter of satellite orbits

The comparison of the three components of satellite velocity dispersions as a function of radius allows us to characterize their orbits by means of the *anisotropy parameter* β (Binney & Tremaine 1987). β is defined as $\beta = 1 - \sigma_t^2/(2\sigma_r^2)$, where $\sigma_t = \sigma_\phi^2 + \sigma_\theta^2$, indicating for $\beta \sim 1$ a predominance of the radial component over the other two, i.e. the case for very eccentric orbits, while for isotropic orbits we expect $\beta \sim 0$. Figure 9 shows σ_r, σ_θ and σ_ϕ profiles (upper panel), and the resulting anisotropy parameter as a function of radius (bottom). As in density profile case, host−satellites systems have been stacked after a re−scaling of position and velocities to host virial values, in order to obtain the average $V_{r,\theta,\phi}$ behaviors. The three spherical components of satellite velocity dispersion decline substantially from the center outwards by typically a factor $\simeq 1.5 - 2.$ at the host virial radius. Within this region, the radial dispersion is significantly larger than σ_θ and σ_ϕ, indicating a positive anisotropy parameter β. However, this is not longer true for distances larger than r_{200}, where the three components of the satellite velocity dispersion start to be comparable, and then, β approach 0 at $r \sim 2r_{200}$.

The behavior of β in the bottom panel of figure 9 is quite different from that reported in previous work (see Wojtak et al. 2005, Diemand et al. 2004 and 2005, Faltenbacher & Mathews 2006), who find both dark matter particles and also subhalos to have an anisotropy parameter profile that increases with radius. Contrary to this, our satellite sample shows that β reaches a maximum at $r \sim 0.3r_{200}$ and declines beyond this radius approaching $\beta \sim 0$ at the virial radius. The explanation for this drop in β may come from the mixing of satellites with dark matter subhalos (W−SUB) and those with no attached subhalos (N−SUB). We have explored the three spherical components of the velocity dispersion of these two satellite populations separately finding: *a*) $\sigma_{r,\theta,\phi}$ are larger for W−SUB than for N−SUB satellites in approximately ∼ 20% for the radial component and ∼ 50% in both angular coordinates, and *b*) that both anisotropy profiles are approximately constant in the external regions, although for all radii satellites without subhalo have higher β values than satellites with bounded substructure ($\beta \sim 0.5$ and ~ 0.13 at $r = r_{200}$ respectively, see bottom panel of figure 9). As the relative fraction of satellites with subhalos increases with distance (see figure 3), the total β profile is completely dominated in the inner regions by the anisotropy parameter of satellites with no dark matter subhalo, and changes to the typical β values of W−SUB satellites for $r \geqslant 0.5$, resulting in the declining anisotropy profile

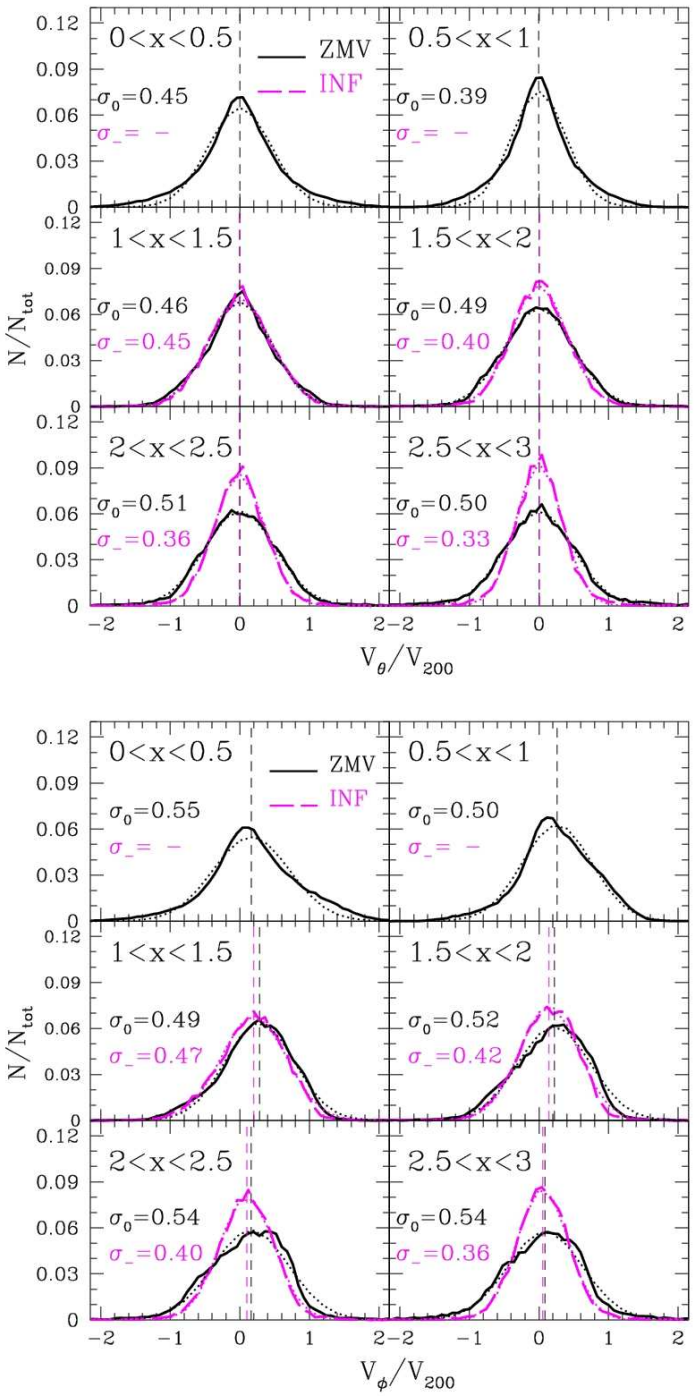

Figure 8. V_θ and V_ϕ distributions dividing the satellite sample into infalling (long–dashed lines) and 'zero–mean velocity' (solid lines) subsamples according to the double–Gaussian function fit in the radial velocity distributions (figure 7). Notice that for satellites within r_{200} we cannot define two Gaussian functions and then we include all satellites in the 'main Gaussian' subsample. Gaussian functions have been fit to these distributions (dotted curves), mean values are shown in short–dashed lines while sigma values are quoted in each panel.

COMPONENT	$x = r/r_{200}$	MEAN	σ	SKEWNESS	KURTOSIS
V_r	0.0-0.5	-0.01 (–)	0.96 (–)	0.02 (–)	-0.67 (–)
	0.5-1.0	-0.07 (–)	0.70 (–)	0.00 (–)	-0.52 (–)
	1.0-1.5	0.0 (-0.84)	0.47 (0.25)	0.00 (0.16)	0.79 (1.14)
	1.5-2.0	0.01 (-0.72)	0.40 (0.17)	-0.11 (-0.11)	3.16 (0.41)
	2.0-2.5	-0.01 (-0.56)	0.38 (0.16)	0.01 (-0.13)	4.56 (0.36)
	2.5-3.0	-0.03 (-0.41)	0.42 (0.15)	-0.10 (-0.01)	3.56 (0.19)
V_θ	0.0-0.5	0.00 (–)	0.45 (–)	0.00 (–)	0.98 (–)
	0.5-1.0	0.00 (–)	0.39 (–)	0.01 (–)	0.77 (–)
	1.0-1.5	0.00 (0.00)	0.46 (0.45)	-0.01 (0.09)	0.66 (0.91)
	1.5-2.0	0.00 (0.00)	0.49 (0.40)	-0.04 (0.04)	1.42 (1.44)
	2.0-2.5	0.00 (-0.01)	0.51 (0.36)	-0.12 (-0.06)	2.37 (3.10)
	2.5-3.0	0.00 (0.00)	0.50 (0.33)	0.034 (0.14)	2.52 (3.87)
V_ϕ	0.0-0.5	0.20 (–)	0.55 (–)	-0.02 (–)	0.48 (–)
	0.5-1.0	0.25 (–)	0.50 (–)	-0.26 (–)	0.40 (–)
	1.0-1.5	0.22 (0.16)	0.49 (0.47)	-0.42 (-0.28)	0.58 (0.52)
	1.5-2.0	0.16 (0.11)	0.52 (0.42)	-0.38 (-0.20)	0.94 (1.74)
	2.0-2.5	0.10 (0.08)	0.54 (0.40)	-0.29 (-0.16)	1.95 (2.75)
	2.5-3.0	0.06 (0.05	0.54 (0.36)	-0.09 (-0.15)	2.33 (3.41)

Table 3. Parameters of the Gaussian distribution fits to the satellite velocities (in its three spherical components) up to $r = 3r_{200}$. Middle lines divide from top to bottom the radial (V_r), polar (V_θ) and azimuthal (V_ϕ) components of V^{sat}. We show both the values corresponding to the zero-mean velocity sample, ZMV, and between parenthesis those that best reproduce the velocity distributions of the infalling satellite population, INF.

shown in figure 9. Nevertheless, we need to understand why satellites with no dark matter particles lie on more radial orbits than those who still conserve their subhalo. We could naturally expect stripped satellites orbiting far from the hosts to have highly radial motions, since we need small pericenter distances for the tidal forces to be effective at removing material from satellites. Therefore, the only possibility for a satellite who has lost their dark matter content of having large apocenter distances is to have very radial orbits, that push it from very small pericenters (where the stripping occurs) to large separations from the host at apocenters. On the other hand, satellites with bound dark matter particles must maintain themselves as far as possible from the center of the host potential in order to retain their subhalo, and then, we expect them to be moving on more circular orbits (lower β parameters). There is another factor contributing to more isotropic velocities in the outskirts of halos, and is related to the increasing presence of satellites in their first infall as one moves further from the host galaxy. These recently accreted satellites are flowing into the hosts with the intrinsic velocity of the surrounding field, which is typically $\sim 50\%$ of the host virial velocity (see figure 9), and is characterized by no preferred direction. Due to their isotropic velocity dispersions together with their relatively late accretion times and large separations from the hosts, this satellite population on the first infall phase is very likely to conserve their dark matter component, causing S−SUB satellites to lie on quite circular orbits as found here.

Predictions from the Jeans formalism

The so far studied properties of the satellite galaxies allow us to predict the circular velocity V_c expected for the dark matter host halos through the well known Jeans formalism (Binney & Tremaine 1987). In its spherical approximation, the Jeans equation relates the density ($\rho(r)$), the velocity anisotropy ($\beta(r)$) and the radial velocity dispersion ($\sigma_r(r)$) profiles of some observable tracer population to the circular velocity of the dark matter halo that hosts it. More specifically, we have:

$$V_c^2 = -\sigma_r^2\left(\frac{dln\rho}{dlnr} + \frac{dln\sigma_r^2}{dlnr} + 2\beta\right) \tag{2.1}$$

using ρ, β and σ_r of satellites, in order to obtain a prediction for the typical circular velocity of the host halos. We show in figure 10 all the quantities taking part of equation 2.1. In order to obtain a less noisy first derivative for velocity dispersion, we have used an analytical function of the form: $\sigma_r = \sigma_0 + (x/x_0)exp(-(x/x_0)^\alpha)$ with best−fitting parameters $x_0 = 0.068$, $\alpha = 3/4$ and $\sigma_0 = 0.6$ km/s. We see from this figure that the proposed fit (magenta dotted line) suitably reproduces the behavior of the satellite radial velocity dispersion at all radii, and also all terms of equation 2.1 are reasonably smooth functions.

In CDM models, the dark matter in halos follows a NFW−like density profile inside the virial radius (Navarro, Frenk & White 1997). This matter distribution implies a very well defined circular velocity profile for the dark matter particles that we can compare to the circular velocity obtained using satellites as tracers in the Jeans equation (eq. 2.1). Figure 11 shows this, where solid line corresponds to Jeans predictions, while

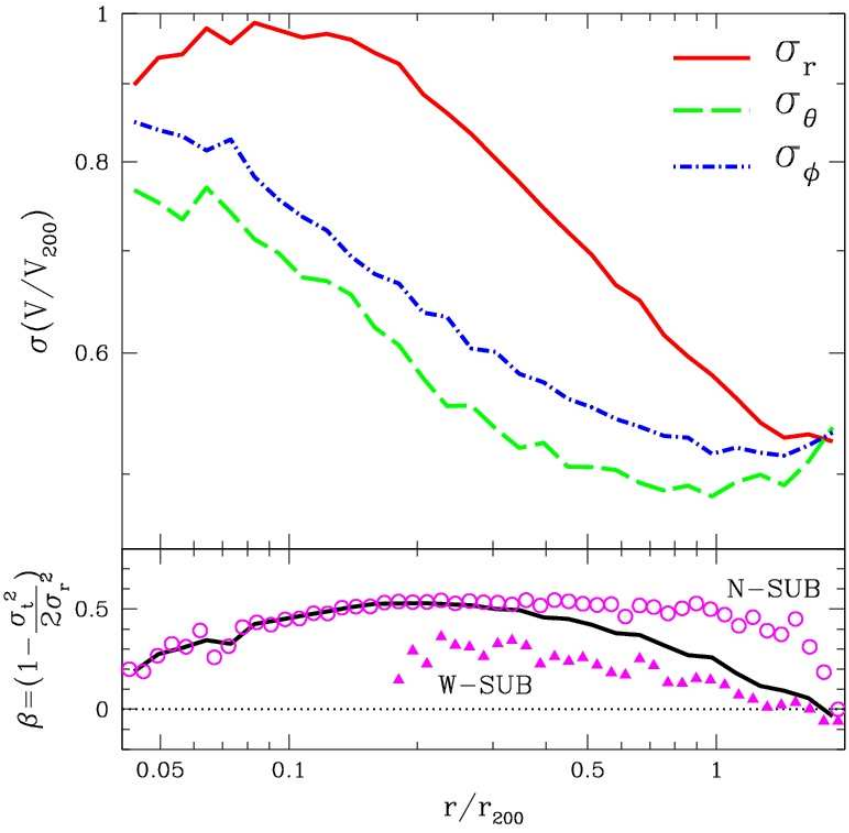

Figure 9. Mean spherical components of velocity dispersion as a function of radius up to 2 times r_{200}. It is computed by stacking all satellites associated to central hosts. Errors are included, but they are smaller than line width. Lower panel shows in solid line the anisotropy parameter defined as: $\beta = 1 - {\sigma_t}^2/2{\sigma_r}^2$, where ${\sigma_t}^2 = \sigma_\theta^2 + \sigma_\phi^2$ of the total sample. Filled triangles and open circles indicate the β profile corresponding to satellites with and without dark matter subhalo respectively.

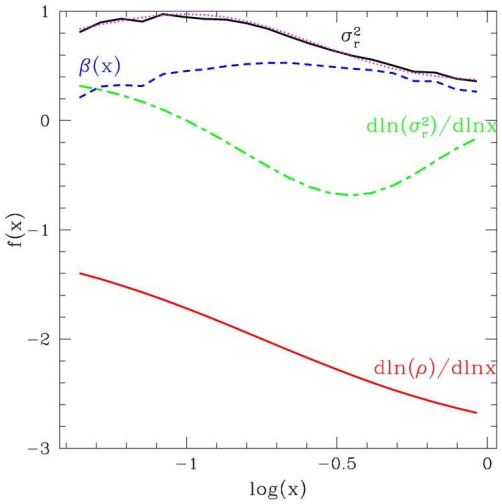

Figure 10. Quantities that take part in the Jeans's equation. Magenta dotted line shows the fit to σ_r of the form: $\sigma_r = \sigma_0 + (x/x_0)exp(-(x/x_0)^\alpha)$. Best−fitting parameters are: $x_0 = 0.068$, $\alpha = 3/4$ and $\sigma_0 = 0.6$ km/s.

magenta dotted curves show the circular velocity profile associated to NFW halos of concentrations $c = 5.6, 7$ and 8.4 (accordingly to the previously studied satellite number density profile and the $M_{200} - c$ relation found in Millennium halos, see 3.2). This figure indicates that the Jeans formalism applied to satellite kinematics predicts a circular velocity profile that rises in the inner regions, reaches a maximum V_c^{max} at $r \sim 0.3 r_{200}$ and steadily declines beyond this to $65 - 70\%$ of V_c^{max} at $r \sim r_{200}$. This behavior is broadly consistent with the circular velocity profile expected for an NFW halo and the location of the maximum suggests a concentration of $c \sim 7$, in reasonable agreement with the $c \sim 8.4$ expected for the dark matter particles in the host halos.

Satellite velocity dispersions and the L−σ relation of hosts

What is the typical velocity dispersion of satellites orbiting around hosts of a given luminosity?. In figure 12 we show in panel a) (black solid curve) the average σ[3] of all satellites within r_{200} for different bins of the host galaxy luminosity. As we can see, both quantities are not related through a simple power law but instead the slope changes at approximately $\log(L/L_\odot) \sim 10.8$ (dotted lines indicate two power−laws $L \propto \sigma^{2,3}$ in order to guide the eye). For hosts fainter than this luminosity we find $L \propto \sigma^{2.2}$ with velocity dispersions below 200 km/s, whereas for bright hosts the relation is shallower, showing $L \propto \sigma^{1.1}$. We argue that this break in the $L - \sigma$ relation is due to the increasing relevance of satellite luminosities on the total luminosity (L^{system}) of each system as we move towards brighter hosts. The total luminosity of

3 During this subsection we refer to σ meaning the 1D velocity dispersion of satellites, σ_{1D}. It is computed as $\sigma_{1D}^2 = 1/3(\sigma_x^2 + \sigma_y^2 + \sigma_z^2)$ by stacking all considered satellites after re−scaling their positions and velocities to r_{200} and v_{200} respectively.

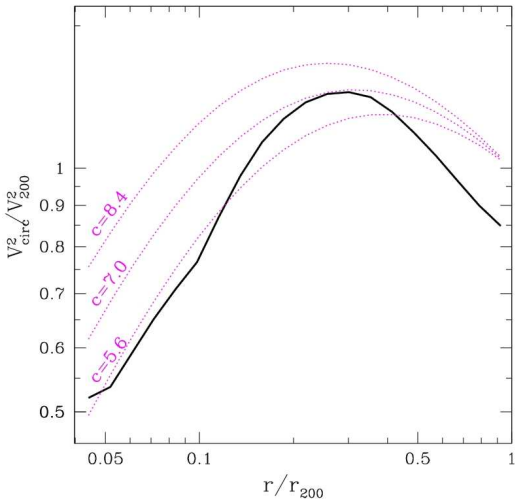

Figure 11. Circular velocity profile obtained from the Jeans equation. For comparison we also show the V_c profiles expected for NFW halos of concentrations $c = 5.6$, 7 and 8.4.

a bound system is computed by summing up the contribution of all galaxy members within the virial radius, and we expect this L^{system} to be strongly related with the system total mass M_{vir}, and through this, also with their velocity dispersions since $M_{vir} \propto \sigma^3$. In our sample, the fraction of L^{system} that corresponds to the host galaxy luminosity ranges from 99% to 40% as we increase host luminosity. Consequently, for bright hosts their luminosity is more weakly related to the system velocity dispersion than for faint ones (where L^{host} dominate the total luminosity), resulting in the flattening of the $L - \sigma$ relation seen in figure 12. As an additional test for this, we have computed the $L - \sigma$ relation for those systems where the primary luminosity represents more than 70%, 85% and 95% of the total luminosity L^{system} and show them in panels b), c) and d) of figure 12 respectively. As it can be seen the $L - \sigma$ relation becomes progressively steeper as we consider only primary galaxies that dominate the total luminosity of each system; i.e., we have $L \sim \sigma^2$ if all systems are included (panel a)) whereas $L \propto \sigma^3$ (in agreement with theoretical expectations) is found when restricting to hosts with $L^{host} > 0.9L^{sys}$ (panel d)). This suggests that for the brightest primaries ($L^{host} > 10^{10.8} L_\odot$) we are switching from single galactic halos ($\sigma < 200$ km/s) to the regime of group and cluster sized halos characterized by higher velocity dispersions. This findings support the observational results from the recent work of Eke et al. 2006. These authors study the relation between the velocity dispersion and luminosity of the brightest member of galaxy groups from the 2PIGG catalog and a mock sample, comparing this with the expected galaxy rotation velocity inferred from the well known Tully Fisher relation. They conclude that for low luminous hosts these two velocities differ by less than 20%, while for bright hosts the rotational speed may represent only 10% of the typical circular velocity speed of halos hosting brightest galaxies of the same luminosity. This stresses the poor relation

between the brightest galaxy and the halo mass at the bright end of the halo mass function.

The interpretation of the $L-\sigma$ relation is complicated further for the large spread in the $L-M$ relation analyzed in Section 3.1. We have found that applying color cuts to the isolated galaxies sample we are actually constraining the mass of the halo in which galaxies live. We therefore expect the satellite velocity dispersions of red, intermediate and blue hosts to be different as a consequence of this. We show in a)-d) panels of figure 12 the $L-\sigma$ relation for the previously defined color host subsamples using blue short dashed ($(g-r) < 0.65$), green long dashed ($0.65 \leqslant (g-r) \leqslant 0.95$) and red dot−dashed lines ($(g-r) > 0.95$). The three sequences split in the $L-\sigma$ plane as expected, with increasingly higher velocity dispersions associated to the redder hosts. The differences are quite appreciable, with satellites of blue hosts moving typically with half of the speed of satellites associated to red hosts of the same luminosity. This difference could be even larger in the case of brighter hosts, where the inclusion of group and cluster sized halos starts to dominate the statistics. An interesting feature seen in figure 12 is the single power−law relation that follow the hosts included in the blue subsample in each panel, that stands out over all the luminosity range. This clearly differ from the other two sequences, who show the break in the $L-\sigma$ relation we have found when all hosts were taken into account. We notice that velocity dispersions of blue hosts are always below $\sim$ 200 km/s, the transition value from galactic to group−sized halos we find for the full host sample, and therefore a change in the slope for them is not very likely to occur. This suggests that blue hosts tend to live *typically* in low mass galactic−sized halos with σ between 100−200 km/s and surrounded only by faint satellites (since the no−break behavior here implies that L^{host} is very close to the total luminosity of the system). For intermediate color hosts, the satellite contribution to L^{system} is unimportant for hosts fainter than $6x10^{10}L_{\odot}$, and beyond this we start to include in our sample group−like systems rather than single primary galaxies with their satellites orbiting around them. For the reddest host subsample this threshold moves to $4x10^{10}L_{\odot}$, reflecting the tendency of early−type red−color galaxies to always lie on massive multiple galaxy systems.

We repeated this analysis of satellite velocity dispersions but now as a function of host stellar masses instead of luminosities, also splitting the sample according to host color indexes. Results are displayed in figure 13 and lines and color coding is used as in figure 12. We obtain as before no consistence with a single power−law, finding a break point towards $\sigma \sim 200$ km/s. However, unless the $L-\sigma$ case, now all host color sequences (red, intermediate and blue) do indeed show a change of slope in the $M_{str}-\sigma$. We study the $M_{str}-M_{200}$ relation of hosts and find that the mass in stars of a given galaxy is a better estimator of the virial mass of the halo than their luminosities, in the sense that it shows significant less scatter than the $L-M_{200}$ plot of figure 1. As a consequence of this, the shift in velocity dispersion between primaries of different color basically disappears when stellar masses are considered instead of r-band luminosities. Using, whenever possible, stellar mass estimates rather than luminosity in order to bin galaxies is likely to give more robust results in observational studies. The change of slope for $\sigma \sim 200$ km/s seen in figure 13 is also here a consequence of plotting the host stellar masses instead of the whole

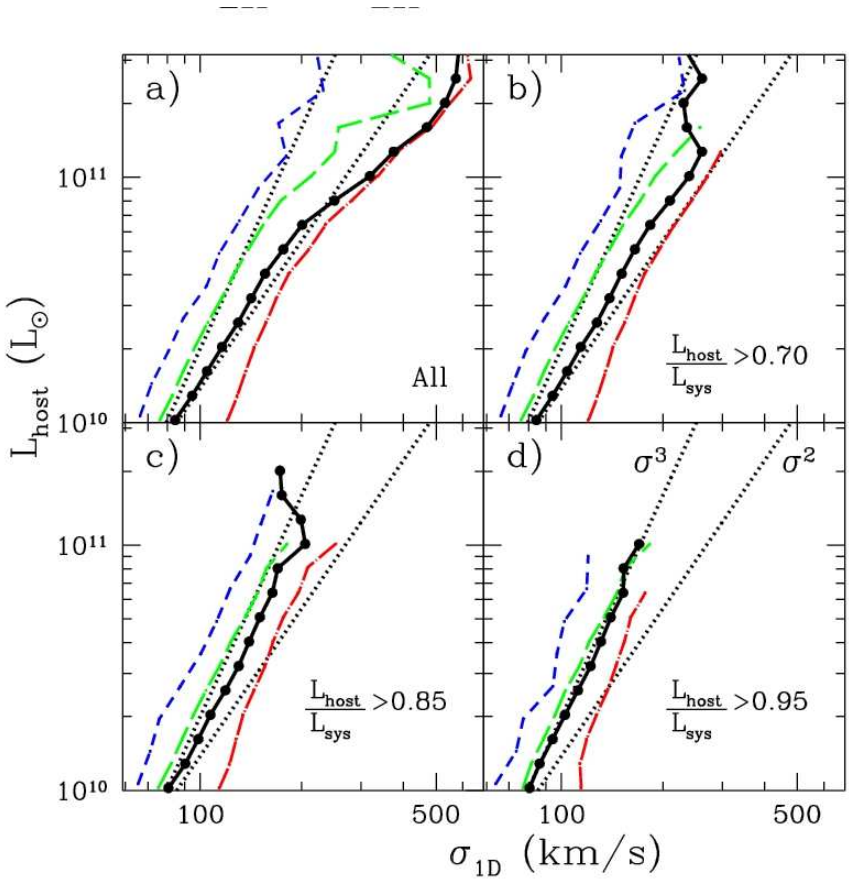

Figure 12. 1D velocity dispersion of satellites within r_{200} as a function of host luminosity (black solid line). We need two power−laws in order to reproduce this curve (see dotted line), with slopes $L \propto \sigma^{2.2}$ and $L \propto \sigma^{1.1}$ for low and high luminosity ranges respectively. This break may be associated to a transition between single galaxy halos and group−like halos (see text below). Error bars are bootstrap re−sampling of the data. We also show the luminosity−satellite velocity dispersion of hosts when they are split in three subsamples according to the color cuts applied in Section 3.1.

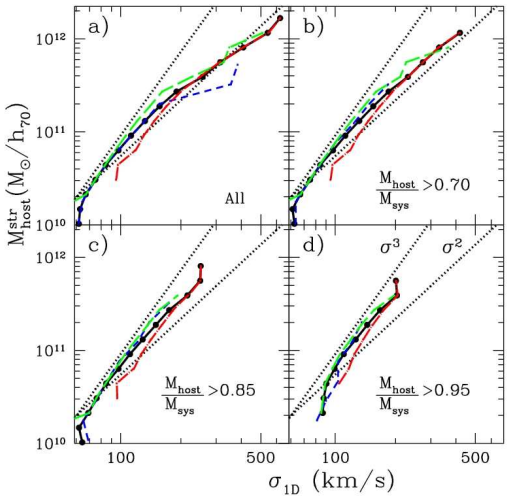

Figure 13. Same as figure 12 but using the stellar mass of the hosts instead of their luminosities.

system stellar mass. When satellite contributions are included into M_{str}^{system} we find a single power−law behavior of the form $M_{str} \propto \sigma^{2.5}$, with a less pronounced shift on the satellite velocity dispersion between different host color subsamples than in the $L - \sigma$ relation shown in figure 12.

2.4.4 *Satellite Orbits and Alignments*

In this Section we analyze how satellite orbits and angular positions are related to the orientation of the host halo angular momentum. The angular momentum in dark matter halos is determined by tidal torques from the infalling material (Peebles 1969, Barnes & Efstathiou 1987) and the cumulative acquisition of angular momentum from satellite accretion (Vitvitska et al. 2002). Recent numerical simulations have found that ∼ 60% of satellites are orbiting in a pro−grade sense compared to the angular momentum of their host halo (Azzaro et al. 2006, Warnick & Knebe 2006). Our previous analysis of Section 2.4.3 revealed that satellite orbits are not randomly oriented, as shown by the slightly skewed distribution of the ϕ component of satellite velocities (see lower panel of figure 8). We explore further the orientation of satellite orbits in figure 14. We define as α the angle subtended by the orbital rotation axis of satellites, L_{orb}^{sat}, and the host halo spin, J^{host}. A measure of the correlation between satellite orbit orientation and the host angular momentum vector is provided by: $\cos(\alpha) = L_{orb}^{sat}.J^{host}/(|L_{orb}^{sat}||J^{host}|)$. Satellites orbiting pro−grade have $\cos(\alpha) > 0$ while negative values indicate an anti−alignment between the satellite orbit and J^{host}. The different panels in figure 14 show $\cos(\alpha)$ distributions for several bins of satellite separations up to 1.5 times r_{200}. We also distinguish between satellites who have lost (shaded magenta histograms) or retained (black curves) their dark matter subhalos (subsamples N−SUB and W−SUB respectively) in order to test if different

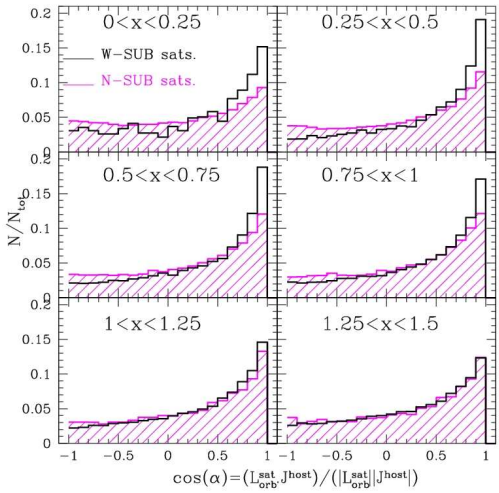

Figure 14. Distributions of satellite orbit orientations for different ranges of satellite distances. α is the angle formed by the satellite orbital angular momentum, L_{orb}^{sat}, and the host halo particles angular momentum, J^{host}. Black solid lines and magenta shaded histograms show satellites with and without subhalos (W−SUB and N−SUB) respectively. We see the clear trend of satellites to move on orbits co−rotating with J^{host} up to distances $\sim 1.5R_{vir}$.

orbit orientations may significant favor the stripping of the dark matter component on the N−SUB satellite subsample. This figure shows a clear tendency of satellites to move in pro−grade sense (positive $\cos(\alpha)$ values) following the host halo particle rotation. No significant difference is found for magenta and black-shaded histograms showing that the trend is almost independent of the satellite dark matter content. The average fractions of satellites with positive $\cos(\alpha)$ values are $\sim$ 72% and $\sim$ 65% for satellites with and without dark matter subhalo respectively. This effect is somewhat stronger than that previously reported by Azzaro et al. (2006) and Warnick & Knebe (2006) of $\sim$ 60%. Notice that this preference for co−rotating orbits is only weakly dependent on satellite distances to the host up to $1.5r_{200}$, in agreement with the Warnick & Knebe (2006) findings. This highlights the important role of the large scale tidal fields in the determination of the host angular momentum.

Galaxies and subhalos in numerical simulations show anisotropies in their distribution within host halos, with an excess of satellites preferentially aligned with the major axis of their hosts (Knebe et al. 2004, Zentner et al. 2005, Wang et al. 2005, Libeskind et al. 2005). Evidence for a preferential satellite alignment with the disk of their central galaxies has also been found in large observational samples of satellite galaxies selected from the 2dFGRS and SDSS (Brainerd 2005, Agustsson & Brainerd 2006, Yang et al. 2006 and references therein). Since we expect a certain degree of correlation between the halo angular momentum and their minor axes (Faltenbacher et al. 2005, Wang et al. 2005), these observational results are in good agreement with numerical simulations once we assume no misalignment between the baryonic and

dark matter angular momentum. This bias towards disk−alignments of satellites in spiral galaxies, constitutes a curious contradiction with what we find in our own galaxy and also in our closest neighbor, M31. The Milky Way has their satellite system in a disk−like structure arranged *perpendicular* to the disk (Libeskind et al. 2005). Also, the Andromeda Galaxy seems to show an anisotropic distribution of satellites with its long−axis approximately at $\sim 60^\circ$ of the M31 disk direction (Koch & Grebel 2006). Besides particular cases, anisotropies in satellite distributions can be understood in terms of the existence of preferred directions for satellite accretion, mostly related to the direction of filaments that fed the host halos. Here we explore possible correlations between satellite positions and J^{host} by stacking several systems according to the host galaxy luminosity. We show this in figure 15, where we compute the distributions of the θ (spherical) component of satellite positions in a system oriented with J^{host} in the z−axis. A fully isotropic distribution of satellites around J^{host} corresponds in this figure to a horizontal line. Hence, the over−abundance of satellites with low values of $|\cos(\theta)|$ seen in figure 15 indicates a tendency of satellites to reside preferentially in the direction perpendicular to the host angular momentum, in agreement with previous numerical results and disk−alignment trends found in observations. This effect is present for all host luminosities, although the anisotropy seems to be larger in the faintest bin ($\log(L/L_\odot) \leqslant 10.3$, blue thick curve). Nevertheless, this dependence on the primary luminosity might not be real but instead a consequence of the lower number of particles used to define J^{host}. The host angular momentum direction is determined by counting all dark matter particles within the virial radius of a given halo. This set of particles also includes those associated with satellites, since substructure has not been removed when computing J^{host}. In the case of low mass (faint) hosts, massive satellites could represent a significant fraction of the host particles, biasing the determination of J^{host} towards a direction perpendicular to their orbital plane. This would cause an artificial increase of the number of satellites with low $|\cos(\theta)|$ values. To disentangle this, we study the distribution of $|\cos(\theta)|$ considering different subsamples: only bright satellites (with $M^{sat} < M^{host} + 3.5$), intermediate ($M^{sat} < M^{host} + 4.5$), and including also faint satellites ($M^{sat} < M^{host} + 5.5$). The results are shown as thick solid, dashed and thin solid lines in figure 15. We obtain a larger anisotropy signal when only bright satellites are considered, partially supporting our hypothesis about the impact of satellite particles in the J^{host} determinations. Due to the simulation resolution, low mass (and likely faint) hosts have only relatively bright satellites ($M^{sat} < M^{host} + 3.5$), so they are more strongly affected by this bias. Based on this we argue that satellite galaxies are preferentially located near the plane perpendicular to the host angular momentum, but further analysis is required in order to confirm (or rule out) any trend of this alignment with the luminosity and mass of the host halos.

2.5 Conclusions from this Chapter

The main conclusions from our study of satellite galaxies in the *Millennium Run* can be summarized as follows:

- Using the selection criteria described in Section 2, the probability for a galaxy

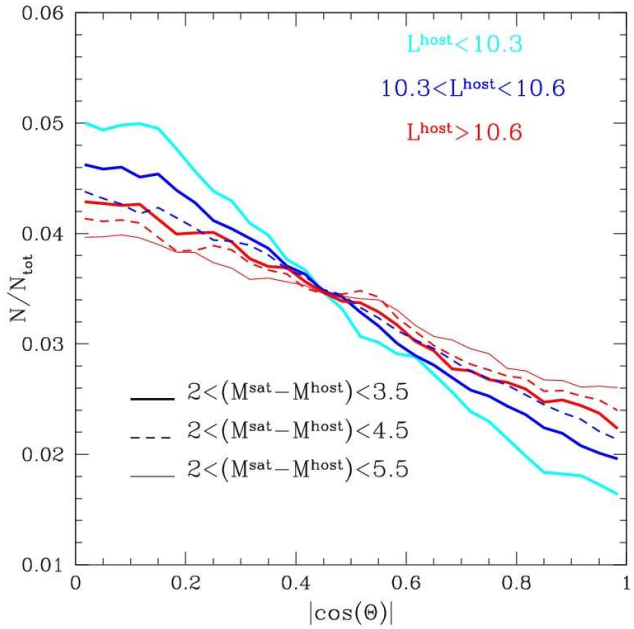

Figure 15. Distribution of $|\cos(\theta)|$, where θ is the polar angle of each satellite in a system oriented with the host angular momentum in the z−axis direction. Satellites are separated according to their host luminosity as in figure 5. We show in different line types the result for satellites within limiting magnitude ranges: $2 \leqslant \Delta M \leqslant XX$, where $XX = 3.5$ (thick solid line), 4.5 (dashed line) and 5.5 (thin solid line). As done in figure 5, we consider only hosts brighter than $-17 - XX$ in order to deal with comparable samples. An isotropic distribution of satellites around hosts corresponds to a horizontal line here, and therefore, the excess of satellites towards zero means a tendency of satellite spatial distribution to be anti−aligned with the host angular momentum.

of being isolated is about $\sim 20\%$, quite independent of its luminosity. On the other hand, the probability that these isolated galaxies host at least one satellite brighter than $M_r < -17$ within their virial radius substantially depends on their luminosity, ranging from 38% (for faint isolated galaxies with $M_r > -21$) up to 92% for the brightest ($M_r < -23$).

• Isolated galaxies of comparable luminosity tend to live in less massive dark matter halos if they do not host any satellite than compared to the case when they do (singles or hosts respectively). Also color indices may differ between these two populations since hosts sample show in comparison a larger fraction of red galaxies than those primaries without satellites.

• Satellite galaxies are radially distributed consistently with an NFW profile of concentration ~ 5.6. This is somewhat shallower than the average expectation for the dark matter particles in *Millennium Run* halos (of about ~ 8.4). However, satellite galaxies are still reasonable good tracers of the underlying dark matter distribution for distances larger than $\sim 0.2 r_{200}$. We find no dependence of the number density profile of satellites on host luminosities, which is in good agreement with previous observational studies based on SDSS data (Chen et al. 2006).

• Satellites suffer strong stripping of their dark matter content while orbiting around the central potentials, specially those located close to their hosts. This implies differences on the radial distribution of all satellite galaxies compared to the distribution of the dark matter subhalos.

• We find that satellite galaxies are distributed differently according to their color indices and luminosities. In the central regions of hosts, satellites tend to be redder than in the outskirts, probably as a combination of earlier accretion times and a stronger and more efficient stripping of their gas. Therefore the radial distribution of red satellites is appreciably steeper in the inner regions than the flat distribution associated with the blue satellite population, which in turn dominates the total profile for $r \geqslant 0.7 r_{200}$. Not only a color but also a luminosity segregation has been found, with satellites in the inner regions being on average brighter than in the external ones, in agreement with some observational studies. However, this radial segregation appears only if a large range of satellite relative magnitudes is resolved.

• The radial component of satellite velocity dispersions have a Gaussian distribution within r_{200}, with a radial dispersion that decreases from the center outwards from $\sigma_r \sim V_{200}$ at $0.1 r_{200}$ to typically $0.55 V_{200}$ at the virial radius. Outside this region a clear infall pattern is present, with satellites falling into host halos with average values $\sigma_r \sim 0.25 - 0.15$ times the virial velocity of their hosts. The satellite V_r distribution is thus well described by a double−Gaussian function for regions outside r_{200}. The angular components of satellite velocities, V_θ and V_ϕ, are also consistent with Gaussian distributions, although the ϕ component shows some skewness due to the preference of satellites to co−rotate.

• Satellite orbits are radially anisotropic, with a maximum $\beta \sim 0.5$. For $r > 0.4 r_{200}$ the inclusion of satellites recently accreted tends to lower this value reducing the radial bias of their orbits. This can be used in combination with the Jeans equation to explore the consistency of the satellite circular velocities with the expected for CDM dark matter halos. The Jeans formalism predicts a raising inner circular velocity profile

that decreases beyond $r \sim 0.4 r_{200}$, in agreement with the behavior of NFW-like density profiles for the underlying dark matter distribution. The location of the maximum suggests a concentration of $c \sim 7$, in reasonable agreement with the $c \sim 8.4$ expected on average for the host halos. The circular velocity inferred using the satellite population as tracers in the Jeans equation is lower than theoretical expectations for distances larger than $\sim 0.4 r_{200}$. This may be attributed to the lack of virial equilibrium that stands on the external regions of halos.

• The $L^{host} - \sigma$ relation shows a double power law−behavior: $L^{host} \propto \sigma^{2.2}$ for $\sigma \leqslant 200$ km/s, and for larger σ values we find a break in the relation that become shallower ($L^{host} \propto \sigma^{1.1}$). This is likely to be caused by the increasing importance of satellite contribution to the total luminosity of the system. This break then can be understood as a transition region between single galactic sized halos to multiple populated group−like halos. When only host galaxies that dominates the total luminosity of the system are taken into account, we find $L^{host} \propto \sigma^3$ in agreement with the scaling laws expected for halos in the CDM cosmology.

• The velocity dispersion of satellites also reflects the large spread in the $M - L$ relation of primaries. On average, satellites associated to blue hosts have $\sigma \leqslant 200$ km/s whereas for the reddest hosts, satellite's velocities almost double this value. When the $M_{str} - \sigma$ relation is analyzed, the difference between blue, intermediate and red galaxies tends to disappear as a consequence of the strong correlation that links M_{str} to M_{vir} in halos.

• Satellites are preferentially moving in a pro−grade sense respect to the host angular momentum, with a percentage of $\sim 65 - 70\%$ of satellites in co−rotating orbits. This effect does not depend on satellite distances up to $1.5 r_{200}$, emphasizing the important role of satellite galaxy accretions on the acquisition of the host angular momentum. Satellite spatial distribution is also correlated with the host angular momentum, showing a mild preference of satellites to be located in the plane perpendicular to the angular momentum of the host, probably aligned with the long axis of the dark matter host halo. This finding is in agreement with previous observational and numerical results.

3

AN IMPROVED SATELLITE IDENTIFICATION METHOD IN GALAXY CATALOGS

3.1 Abstract

We describe a new method for the identification of satellite galaxies in large−scale observational catalogs. It defines adaptively a projected search radius Δ_r to look for candidate satellites around bright isolated hosts. Δ_r is automatically adjusted to the virial mass of the host halo, estimated using the luminosity and color of the primary galaxy. We use a relation of the form $\log(M_{200}/M_\odot) = A\log(L/L_\odot) + B$ (where A and B are a function of the color of the primary) in order to assign virial masses to candidate isolated host halos. We apply this method in first place to a mock galaxy catalog of the *Millennium Run* and find a significant reduction in the number of interlopers misclassified as satellites when compared with a fixed Δ_r identification algorithm. The decontamination is more substantial for the faintest hosts, where the expected fraction of interlopers decreases from $\sim 80\%$ to $\sim 21\%$ of the sample. The completeness level in samples is also improved by up to 30% in the most luminous host galaxies. We apply this algorithm to study the projected radial distribution of satellites around bright hosts. For the mock catalog we find a suitable power law fit over $x = R_p/r_{200}$ of the form $\Sigma(x) \propto x^\alpha$ with $\alpha = -1.5 \pm 0.1$, in good agreement with the value $\alpha = -1.6 \pm 0.1$ obtained by projecting the three−dimensional NFW distribution of satellites found in the previous Chapter. The algorithm, when applied to the SDSS DR4 sample, gives results consistent with these findings ($\alpha = -1.4 \pm 0.2$) for distances $R_p > 0.3r_{200}$, where observational effects such as fiber−fiber collisions are negligible. We also explore the number density profiles of the reddest and the bluest satellites, finding a pronounced segregation of the former towards the central regions of the host halo. This closely resembles a similar effect found for satellites in the 3D analysis of the *Millennium Run* simulation, although we expect that real signal may have been strongly degraded due to projection effects. Both tests highlight the good performance of the proposed algorithm to avoid contamination by interlopers reconciling projected and three−dimensional results.

3.2 Introduction

Although the assignment of satellites to a host halo is a simple task in numerical simulations, it is far from straightforward in real data. In simulations we only need to

check whether the distance of the (candidate)−satellite to its (candidate)−host places it within or beyond the virial radius of the main halo. On the other hand, two serious obstacles are found in observations: i) we do not have information about the spatial extension of the host halo (namely its virial radius), and ii) we measure *projected* distances and velocities, an issue that sometimes can conspire to make objects look either closer or further from the host than they actually are. We propose a new method that builds on the first of these items, providing an estimation of the mass of the halo where an isolated galaxy settles that is only based on its observational properties. The cornerstone of the algorithm is the well−defined relation between color, luminosity and virial masses of galaxies we explored using the *Millennium Run* simulation and presented in the previous Chapter (see figure 1).

It is common in the literature to search for satellites within a circular region centered on each primary candidate using a fixed projected radius for all potential hosts (Zaritski et al. 1993, 1997; McKay et al. 2002; Brainerd & Specian 2003; Prada et al. 2003, Brainerd et al 2004a,b,2005; Sales & Lambas 2005; van den Bosch et al. 2005a,b, Agustsson & Brainerd 2006, Chen et al. 2006) As shown in figure 1, the virial mass of primary galaxies can vary significantly as a function of L, and then, a single Δ_R value would produce an under(over)−estimation of the virial radius in low (high) mass systems. The consequence of this is satellite samples highly contaminated by interlopers [1] for the low mass primaries, whereas for the high mass case satellite samples are likely to be incomplete. In this regard, an interesting and useful implementation of the M−L−color relation found for primary galaxies in the *Millennium* simulation is used here to improve satellite−search algorithms in observational catalogs. More precisely, by taking into account both, luminosity and color index of primaries, we are able to determine more accurately the primary galaxy mass, and therefore a more appropriate search radius in each host. We point out that the implementation of this method in an observational survey is straightforward and also computationally inexpensive compared to more rigorous alternative satellite identification algorithms (see for instance van den Bosch et al. 2004, Chen et al. 2006).

We describe in Section § 3.3 the projected data samples we use (Sloan and the mock catalog). We first apply our selection algorithm to the mock catalog and compare its performance to fixed Δ_r methods. In Section § 3.5 we identify satellites from the Sloan survey and study their spatial distribution around isolated hosts. We summarize our results in Section § 3.6.

3.3 2D Galaxy Data Samples: The Sloan Survey and the Mock Catalog Construction

Statistical studies of galaxy properties can now be made thanks to the availability of large photometric and redshift surveys. Among them, the most recent and ambitious projects are the *2−degree Field Galaxy Redshift Sample* [2] (2dFGRS, Colless et al. 2003) and the *Sloan Sky Digital Survey* [3] (York et al. 2000, Strauss et al. 2002). We use the

1 not physically bound pair of galaxies
2 http://www.mso.anu.edu.au/2dFGRS/
3 http://cas.sdss.org/dr4/en/

data release 4 (DR4, Adelman–McCarty et al. 2005) to select and analyze a sample of hosts and their satellite galaxies as a practical example on the implementation of our algorithm. In its spectroscopic version, the SDSS DR4 covers an area of 4784 deg^2 on the sky and provides positions, Petrosian magnitudes *u,g,r,i,z*, concentrations, spectral indices and accurate redshifts (average error $\sim$ 30 km/s) for approximately 480000 galaxies. The spectroscopic targets are objects brighter than $m_r = 17.77$, have r–band half light surface brightness $\mu_{50} \leqslant 24.5$ mag $arcsec^2$ and the redshifts of these peak at around $z \sim 0.1$.

According to this, we construct a 2D mock catalog from the 3D information of the *Millennium Run* simulation described in the previous Chapter, aimed to reproduce the DR4 main characteristics. The procedure involves projecting the data from the simulated box in a random direction assigning to each object a pair of spherical angular coordinates analogous of the (α, δ) (equatorial) or (l, b) (galactic) used for real objects on the sky. The area of coverage has been fixed to 4783 deg^2 according to the DR4 spectroscopic sample. Line–of–sight velocities depends on both the velocity and the distance to the object and is computed as $V_{los} = V_r + V_H$, where V_r is the projection of the real velocity into the line of sight and $V_H = rH_0$ is the Hubble flow at the 3D distance r. Redshifts are then obtained from $z = V_{los}/c$ with c the speed of light[4]. Apparent magnitude assignment needs some extra caution since the semi–analytical code has evolved all galaxies up to $z = 0$ whereas now they span a non–zero volume in redshift space. We therefore apply K–correction and evolution to the absolute magnitudes in order to refer galaxies to their position in the mock z–space. The final apparent magnitudes in the x–band ($x = u, g, r, i, z$, the 5 Petrosian magnitude bands provided by Sloan data) are then computed as: $m_x = M_x + DM(z) - K_x(z) - 5log(h) - e$, where M_x is the absolute x–band magnitude, $DM(z)$ is the distance modulus, $e = 1.6(z)$ is the correction for evolution (we apply the same correction to all bands) and we use the algorithm correct.v4 1 4 (Blanton et al. 2003) to estimate the K–corrections K_x in each magnitude–band. As a final step, we select the catalog of galaxies by applying the r–band magnitude cut used in the DR4: $m_r < 17.77$ that assures completeness in observation up to $\sim$ 90% level.

3.4 Description of the new satellite finding algorithm

3.4.1 *Algorithm scheme*

We outline a method to select satellites in observational samples aimed at reducing the fraction of interloper contamination included by previously used algorithms. We make use of the relation between the color, luminosities and masses of isolated hosts explored in Chapter 2 (see figure 1). Based on a simple tabulation of this relation, we assign virial masses to possible host halo candidates. From the virial mass of a given system we can directly infer its virial radius by $r_{200}^3 = M_{200}/(4/3\pi)\Delta\rho_c$, where Δ is the mean overdensity of mass enclosed within the virial radius expressed in

4 We adopt $H_0 = 73$ km/s Mpc^{-1} and $c = 3$ x10^5 km/s throughout this Chapter

units of the critical density of the universe[5]. It is clear that an estimation of M_{200} for isolated galaxies can therefore be translated into the (projected) area we need to identify satellites around these isolated hosts.

3.4.2 *Quick recipe for satellite finding*

The selection of host and satellite galaxies involves the following steps:

- *Identification of bright isolated galaxies.* This is required in order to maximize the chance of primary galaxies assigned as central objects in a given dark mater host halo. This means we look for galaxies whose gravitational potential dominates the local dynamics and we consequently avoid bright galaxies that are members themselves of a larger system like a galaxy group or cluster. For the present work we will consider as isolated all galaxies brighter than $M_r = -19.5$ (r−band absolute magnitude) and whose neighbors within a projected distance of 1Mpc and velocity difference smaller than 700 km/s are at least two (r−band) magnitudes fainter than the targeted isolated candidate. We refer to this sample as *ISO*.

- *Search for satellites around isolated primaries with a* **fixed** *radius and velocity criteria.* This step, although not strictly required, considerably improves the estimations of M_{200} achieved for host galaxies. As highlighted in Chapter 2, isolated galaxies without satellites tend to reside in lower mass dark matter halos when compared to galaxies of similar luminosity and color that do have associated satellites. Since the algorithm is optimized for the latter case, this auxiliary step enables a a rough characterization of the host population, getting rid of the largest fraction of isolated primaries from sample *ISO*. Based on the color distribution of these tentative host galaxies (sample *HSTFIX*) we select the color cuts that (inspired by the analysis performed on the 3D data) define the 5% bluest and the 35% reddst host sequences. Notice by chosing $\Delta_R = 500$ kpc and $\Delta_V = 500$ km/s we will generate as a sub product also a sample of satellites (*SATFIX*) composed by all galaxies within a projected (fixed) distance of 500 kpc and with velocity differences lower than 500 km/s from any isolated galaxy in sample *ISO*. We will use these satellites to establish further comparisons with the counterparts identified once the full adaptive method is applied.

- *Derivation of* Δ_R *and* Δ_V*.* Once the sequences in the M−L−color space are defined, we assign a virial mass M_{200} to each isolated primary in sample *ISO* establishing for each one an adaptive searching radius $\Delta_R = r_{200}$ and a maximum velocity for candidate satellites $\Delta V = V_{esc}(R_p)$, where $V_{esc}(R)$ is the local escape velocity at $r = R_p$ for an NFW halo of mass M_{200}.

- *Search for satellites around isolated primaries with* **adaptive** *radius and velocity criteria.* In the last step we look for satellite galaxies associated to galaxies in sample *ISO*

5 we use here $\Delta = 200$ following the convention adopted in the previous chapter; therefore $M_{vir} = M_{200}$ and $r_{vir} = r_{200}$ for sake of simplicity

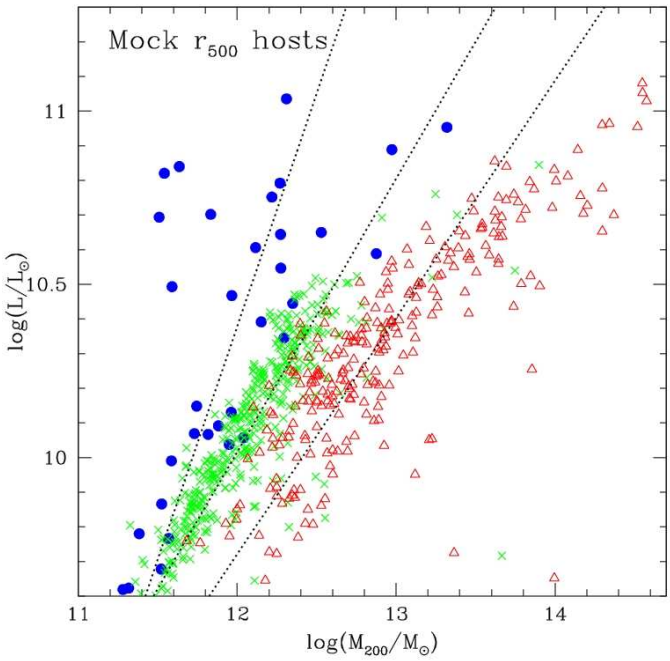

Figure 16. Mass−Luminosity relation of host galaxies in the *HSTFIX* sample. Solid points, crosses and triangles indicate the blue, intermediate and red color subsamples defined to estimate r_{200}.

defined to be at least $\Delta_m = 2$ (r−band) magnitudes fainter than the candidate host, within a projected distance $R \leqslant \Delta_R$ and with a relative line−of−sight velocity difference between them lower than Δ_V. These are the final samples of hosts and satellite galaxies and will be referred as *HSTADP* and *SATADP* respectively.

We notice that the adaptively definition of Δ_R and of Δ_V both introduce changes in the *SATFIX* sample building the *SATADP* sample. However, a quick analysis shows that the largest suppression of interlopers are introduced by restringing the satellite projected distances and not by their relative velocities. As discussed in van den Bosch et al. 2004 interlopers do not have a homogeneous distribution of velocities, but instead they have preferentially low velocities. Therefore, applying cuts only to ΔV (and keeping fixed $\Delta_R = 500$ kpc) is not as effective as restricting the projected distance of satellites according to the virial radius of their hosts.

3.4.3 *Application to the mock & algorithm performance*

We start by testing our adaptive satellite finding method by applying it to the mock galaxy catalog constructed from the *Millennium* simulation as explained in Section 3.3. We identified ~ 67000 isolated galaxies out of which only about ~ 1% (696) have at

COLOR SUBSAMPLE	A	B	σ
Blue	0.74 ± 0.16	4.28 ± 1.64	$0.07\log(L/L_\odot) - 0.64$
Intermediate	1.26 ± 0.04	-0.69 ± 0.41	$0.02\log(L/L_\odot) - 0.1$
Red	1.46 ± 0.07	-2.22 ± 0.68	$0.07\log(L/L_\odot) - 0.47$

Table 4. Coefficients for the assignment of virial masses to isolated galaxies: $\log(M_{200}/M_\odot h^{-1}) = a\log(L/L_\odot) + b$. Last column lists the dispersion introduced to this mean relation computed as a function of the luminosity.

SAMPLE	NAME	MOCK	DR4
isolated glxs	*ISO*	67643	59909
hosts Δ_r fix	*HSTFIX*	696	955
sats Δ_r fix	*SATFIX*	997	1199
hosts Δ_r adap	*HSTADP*	448	638
sats Δ_r adap	*SATADP*	723	865

Table 5. Number of galaxies in each subsample for the Mock catalog and the DR4 survey.

least 1 satellite when applied the fixed Δ_r and Δ_V criteria for satellite finding (see table 5). From the color distribution of these *HSTFIX* galaxies we derive $(g-r) = 0.35, 0.83$ as the limiting color indices that divide blue, intermediate and red host galaxies. The Mass−Luminosity relation of each color subsample defines a sequence in the M−L plane as shown in figure 16, that can be roughly reproduced by a linear relation of the form: $\log(M_{200}) = A\log(L) + B$ plus a Gaussian function that regulates the dispersion of the points around this mean trend. Table 4 summarizes the A and B coefficients found in each color subsample together with the expression used to reproduce the dispersion σ of points as a function of luminosity (we use the 3D sample in σ estimating in order to mitigate the noise introduced by the low number statistics in the projected host sample). We allocate M_{200} for each isolated galaxy in sample *ISO* by means of a and b coefficients according to the galaxy color index and generate a dispersion from this mean value using a Gaussian distribution with $\sigma(L/L_\odot)$. We finally proceed to the last step by searching for satellite galaxies with projected distances $R_p \leqslant \Delta_R = r_{200}$ and limiting their relative velocities to be lower than the local escape velocity of the host halo[6]. This gives us the *HSTADP* and *SATADP* samples of host and satellite galaxies that contains 448 and 723 objects each (see table5).

The performance of this satellite finding method can be evaluated by inspection

6 NFW concentrations here have been estimated for each primary using $\log(c) = 1.97 - 0.77\log(M_{200}/(M_\odot h^{-1}))$ and $\sigma(\log(c)) = 0.149$ as explained in Chapter 2

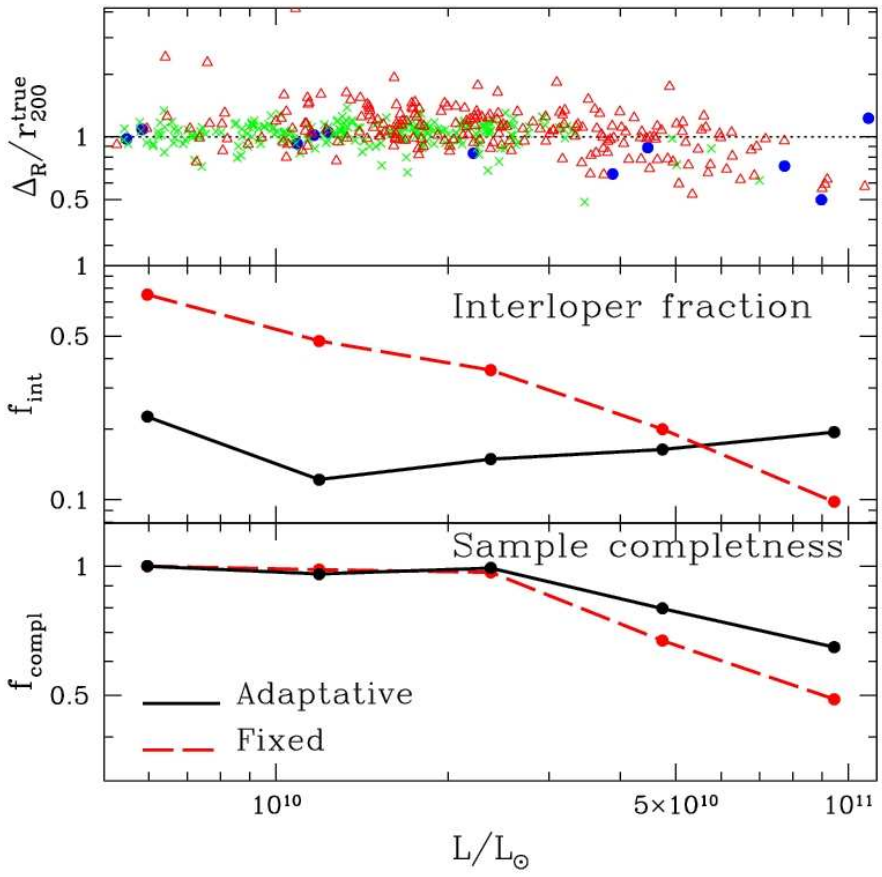

Figure 17. *Upper:* true vs estimated virial radius of host galaxies in the *HSTFIX* sample. The latter is derived using $\log(M_{200}) = A\log(L) + B$ with A and B tabulated according to galaxy color and listed in table 4. *Middle:* Interloper fraction in bins of host luminosities computed for galaxies in the *HSTFIX* (magenta dashed lines) and *HSTADP* (black solid curve) samples. *Bottom:* completeness of the satellite samples found selecting with the fixed (magenta dashed) and the adaptive (black solid) searching radius criteria.

of figure 17. In the upper panel we compare the true vs estimated values of r_{200} inferred for hosts in the *HSTADP* sample using the M−L relations tabulated before. Points lie mostly clustered around ~ 1, suggesting that the estimations of galaxy masses from their luminosity and colors are quite reliable. However, the relation also shows a non−negligible scatter with some galaxies (less than 1%) having their radius over or sub estimated by a factor of ~ 2. These outliers are largely dominated by hosts assigned to the red sequence for which the spread on the M−L plane is poorly constrained compared to the blue or intermediate color companions. Besides those cases where we naturally expect a considerable scatter, the large bulk of galaxies (80%) have a guessing for their r_{200} with an accuracy better than 25%.

The systematic underestimation of r_{200} for galaxies more luminous than $\log(L/L_\odot) > 10.7$ inherits the weaker dependence of the dark matter mass on the luminosity of the host when we move towards the high mass end of the halo mass function. As discussed in Chapter 2, this is only a reflection of the increasing contribution of satellites to the total luminosity of the galaxy system that produce the break around $\log(L/L_\odot) \sim 10.8$ in the σ−L relation shown in figure 1 of previous Chapter. We do not find this effect to be highly relevant in our samples since massive halos are likely to be populated by more than one bright galaxy not fulfilling our isolation criteria; actually, a very low percentage (lower than $\sim 1\%$) of the host primaries have luminosities exceeding $10^{10.7} L_\odot$ ($M_r < -22.3$).

Middle and bottom panels of figure 17 show the good performance of our new satellite identification method. We find that by selecting satellites in this way we sharply reduce the contamination due to interlopers to less than 20% of the sample regardeless the host luminosity[7]. This is among the lowest levels of contaminations reached by previous identification methods in the literature (see for instance van den Bosch et al. 2004). The largest improvement is for the faintest host galaxies, where a fixed search radius results in around 80% of interlopers. For these hosts, we now estimate a factor 4 reduction in spurious satellites. As we consider higher luminosity hosts the number of interlopers picked up by either the fixed and adaptive Δ_r methods match each other. However, also for these galaxies varying Δ_r with luminosity and colors of primaries translates into benefits since the completeness of the sample increases $\sim 50\%$ by allowing distant satellites with $R_p > 500$ kpc to enter the sample.

3.5 Application to the SDSS & the radial distribution of satellite galaxies

In this last Section we applied the adaptive criteria to search for satellites around isolated hosts in the SDSS DR4 data (York et al. 2000, Strauss et al 2002, Adelman−McCarty et al. 2005). We use this sample to compare the number density profile expected in projection and its relation to the three−dimensional distribution of satellites analyzed in Chapter 2.

We follow the procedure outlined in Section 3.4.2 using all galaxies from the Sloan catalog up to redshift $z = 0.1$. The A and B coefficients were taken from table 5 to

7 Here we consider as an interloper to all galaxy identified as a satellite in projection but with a three−dimensional distance to the host larger than the real virial radius of the main halo

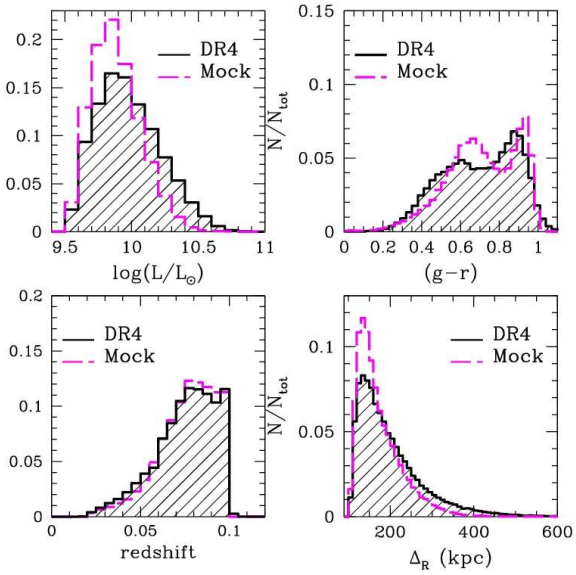

Figure 18. Comparison of magnitude, color, redshifts and estimated virial radius for isolated galaxies (*ISOADP*) in the mock catalog (magenta dashed line) and the DR4 (black solid−shaded histogram) sample.

assign virial masses to the ~ 59000 isolated primaries identified. Figure 18 compares the main properties of these galaxies to their counterparts selected from the mock catalog described in Section 3.4. Luminosities, colors and redshifts distributions seem to be in reasonable agreement in both samples although there is a tendency of galaxies in the Sloan sample to be shifted towards higher luminosities. This translates into r_{200} estimations shifted to slightly larger values than their distribution obtained from the mock galaxies. Color cuts applied to hosts in the Sloan survey are $(g-r) = 0.37, 0.81$ also consistent with those defined for the mock catalog. The final number of hosts and satellites in samples *HSTADP* and *SATADP* are 638 and 865 respectively and are listed in table 5. As found in the last Section using galaxies in the mock catalog, the fraction of isolated galaxies with positive identification of satellites is considerably low (less than ~ 1.1%). For most of them (78%) we detect only 1 satellite within their assigned r_{vir} and the fraction decreases for larger number of satellites per hosts; only about ~ 3% of galaxies in *HSTADP* sample host 4 or more satellites. The distribution of the number of satellites per hosts in shown in figure 19 and it is found to be in excellent agreement with the mock sample.

We use samples *HSTADP* and *SATADP* selected from the mock and DR4 survey to characterize the radial distribution of satellite galaxies around their hosts. The preliminary analysis carried out on the 3D data from the *Millennium Run* simulation in Chapter 2 suggests that satellites are good tracers of the dark matter distribution of host halos if we restrict to look at distances beyond $r \geqslant 0.2 r_{vir}$. This is in agreement with other previous works based on numerical simulations that mainly deal with

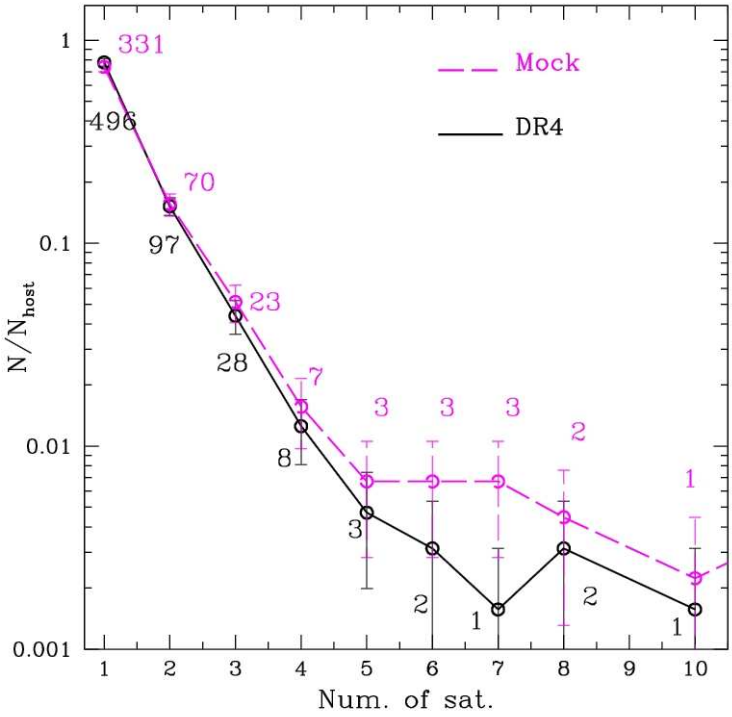

Figure 19. Number of satellites per hosts in the DR4 (black solid) and mock (magenta dashed curve) samples. Error bars indicate Poisson errors and numbers at each side of points the total (not normalized) number of hosts per bin.

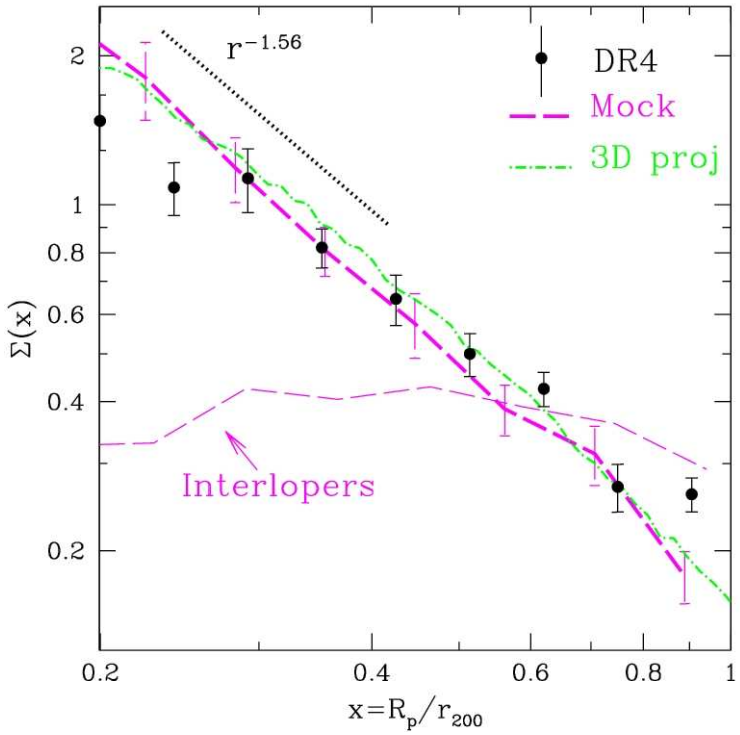

Figure 20. Projected number density distribution of satellites in the mock sample (thick magenta dashed line) compared to that obtained by projection of the 3D distribution of satellites analyzed in the previous Chapter (green dot−dashed line). Both curves are consistent with a power−law $\Sigma(x) \propto x^{\alpha}$ of slope $\alpha \sim -1.5, -1.6$. We also superimpose the data from the Sloan sample, shown in black dots. There is a reasonable agreement for $R_p > 0.3r_{200}$. Error bars correspond to 100 bootstrap re−sampling of the data. The expected contribution of interlopers when selecting satellites with the fixed Δ_R criteria is also shown in thin magenta dashed line (see text for further details).

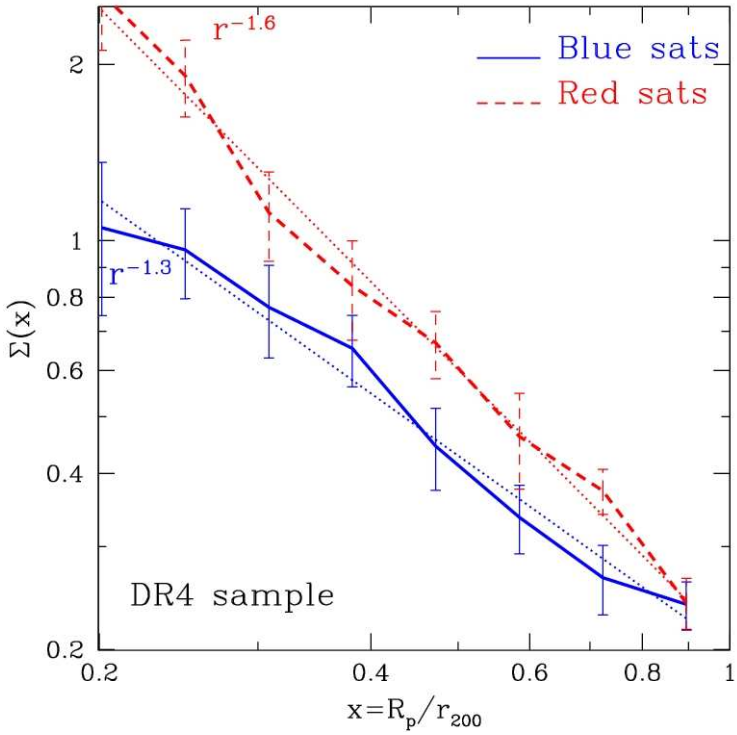

Figure 21. Red dashed and blue solid curves show the density profiles of the one−third reddest and the one−third bluest satellites in the Sloan sample. Dotted lines indicate the best−fit power law slopes obtained: $\alpha_{\mathrm{red}} = -1.6 \pm 0.1$ and $\alpha_{\mathrm{blue}} = -1.2 \pm 0.1$ for red and blue satellite samples respectively. This reflects the spatial segregation of satellites expected from the 3D analysis in the previous Chapter, although the signal has been erased by projection effects. The mock sample also shows comparable slopes: $\alpha_{\mathrm{red}} = -1.6 \pm 0.1$ and $\alpha_{\mathrm{blue}} = -1.3 \pm 0.1$.

dark matter subhalos and also galaxies associated to multiple systems like groups and clusters (Ghigna et al. 2002, Diemand et al. 2004, Nagai & Kravtsov 2005, Maccio et al. 2005, Weinberg et al. 2006). On the other hand, the *projected* radial distribution of satellite galaxies in observational samples is still far from being well constrained (e.g. van den Bosch et al. 2005, Sales et al. 2005, Chen et al. 2006). The main reason for discrepancies between independent studies may come from the way of accounting for interloper contamination. Therefore, our samples of satellite galaxies offer a suitable chance of disentangle this issue owing to the low fraction ($\leqslant$ 20%) of interloper contamination expected.

Figure 20 compares the (averaged) projected number density profile of satellites $\Sigma(x)$ in the mock catalog to the profile obtained from the projection of the 3D satellite sample analyzed in Chapter 2 (see figure 3). Σ is computed by counting the number of objects in circular annuli of projected distances $R_p > 0.2r_{200}$, dividing by the corresponding area and then normalizing to the total number of hosts in the sample. We notice that $0.2r_{200}$ translates onto $\sim$ 25 kpc in the lowest mass hosts, and then, the central regions of halos likely to hold the central primary galaxy are correctly avoided in the plot. Error bars were computed with 100 bootstrap re−sampling of the data. We find in Chapter 2 that satellites are distributed in the three−dimensional space following an NFW profile of concentration $c \sim 5.6$. We project randomly each of these systems considering only satellites within $r = r_{200}$, stack them (after rescaling distances to r_{200}) and take the average among all primaries. The resulting profile is close to a power law $\Sigma \propto x^{\alpha}$ with slope $\alpha = -1.56 \pm 0.02$ which is in good agreement with the value $\alpha = -1.5 \pm 0.1$ found for the mock sample. The likeness of both curves in figure 20 is a direct test of the ability of the satellite selection method to reflect in projected data the real three−dimensional distribution of satellites without biasing it with interloper contamination.

Interlopers are expected to flatten the distribution of real satellites, as shown by the thin dashed line in figure 20. This curve shows the projected profile of those objects identified as satellites by the fixed $\Delta_R - \Delta_V$ method, but that have been excluded from the sample *SATADP* when selecting with adaptive Δ_R and Δ_V. The effective removal of this subsample of objects allows proper match between the 2D distributions of satellites and the 3D space counterparts.

Figure 20 also shows the number density profile of satellites in the Sloan sample (black dots). We can see that this observational sample is also in agreement with both the mock and the 3D−projected data, although only at distances larger than $R_p > 0.3r_{200}$. For the inner regions, there is an artificial flattening of Σ that is likely due to the fiber−fiber collision not taken into account when constructing the mock catalog. In the SDSS sample, there is a restriction in the targeted objects since the fiber centers can not be placed closer than 55" on a given plate. This limitation produces the missing−pair problem, i.e. one of the pair components can not be observed. Strauss et al. 2002 quantified that about $\sim$ 6% of galaxies are lost to fiber−fiber collisions. At redshift $z \sim 0.6$, this restriction translate to $\sim$ 65 kpc, or equivalently to $0.32r_{200}$ for a typical $r_{200} = 200$ kpc in our host sample accounting for the apparent flattening of the number density profiles of satellites in the Sloan catalog. As this may be affecting our results, we excluded the two innermost points in figure 20 when estimating the slope

of the satellite distribution in this sample. We find $\alpha = -1.4 \pm 0.2$, a profile slightly shallower than (but consistent to) the distributions derived from the mock and the 3D projected data.

In a previous work, Chen et al 2006 derive $\alpha = -1.7 \pm 0.1$ for the projected radial distribution of satellites in the Sloan Survey. These authors compared several interloper rejection methods concluding that their *"nearby points"* procedure performs best. After the removal of the interloper contribution to the real profile, and based on empirical tests performed with numerical simulations, these authors apply an extra shift to α by adding $\Delta_\alpha = -0.1$. Our power law distribution for satellites in the Sloan catalog is in (marginal) agreement with Chen et al work. However, we notice the link between both results is not straightforward and must be considered with caution. Whereas Chen et al compute the best−fit α over physical radial units (kpc), we rescale each satellite to the estimated host r_{200} value. This may introduce significant changes to the derived shape because the host luminosity interval considered in Chen et al ($M_r = [-22, -20]$) span a wide range of masses (and therefore of r_{200}) in our method, and therefore, the inclusion of a normalization to each satellite could have non−negligible effects. Nevertheless and taken at face value, these results are encouraging since they show a reasonable agreement for the projected distribution of satellite galaxies that were both obtained by two independent methods.

Red satellite galaxies are shown to be more centrally clustered than blue ones in the three−dimensional analysis of Chapter 2. We analyzed the *projected* spatial segregation of satellites according to their colors with our 2D samples, as previously done for 3D data. Figure 21 shows the projected density profiles computed from the $1/3$ reddest (red short−dashed) and the $1/3$ bluest (solid lines) satellite fractions in the DR4 sample. Power laws fit to each curve are also quoted in these panels. We obtain $\alpha_{blue} = -1.2 \pm 0.1$ and $\alpha_{red} = -1.6 \pm 0.1$ for blue and red satellites respectively. The same analysis performed in the mock data shows $\alpha_{blue} = -1.3 \pm 0.1$ and $\alpha_{red} = -1.6 \pm 0.1$ in good agreement with the Sloan values. Profiles in both samples therefore predicts an over−abundance of red satellites of a factor ~ 1.5 at $R_p \sim 0.3 r_{200}$. This is comparably weaker than the difference in the spatial distribution of red and blue satellites found in the three−dimensional analysis, where the over−abundance of red satellites at $r = 0.3 r_{200}$ is a factor ~ 4 (see figure 4). This points out that some degree of segregation according to satellite colors is still conserved even in 2 dimensional data, although projection effects may induce a significant degradation of the signal.

We should not forget to mention the possible model−dependence of these results on the specific semi−analytical treatment applied to satellites. Galaxies that enter the virial radius of a larger system suffer significant modifications to their intrinsic properties like stellar and dark matter mass contents, colors, concentrations, etc, mainly due to a combination of the dynamical friction, tidal forces, strangulation and ram pressure stripping. All these effects are accounted for in different ways in each semi−analytical model, although it is most of the time only a crude attempt to mimic the real physics (still not well−known) that operates in such scales and dynamics. In the particular case of the Croton et al. (2006) code it has been found that satellite galaxies tend to be redder than satellites in comparable systems of real catalogs. However, although the relative fraction of red and blue satellites in our samples might

therefore be affected by this, we indeed compare the 3D data to the mock catalog generated under the same semi−analytical prescriptions. This is then a fair comparison that get rid of the dependence in the satellite modelling and suggests that the smaller segregation we found between blue and red satellites in 2D data (compared to that present in the 3D space) is a real effect caused only by the information lost when projecting the positions and velocities of satellites. This reinforces the idea that the differences in the radial distribution of blue and red satellites might be stronger in the three−dimensional space than that found here in projection for the SDSS data.

3.6 Conclusions from this Chapter

In this Chapter we have developed a new method for the identification of satellite galaxies in observational catalogs that adaptively defines a search area to look for candidate satellites that depends upon the expected mass for the host halo. We use the Mass−Luminosity relations found in the previous Chapter taking also into account the color indices of galaxies. Using a mock galaxy catalog we constructed from the *Millennium Run* simulation, we calibrate a relation of the form: $\log(M_{200}/M_{\odot}) = A\log(L/L_{\odot}) + B$, where A and B vary for blue, intermediate or red color hosts. We finally apply the algorithm to identify satellite galaxies in the SDSS DR4 catalog and analyze their projected radial distribution around isolated hosts. Our main results can be summarized as follows:

- We can recover virial radii of hosts based on their color and luminosities to an accuracy better than 25% for the large (80%) majority of isolated primary galaxies.
- The inclusion of interlopers in the sample is limited to less than $\sim 20\%$ regardless of the host luminosity. This is among the lowest levels of contamination reached by previous identification methods in the literature. Also the completeness level performs better by up to 30% for the brightest hosts although for these galaxies the inclusion of interlopers is higher than in the fixed Δ_R method. This is a consequence of the larger search area for satellites, which allows the inclusion of a higher fraction of spurious pairs. Nevertheless, the number of isolated primary galaxies in the last luminosity bin is small ($\sim 6\%$) so we do not expect our results to be strongly affected by them.
- We study the projected radial distribution of satellites in the mock and the Sloan catalogs. We fit power law relations to these profiles ($\Sigma(R_p) \propto R_p^{\alpha}$) finding $\alpha = -1.5 \pm 0.1$ for the mock sample. This is in agreement with the projection of the NFW distribution of satellite galaxies found previously in the three−dimensional analysis of Chapter 2. In the case of the Sloan sample, the slope is slightly shallower ($\alpha = -1.4 \pm 0.2$) although consistent with those derived from the *Millennium* data (3D and mock).
- Satellites in the Sloan sample show a spatial segregation that depends on their colors: red satellites are preferentially found closer to the host than the blue counterparts. This is reflected on the slope of their number density profiles:

$\alpha_{blue} = -1.2 \pm 0.1$ and $\alpha_{red} = -1.6 \pm 0.1$ for the $1/3$ bluest and reddest satellite fractions respectively. This is in agreement with our analysis of the radial distribution of red and blue satellites in three−dimensions performed in Chapter 2. Nevertheless we find the signal present in the latter to be significantly reduced due to projection effects in observational samples.

The semi−analytical modelling of galaxies has been shown to be able to reproduce several global properties of real galaxies, distribution of colors, magnitudes, clustering, etc. Nevertheless, the detailed analysis of galaxies in all scales is indispensable to fully support a particular and specific modelling. The comparison between observations and simulations demands suitable methods to select comparable samples from both sources. We propose an identification algorithm of satellites based on the color and luminosities of their host primaries aimed to reduce the inclusion of interlopers in observational catalogs. A successful implementation of this or other similar−aimed methods to improve the agreement between real and simulated data will provide the fundamental proofs about how well our theoretical models provide a reliable understanding of galaxy formation.

Part II

DYNAMICAL EVOLUTION OF SATELLITE GALAXIES IN NUMERICAL SIMULATIONS

4

SATELLITES OF SIMULATED GALAXIES: SURVIVAL, MERGING, AND THEIR RELATION TO THE DARK AND STELLAR HALOS

4.1 Abstract

We study the population of satellite galaxies formed in a suite of N−body/gasdynamical simulations of galaxy formation in a ΛCDM universe. The simulations resolve the ~ 10 most luminous satellites around each host, and probe systems up to six or seven magnitudes fainter than the primary. We find little spatial or kinematic bias between the dark matter and the satellite population. The radius containing half of all satellites is comparable to the half−mass radius of the dark matter component, and the velocity dispersion of the satellites is a good indicator of the virial velocity of the halo; $\sigma_{sat}/V_{vir} \sim 0.9 \pm 0.2$. Applied to the Local Group, this result suggests that the virial velocity of M31 and the Milky Way might be substantially lower than the rotation speed of their disk components; we find $V_{vir}^{MW} \sim 109 \pm 22$ km/s and $V_{vir}^{M31} \sim 138 \pm 35$ km/s, respectively, compared with $V_{rot}^{MW} \sim 220$ km/s and $V_{rot}^{M31} \sim 260$ km/s. Although the uncertainties are large, it is intriguing that both estimates are significantly lower than expected from recent semianalytic models, which predict only a small difference between V_{vir} and V_{rot}. The detailed kinematics of simulated satellites and dark matter are also in good agreement: both components show a steadily decreasing velocity dispersion profile and a mild radial anisotropy in their velocity distribution. By contrast, the stellar halo of the simulated galaxies, which consists predominantly of stellar debris from *disrupted* satellites, is kinematically and spatially distinct from the population of *surviving* satellites. This is because the survival of a satellite as a self−bound entity depends sensitively on mass and on time of accretion; surviving satellites are significantly biased toward low−mass systems that have been recently accreted by the galaxy. Our results support recent proposals for the origin of the systematic differences between stars in the Galactic halo and in Galactic satellites: the elusive "building blocks" of the Milky Way stellar halo were on average more massive, and were accreted (and disrupted) earlier than the population of dwarfs that has survived self−bound until the present.

4.2 Introduction

The satellite companions of bright galaxies are exceptionally useful probes of the process of galaxy formation. Studies of the dynamics of satellites around bright galaxies, for example, have provided incontrovertible evidence for the ubiquitous presence of massive dark halos surrounding luminous galaxies, a cornerstone of the present galaxy formation paradigm.

Satellites may also be thought of as probes of the faint end of the luminosity function. After all, satellite galaxies are, by definition, dwarf systems, thought to be themselves surrounded by their own low−mass dark matter halos. These low−mass halos are expected to be the sites where the astrophysical processes that regulate galaxy formation (i.e., feedback) operate at maximum efficiency. Thus, the internal structure, star formation history, and chemical enrichment of satellites provide important constraints on the process of galaxy formation in systems where theoretical models predict a highly non−trivial relation between dark mass and luminosity (see, e.g., White & Rees 1978; Kauffmann et al. 1993; Cole et al. 1994; see as well Cole et al. 2000 and Benson et al. 2002).

The anticipated highly non−linear mapping between dark matter and light at the faint−end of the luminosity function is perhaps best appreciated in the satellite population of the Local Group, where the relatively few known satellites stand in contrast with the *hundreds* of "substructure" cold dark matter (CDM) halos of comparable mass found in cosmological N−body simulations (Klypin et al. 1999; Moore et al. 1999). One possible resolution to this "satellite crisis" invokes the energetic feedback from stars plus the effects of reionization to reduce the star formation activity in substructure halos. (see, e.g. Kauffmann et al. 1993; Bullock et al. 2000; Somerville et al. 2001; Benson et al. 2002)

The price paid for reconciling cold dark matter substructure with the Local Group satellite population is one of simplicity, as the "feedback" processes invoked involve complex astrophysics that is not yet well understood nor constrained. It is not yet clear, for example, whether the brighter satellites inhabit the more massive substructures, or whether, in fact, there is even a monotonic relation between light and mass amongst satellites. This issue is further complicated by the possibility that a substantial fraction of a satellite's mass may have been lost to tides. Tidal stripping is expected to affect stars and dark matter differently, complicating further the detailed relation between light and mass in substructure halos (Hayashi et al. 2003; Kravtsov et al. 2004, Strigari et al. 2007a,b).

These uncertainties hinder as well the interpretation of satellites as relicts of the hierarchical galaxy assembly process, and consensus has yet to emerge regarding the severity of the biases that the various effects mentioned above may engender. Do the spatial distribution of satellites follow the dark matter? Is the kinematics of the satellite population substantially biased relative to the dark matter's? Have satellites lost a substantial fraction of their stars/dark matter to stripping? Are surviving satellites fair tracers of the population of accreted dwarfs?

Of particular interest is whether satellites may be considered relicts of the "building blocks" that coalesced to form the early Galaxy. Indeed, the stellar halo of the Milky

Way is regarded, in hierarchical models, to consist of the overlap of the debris of many accreted satellites which have now merged and mixed to form a kinematically hot, monolithic stellar spheroid (Searle & Zinn 1978; Bullock & Johnston 2005; Abadi et al. 2006; Moore et al. 2006). A challenge to this view comes from detailed observation of stellar abundance patterns in satellite galaxies in the vicinity of the Milky Way. At given metallicity, the stellar halo (at least as sampled by stars in the solar neighbourhood) is systematically more enriched in $\alpha-$elements than stars in Galactic satellites (Fuhrmann 1998; Shetrone et al. 2001, 2003; Venn et al. 2004) , a result that remains true even when attempting to match stars of various ages or metallicities (Unavane et al. 1996; Gilmore & Wyse 1998; Pritzl et al. 2005). Can hierarchical models explain why satellites identified today around the Milky Way differ from the ones that fused to form the Galactic halo?

Preliminary clues to these questions have been provided by the semianalytic approach of Bullock, Johnston and collaborators (Bullock & Johnston 2005; Font et al. 2006a,b) , who argue that hierarchical models predict naturally well−defined distinctions between the halo and satellite stellar populations. Detailed answers, however, depend critically on which and when substructure halos are "lit up" and how they evolve within "live" dark matter halos. These are perhaps best addressed with direct numerical simulation that incorporates the proper cosmological context of accretion as well as the gasdynamical effects of cooling and star formation in an evolving population of dark matter halos. The study we present in this Chapter aims to address these issues by analyzing the properties of the satellite population of L_* galaxies simulated in the ΛCDM scenario. We introduce briefly the simulations in § 4.3, analyze and discuss them in § 5.3 and we conclude with a summary of the main results § 5.5.

4.3 The Numerical Simulations

Our suite of eight simulations of the formation of L_* galaxies in the ΛCDM scenario is the same discussed recently by Abadi, Navarro and Steinmetz (2006). The simulations are similar to the one originally presented by Steinmetz & Navarro (2002), and have been analyzed in detail in several recent papers, which the interested reader may wish to consult for details on the numerical setup (Abadi et al. 2003a,b; Meza et al. 2003, 2005; Navarro et al. 2004).

Briefly, each simulation follows the evolution of a small region of the universe chosen so as to encompass the mass of an L_* galaxy system. This region is chosen from a large periodic box and resimulated at higher resolution preserving the tidal fields from the whole box. The simulation includes the gravitational effects of dark matter, gas and stars, and follows the hydrodynamical evolution of the gaseous component using the Smooth Particle Hydrodynamics (SPH) technique (Steinmetz 1996). We adopt the following cosmological parameters for the ΛCDM scenario: $H_0 = 65$ km/s/Mpc, $\sigma_8 = 0.9$, $\Omega_\Lambda = 0.7$, $\Omega_{\rm CDM} = 0.255$, $\Omega_{\rm bar} = 0.045$, with no tilt in the primordial power spectrum.

All simulations start at redshift $z_{\rm init} = 50$, have force resolution of order 1 kpc, and the mass resolution is chosen so that each galaxy is represented on average, at $z = 0$, with $\sim 50,000$ gas/dark matter particles and $\sim 125,000$ star particles. Each

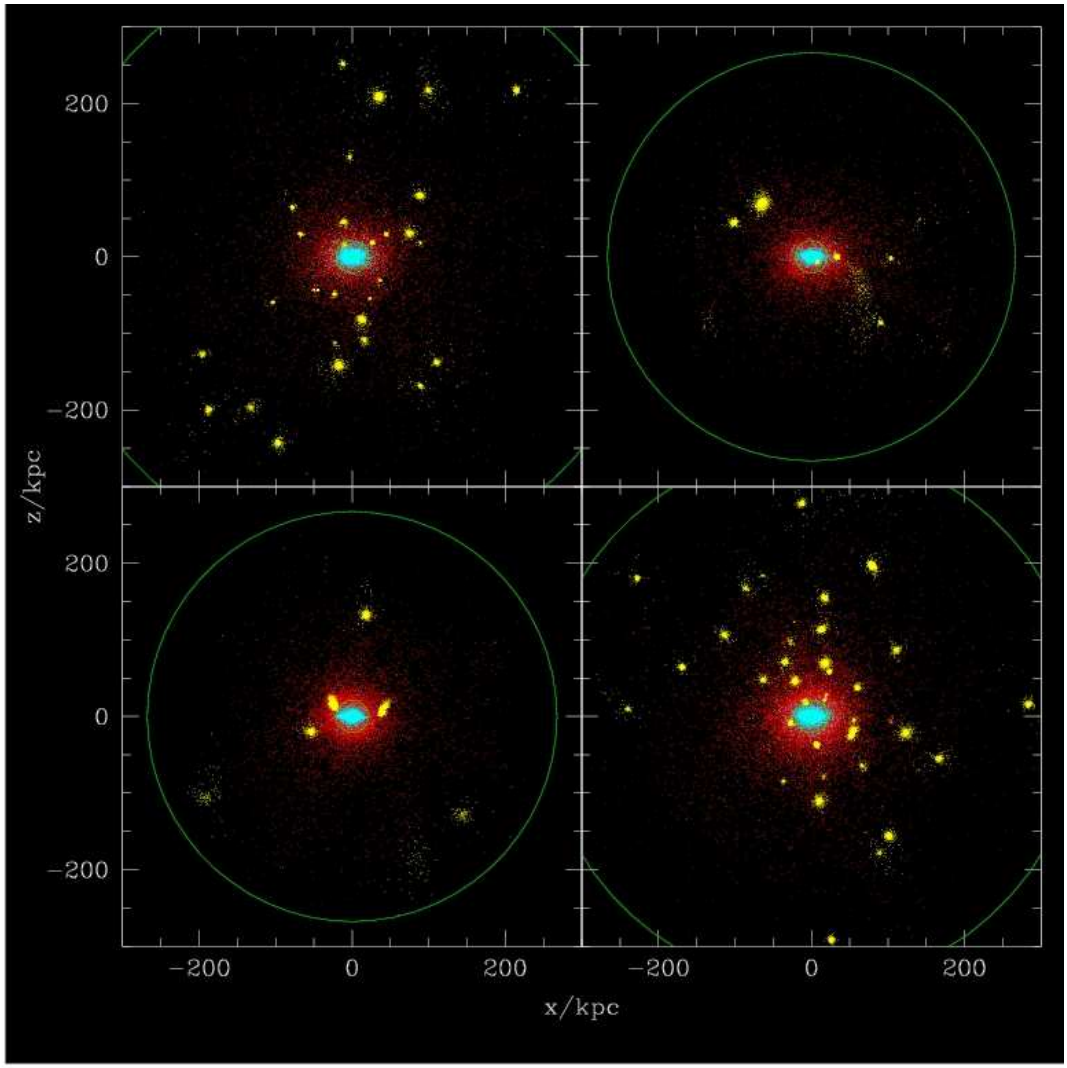

Figure 22. Spatial distribution of the stellar component of four of our simulated galaxies at z=0. Each panel corresponds to a different simulation, projected so that the inner galaxy is seen approximately "edge−on". The virial radius of the system is marked by the outer green circle in each panel. The inner circle has a radius of 20 kpc, where most the stars in each galaxy are found. Stars that have formed in satellites that survive as self−bound entities until $z = 0$ are shown in yellow. "In situ" stars, i.e., those formed in the most massive progenitor of the galaxy, are shown in cyan, whereas those formed in satellites that have been accreted and disrupted by the main galaxy are shown in red. Note that the diffuse outer stellar halo reaches almost out to the virial radius, and consists almost exclusively of accreted stars. The inner galaxy, on the other hand, is dominated by stars formed "in situ".

re−simulation follows a single $\sim L_*$ galaxy in detail, and resolves a number of smaller, self−bound systems we shall call generically "satellites". We shall hereafter refer to the main galaxy indistinctly as "primary" or "host".

Gas is allowed to turn into stars at rates consistent with the empirical Schmidt−like law of Kennicutt (1998) in collapsed regions at the center of dark matter halos. Because star formation proceeds efficiently only in high−density regions, the stellar components of primary and satellites are strongly segregated spatially from the dark matter. We include the energetic feedback of evolving stars, although its implementation mainly as a heating term on the (dense) gas surrounding regions of active star formation implies that most of this energy is lost to radiation and that feedback is ineffective at curtailing star formation. The transformation of gas into stars thus tracks closely the rate at which gas cools and condenses at the center of dark matter halos. This results in an early onset of star−forming activity in the many progenitors of the galaxy that collapse at high redshift, as well as in many of the satellite systems we analyze here.

Another consequence of our inefficient feedback algorithm is that gas cooling and, therefore, star formation, proceed with similar efficiency in all well−resolved dark matter halos, irrespective of their mass. As a result, the total stellar mass of a satellite correlates quite well with the "original" mass of its progenitor dark halo; i.e., the total mass of the satellite before its accretion into the virial radius of its host. We define the *virial* radius, r_{vir}, of a system as the radius of a sphere of mean density $\Delta_{vir}(z)$ times the critical density for closure. This expression defines implicitly the virial mass, M_{vir}, as that enclosed within r_{vir}, and the virial velocity, V_{vir}, as the circular velocity measured at r_{vir}. Quantities characterizing a system will be measured within r_{vir}, unless otherwise specified. The virial density contrast, $\Delta_{vir}(z)$ is given by $\Delta_{vir}(z) = 18\pi^2 + 82f(z)\text{-}39f(z)^2$, where $f(z) = [\Omega_0(1+z)^3/(\Omega_0(1+z)^3 + \Omega_\Lambda))]\text{-}1$ and $\Omega_0 = \Omega_{CDM} + \Omega_{bar}$ (Bryan & Norman 1998). $\Delta_{vir} \sim 100$ at $z = 0$.

It is likely that improvements to our feedback algorithms may lead to revisions in the efficiency and timing of star formation in these galaxies, and especially in the satellites, but we think our results will nonethelesss apply provided that these revisions do not compromise the relatively simple relation between stellar mass and halo mass that underpins many of our results. For example, we expect that modifications of the star formation algorithm will affect principally the number, age, and chemical composition of stars, rather than the dynamical properties of the satellites. This is because the latter depend mainly on the mass, orbit, and timing of the merging progenitors, which are largely dictated by the assumed cosmological model. These properties are less sensitive to the complex astrophysics of star formation and feedback, and therefore our analysis focuses on the kinematics and dynamical evolution of the satellite population around the eight galaxies in our simulation suite.

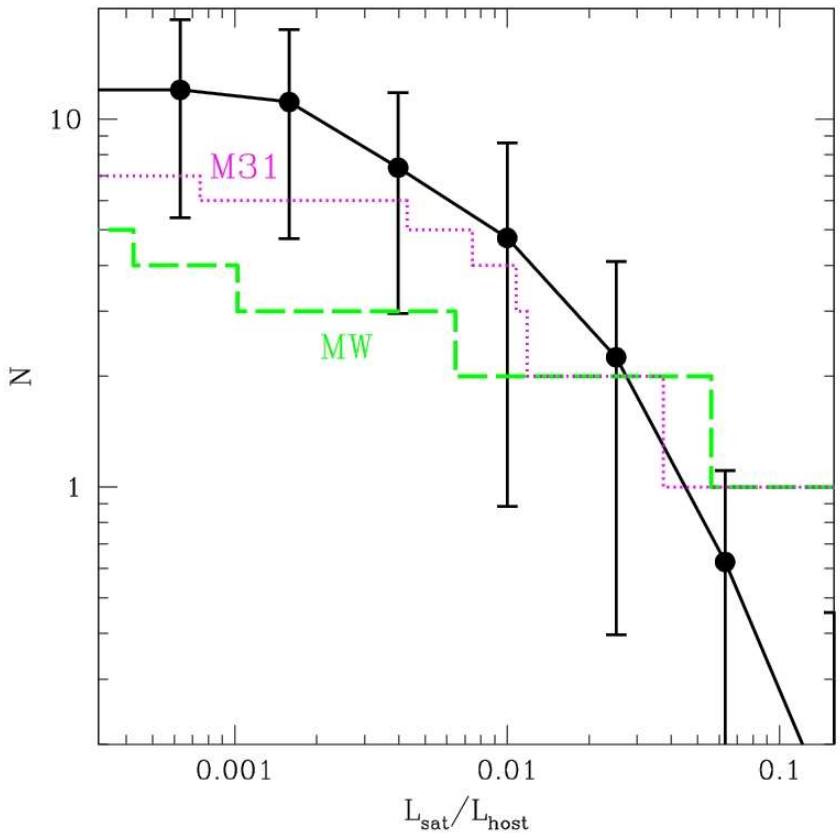

Figure 23. Cumulative luminosity distribution of simulated satellites (filled circles), averaged over our eight simulations, and compared with the Milky Way (blue dashed line) and M31 (red dotted curve) satellite systems. Satellite luminosities are scaled to the luminosity of the host. Error bars in the simulated data indicate Poisson uncertainties in the computation of the average. The flattening of the simulated satellite distribution below 0.1% of the primary luminosity is due to numerical limitations. The Local Group data are taken from van den Bergh (1999). For the MW and M31 systems we include only satellites at distances closer than 300 kpc from the central galaxy.

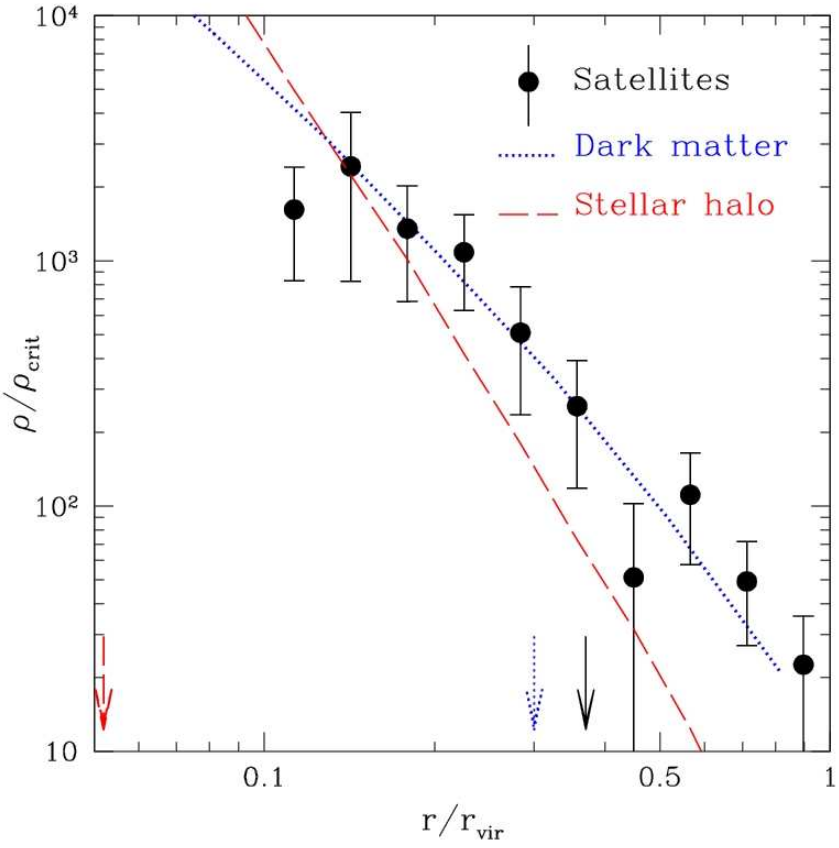

Figure 24. Number density profile of simulated satellites, after scaling their positions to the virial radius of each host and stacking all eight simulations (solid circles; error bars denote Poisson uncertainties associated with the total number of satellites in each radial bin). The dotted line corresponds to the average dark matter density profile, and the dashed line to the stars in the outer stellar halo. The vertical normalization for the satellite and stellar halo profiles has been chosen so that all profiles approximately coincide at $r \sim 0.15\, r_{vir}$. Note that the spatial distribution of satellites is similar to the dark matter, and that stars in the stellar halo are significantly more centrally concentrated. Arrows mark the radius containing half the objects in each component. See text for further discussion.

4.4 Results and Discussion

4.4.1 *Characterization of the satellite population*

Figure 22 shows the spatial distribution of all star particles in four of our simulated galaxies. Stars are assigned to one of three components and colored accordingly. Particles in cyan are "in−situ" stars; i.e., stars that formed in the main progenitor of the primary galaxy. Stars in red formed in satellites that have since been accreted and fully disrupted by the tidal field of the galaxy. Stars in yellow formed in systems that survive as recognizable self−bound satellites until $z = 0$. As discussed in detail by Abadi et al (2006), the tidal debris of fully disrupted satellites makes up the majority of the smooth outer stellar halo component. "In−situ" stars, on the other hand, dominate the inner galaxy, whereas surviving satellites are easily identifiable as overdense, tightly bound clumps of stars.

In practice, we identify satellite systems using a friends−of−friends algorithm to construct a list of potential stellar groupings, each of which is checked to make sure that (i) they are self−bound, and that (ii) they contain at least 35 star particles. This minimum number of stars (which corresponds roughly to $\sim 0.03\%$ of the stellar mass of the primary at $z = 0$) is enough to ensure the reliable identification of the satellite at various times and the robust measurement of their orbital properties, but is insufficient to study the internal structure of the satellite. The satellite identification procedure is run for all snapshots stored for our simulations, allowing us to track the evolution of individual satellites.

With these constraints, our simulations resolve, at $z = 0$, an average of about 10 satellites within the virial radius of each simulated galaxy. The cumulative luminosity distribution of these satellites (computed in the V band[1] for ease of comparison with data available for the Local Group satellites) is shown in Figure 23. The brightest satellite is, on average, about $\sim 12\%$ as bright as the primary, in reasonable agreement with the most luminous satellite around the Milky Way and M31: the LMC and M33 are, respectively, 11% and 8% as bright as the MW and M31 (van den Bergh 1999).

At brightnesses below 0.2% of L_{host} the number of simulated satellites levels off as a result of numerical limitations. Independent tests (Abadi et al, in preparation) show that this brightness limit corresponds to where satellite identification in the simulations becomes severely incomplete. We note that this limitation precludes us from addressing the "satellite crisis" alluded to in §1: our simulations lack the numerical resolution needed to resolve the hundreds of low−mass substructure halos found in higher−resolution CDM simulations. On average, the 10th brightest satellite in our simulations is ~ 5.6 mag fainter than the primary; for comparison, the MW and M31 have only 2 and 5 satellites as bright as that.

Given the small number of systems involved and the considerable scatter from simulation to simulation (the number of bright satellites ranges from 4 to 21 in our eight simulations) we conclude that there is no dramatic discrepancy between observations and simulations at the bright end of the satellite luminosity function. Applying

1 Luminosity estimates in various bands are made by convolving the masses and ages of star particles with standard spectrophotometric models, see, e.g., Abadi et al 2006 for details.

our results to the full Local Group satellite population, including, in particular, the extremely faint dwarfs being discovered by panoramic surveys of M31 and by the SDSS (Zucker et al. 2004, 2006; Willman et al. 2005; Martin et al. 2006; Belokurov et al. 2006, 2007; Irwin et al. 2007; Majewski et al. 2007), involves a fairly large extrapolation, and should be undertaken with caution (see, e.g., Peñarrubia, McConnachie & Navarro 2007 for a recent discussion).

4.4.2 *Spatial distribution*

Figure 22 shows that satellites are found throughout the virial radius of the host and that, unlike stars in the smooth stellar halo, satellites show little obvious preference for clustering in the vicinity of the central galaxy. This is confirmed in Figure 24, where the solid circles show the number density profile of satellites, after rescaling their positions to the virial radius of each host and stacking all eight simulations. The dashed and dotted lines in this figure correspond, respectively, to the density profile of the stellar and dark matter halos, scaled and stacked in a similar way. The vertical normalization of the satellite and stellar halo profiles is arbitrary, and has been chosen so that all profiles approximately match at $r \sim 0.15\, r_{vir}$.

There is little difference in the shape of the dark matter and satellite profiles: half of the satellites are contained within $\sim 0.37\, r_{vir}$, a radius similar to the half−mass radius of the dark matter, $\sim 0.3\, r_{vir}$. We conclude that, within the uncertainties, the satellites follow the dark matter. The stellar halo, on the other hand, is much more centrally concentrated than the dark matter and satellites; its half−mass radius is only $\sim 0.05\, r_{vir}$, as shown by the arrows in Figure 24.

This result implies that the spatial distribution of simulated satellites is distinct from that of CDM substructure halos, whose density profile is known to be significantly shallower than the dark matter's (Ghigna et al. 1998; 2000; Gao et al. 2004; Diemand et al. 2004). This suggests that the "mapping" between dark and luminous substructure is highly non−trivial, as argued by Springel et al. (2001) and De Lucia et al. (2004). Our results, which are based on direct numerical simulation, validate these argumnents and illustrate the complex relation between galaxies and the subhalos in which they may reside (see also Kravtsov et al. 2004; Nagai & Kravtsov 2005; Gnedin et al. 2006; Weinberg et al. 2006). Luminous satellites are resilient to disruption by tides, and they can survive as self−bound entities closer to the primary, where substructures in dark matter−only simulations may quickly disrupt, as first pointed out by White & Rees (1978).

We conclude that using dark matter substructures to trace directly the properties of luminous satellites is likely to incur substantial and subtle biases which may be difficult to avoid. Models that attempt to follow the evolution of dark matter substructures and their luminous components are likely to fare better (Croton et al. 2006; Bower et al. 2006), but definitive conclusions will probably need to wait until realistic simulations with enhanced numerical resolution and improved treatment of star formation become available.

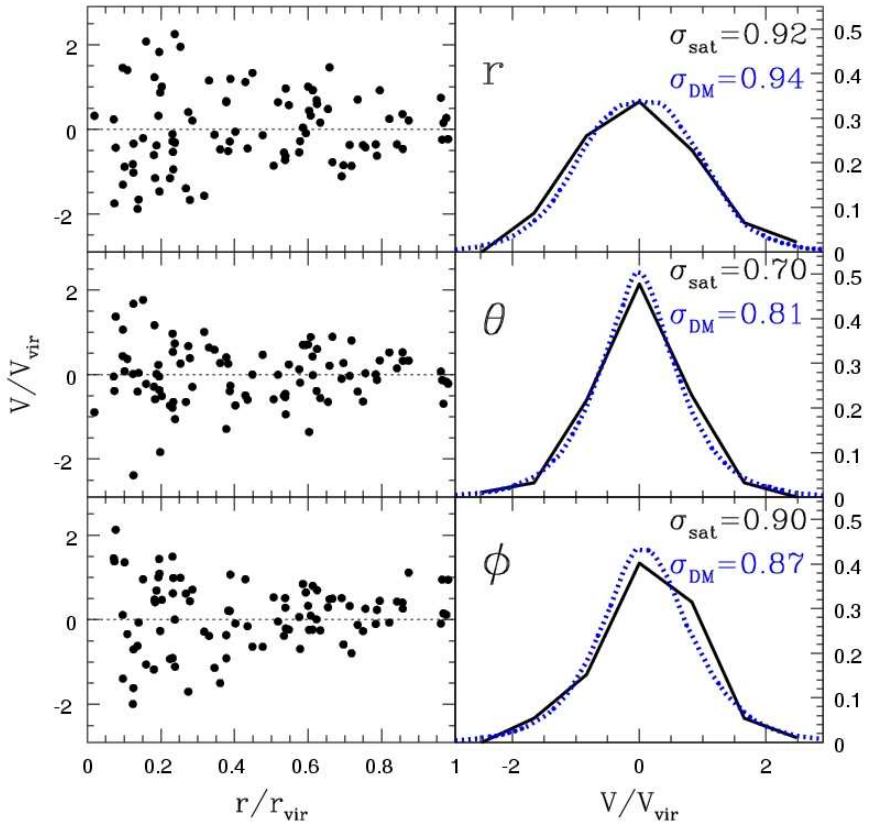

Figure 25. Spherical components of satellite velocities at $z = 0$ as a function of their distance to the center of the host galaxy. Each system has been rotated so that the angular momentum of the inner galaxy is aligned with the direction of the $z-$coordinate axis. Positions and velocities have been scaled to the virial radius and velocity of each host halo. Panels on the right show the velocity distributions of the satellite population within r_{vir} (solid lines) and compare it to the dark matter particles (dotted lines). The velocity dispersions are given in each panel. Note the slight asymmetry in the satellites' V_ϕ velocity distribution, which results from the net co−rotation of satellites around the primary.

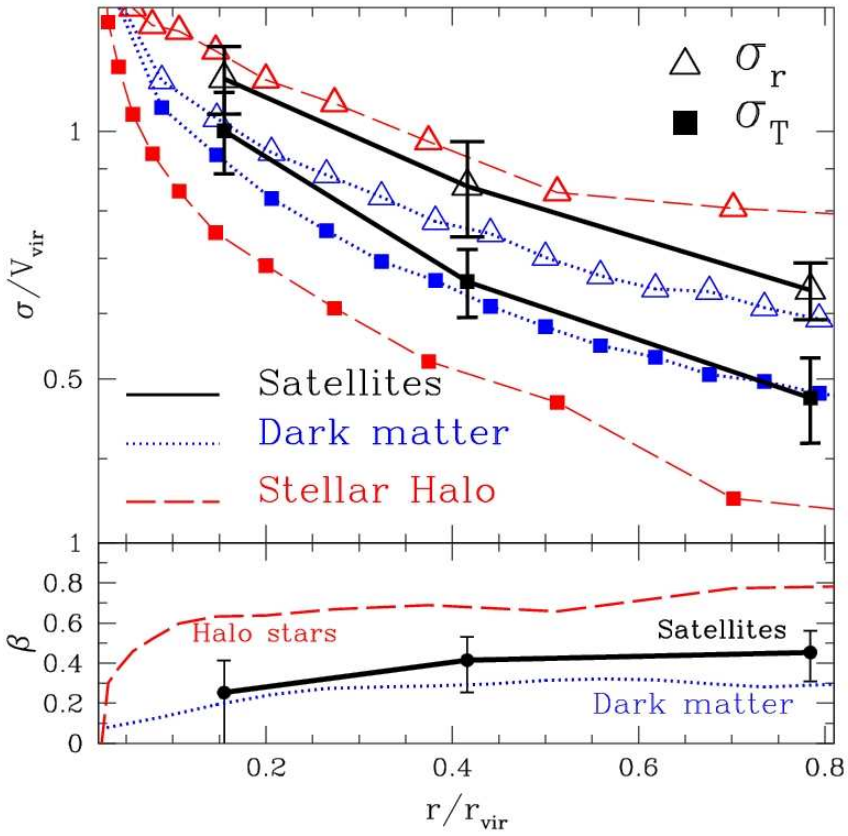

Figure 26. *Top panel:* Radial and tangential velocity dispersion profiles of satellites, dark matter, and stellar halo, computed after scaling to virial values and stacking all simulations in our series. *Bottom panel:* Anisotropy parameter as a function of radius for the satellite population, compared with dark matter particles and with the stellar halo. Note that satellites are only slightly more radially anisotropic than the dark matter and kinematically distinct from the stellar halo.

4.4.3 *Kinematics*

The likeness in the spatial distribution of satellites and dark matter anticipates a similar result for their kinematics. This is illustrated in Figure 25, where the panels on the left show the spherical components of the satellites' velocities (in the rest frame of the host and scaled to its virial velocity) versus galactocentric distance (in units of the virial radius of the host). Velocity components are computed after rotating each system so that the $z-$axis (the origin of the polar angle θ) coincides with the rotation axis of the inner galaxy. The corresponding velocity distributions are shown by the thick solid lines in the panels on the right, and compared with those corresponding to the dark matter particles (dotted lines).

The velocity distribution of each component is reasonably symmetric and may be well approximated by a Gaussian, except perhaps for the satellites' $V_\phi-$component, which is clearly asymmetric. This is a result of net rotation around the z axis: the satellite population has a tendency to co$-$rotate with the galaxy's inner body which is more pronounced than the dark matter's. Indeed, we find that on average the specific angular momentum of satellites is $\sim 50\%$ higher than the dark matter, and a factor of ~ 10 higher than the stellar halo. This result likely arises as a consequence of the accretion and survival biases discussed below; surviving satellites accrete late and from large turnaround radii, making them especially susceptible to the tidal torques responsible for spinning up the galaxy. The overall effect, however, is quite small, and rotation provides a negligible amount of centrifugal support to the satellite population.

The velocity dispersion of both satellites and dark matter particles drops steadily from the center outwards, as shown in Figure 26. The top panel shows that the drop is similar in all components, and that the velocity dispersion decrease from its central value by a factor of ~ 2 at the virial radius. This figure also shows that the velocity distribution is radially anisotropic, and that the anisotropy becomes more pronounced in the outer regions. The trends are again similar for satellites and dark matter, rising slowly with radius and reaching $\beta \sim 0.4$ at the virial radius. (The anisotropy parameter, β, is given by $\beta = 1 - ({\sigma_t}^2/2{\sigma_r}^2)$, where σ_r is the radial velocity dispersion and $\sigma_t = \sqrt{(\sigma_\phi^2 + \sigma_\theta^2)/2}$ is the tangential velocity dispersion.)

The stellar halo, on the other hand, is kinematically distinct from the satellites and from the dark matter. Overall, its velocity dispersion is lower, and its anisotropy is more pronounced, rising steeply from the center outwards and becoming extremely anisotropic ($\beta \sim 0.8$) in the outer regions. As discussed in detail by Abadi et al (2006), this reflects the origin of the stellar halo as debris from satellite disruption, which occur at small radii, where tidal forces are maximal. Stars lost during disruption (merging) events and that now populate the outer halo must therefore be on rather eccentric orbits, as witnessed by the prevalence of radial motions in Figure 26. The kinematical distinction between satellites and stellar halo thus suggests that few halo stars have been contributed by stripping of satellites that have survived self$-$bound until the present. We shall return to this issue below.

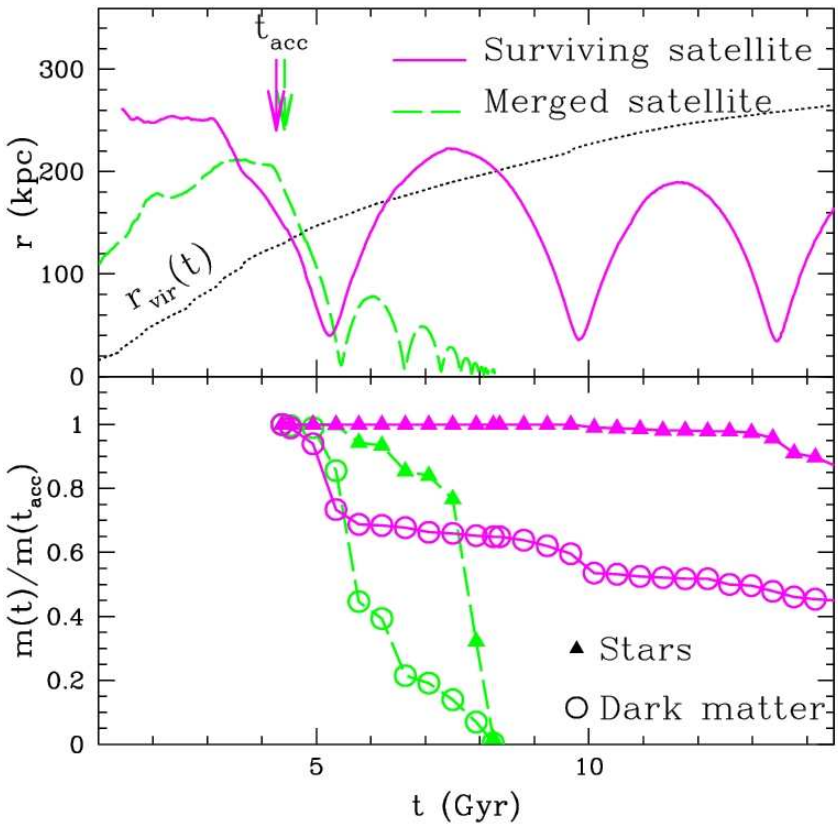

Figure 27. *Top panel:* Orbital evolution of two satellites, chosen to illustrate the case of a system that merges quickly with the primary and of another that survives as a self−bound entity until $z = 0$. Curves show the distance from the primary to the self−bound stellar core of the satellite as a function of time. The dotted line shows the evolution of the virial radius of the primary galaxy, and the arrow indicates the time, t_{acc}, when the satellites are first accreted into the primary's halo. Although both satellites are accreted more or less at the same time, they are not a physical pair and evolve independently. *Bottom panel:* The evolution of the satellites' bound mass of stars and dark matter, normalized to the values computed at the time of accretion. Note that the stellar component is much more resilient to the effect of tides.

4.4.4 *Application to the Local Group*

The lack of strong kinematical bias between satellites and dark matter may be used to estimate the virial velocity of the Milky Way and M31. For example, assuming that the radial velocity dispersion of the satellites is related to the virial velocity by $\sigma_r \sim 0.9\,(\pm 0.2) V_{vir}$ (see Figure 25; the uncertainty is just the rms scatter from our eight simulations), we obtain $V_{vir}^{MW} \sim 109 \pm 22$ km/s from the ~ 99 km/s Galactocentric radial velocity dispersion of the eleven brightest satellites (see, e.g., the compilation of van den Bergh 1999).

The same procedure may be applied to M31 satellites. Taking into account projection effects, we find that the line−of−sight satellite velocity dispersion is $\sigma_{los} \sim 0.8(\pm 0.2) V_{vir}$. Taking the 16 brightest satellites within 300 kpc from the center of M31, we find $\sigma_{los} \sim 111$ km/s, implying $V_{vir}^{M31} \sim 138 \pm 35$ km/s. We use here the compilation of McConnachie & Irwin (2006), complemented with data for And XIV from Majewski et al (2007), and for And XII from (Chapman et al 2007, submitted).

These results imply that the virial radius of the Milky Way is $r_{vir}^{MW} \sim 240$ kpc. Our simulations predict that half of the brightest satellites should be enclosed within ~ 90 kpc, which compares favourably with observations: half of the eleven brightest satellites are within ~ 90.1 kpc from the center of the Milky Way. Contrary to the arguments of Taylor et al. (2005), no substantial bias between satellites and dark matter is required to explain the MW satellite spatial distribution, provided that one accepts a virial radius as small as ~ 240 kpc.

The same argument, applied to M31, suggests that half of the 16 satellites within its virial radius ($r_{vir}^{M31} \sim 300$ kpc) must be within ~ 111 kpc, compared with the observational value of ~ 165 kpc. Note that these radii are actual distances to M31, rather than projections.

Despite the sizable statistical uncertainty inherent to the small number of satellites in these samples, it is interesting that both of the virial velocity estimates mentioned above are significantly lower than the rotation speed measured for these galaxies in the inner regions; $V_{rot}^{MW} \sim 220$ km/s and $V_{rot}^{M31} \sim 260$ km/s. These low virial velocity estimates are in line with recent work that advocates relatively low masses for the giant spirals in the Local Group (Klypin et al. 2002; Seigar et al. 2006; Abadi et al. 2006; Smith et al. 2006).

If confirmed, this would imply that the circular velocity should drop steadily with radius in the outer regions of these galaxies. As discussed by Abadi et al (2006), this may be the result of "adiabatic contraction" of the dark matter halo following the assembly of the luminous galaxy. However, such result may be difficult to reconcile with semianalytic models of galaxy formation, which favor a better match between V_{rot} and V_{vir} (Croton et al 2006, Bower et al 2006). Final word on this issue needs further data to place better constraints on the mass of the halo of the Local Group spirals at large distances, as well as improved semianalytic modeling that re−examines critically the response of the dark halo to the formation of the luminous galaxy. At least from the observational point of view, the steady pace of discovery of new satellites of M31 and MW facilitated by digital sky surveys implies that it should be possible to revisit this issue in the near future with much improved statistics.

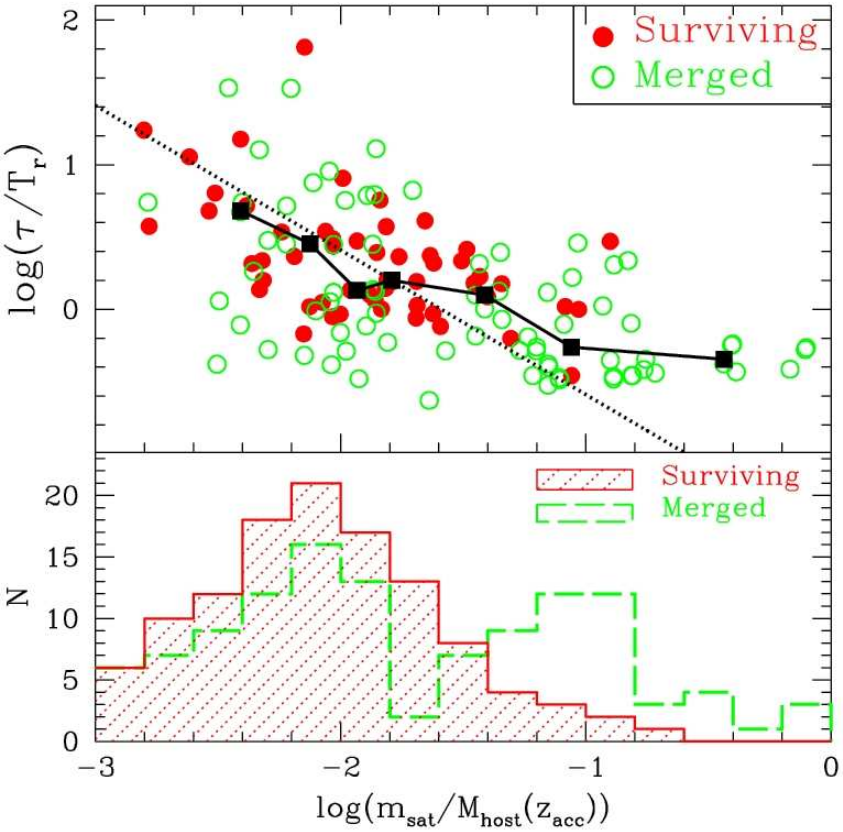

Figure 28. *Top panel:* Orbital decay timescale of satellites, τ, shown as a function of satellite mass. Decay timescales are computed by fitting an exponential law to the evolution of the apocentric radius of a satellite, and is shown in units of the (radial) orbital period measured at accretion time. Satellite masses (dark+baryons) are scaled to the total mass of the host at t_{acc}. Filled and open circles correspond to satellites that have, respectively, survived or merged with the primary by $z = 0$. Filled squares show the median decay timescale after splitting the sample into equal−number mass bins. More massive satellites spiral in faster due to the effects of dynamical friction. *Bottom panel:* Histogram of surviving and merged satellites as a function of satellite mass. Note the strong mass bias of surviving satellites relative to merged ones.

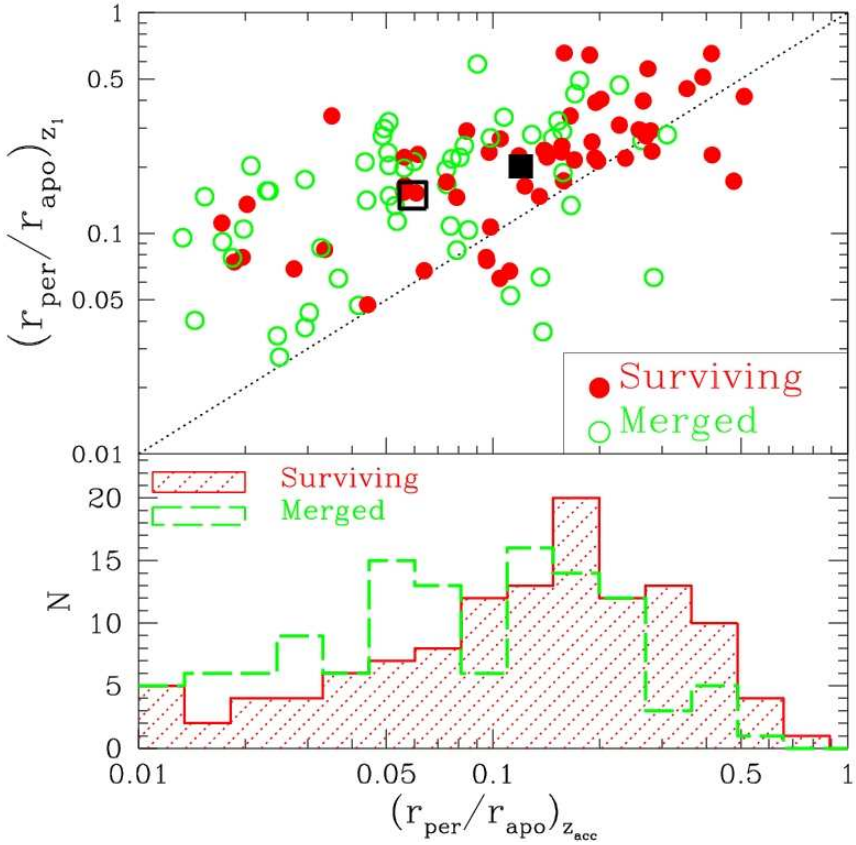

Figure 29. *Top panel:* Orbital pericenter−to−apocenter ratio measured at two different times during the evolution of a satellite. Values on the horizontal axis correspond to the time of accretion whereas values on the vertical axis are computed once dynamical friction has eroded the apocentric distance to $\sim e^{-1}$ of its turnaround value. Most satellites lie above the 1:1 dotted line, indicating significant orbital circularization by dynamical friction. Open and filled circles correspond, respectively, to merged or surviving satellites at $z = 0$. Open and filled squares mark the median of each of those populations, respectively. *Bottom panel:* Histogram of pericenter−to−apocenter ratio at the time of accretion for surviving and merged satellites. Note that satellites originally on more eccentric orbits tend to merge faster.

4.4.5 *Satellite evolution*

Merging and survival

Satellites are affected strongly by the tidal field of the primary, and evolve steadily after being accreted into the halo of the host galaxy. This is illustrated in Figure 27, where the upper panel shows the evolution of the galactocentric distance for two satellites in one of our simulations. These two satellites follow independent accretion paths into the halo of the primary galaxy; after initially drifting away from the galaxy due to the universal expansion, they reach a turnaround radius of a few hundred kpc and are then accreted into the virial radius of the primary at similar times, ~ 4.5 Gyr after the Big Bang ($z \sim 1.5$). The accretion is indicated by the intersection between the trajectory of each satellite in the upper panel of Figure 27 and the dotted line, which shows the evolution of the virial radius of the main progenitor of the primary.

We define the time that the satellite first enters the virial radius of the primary as the *accretion time*, t_{acc}, or z_{acc}, if it is expressed as a redshift. Because masses, radii, and other characteristic properties of a satellite are modified strongly by the tides that operate inside the halo of the primary, it is useful to define the satellite's properties at the time of accretion, and to refer the evolution to the values measured at that time.

One example of the effect of tides is provided by the self−bound mass of the satellite, whose evolution is shown in the bottom panel of Figure 27. The dark matter that remains bound to the satellite (relative to that measured at accretion time) is shown by open symbols; the bound mass in stars is shown by solid triangles. One of the satellites (dashed lines) sees its orbit eroded quickly by dynamical friction, and merges with the primary less than 4 Gyr after accretion, at which point the self−bound mass of the dark matter and stellar components drops to zero. The orbital period decreases rapidly as the satellite sinks in; we are able to trace almost 5 complete orbits before disruption although, altogether, the satellite takes only 2.5 Gyr to merge after the first pericentric passage, a time comparable to just half the orbital period at accretion time.

As the satellite is dragged inwards by dynamical friction dark matter is lost much more readily than stars; after the first pericentric passage only about 40% of the original dark mass remains attached to the satellite, compared with 85% of the stars. This is a result of the strong spatial segregation between stars and dark matter which results from gas cooling and condensing at the center of dark halos before turning into stars. Stars are only lost in large numbers at the time of merger, when the satellite is fully disrupted by the tides.

The second satellite (solid lines in Figure 27) survives as a self−bound entity until the end of the simulation. Its orbit is affected by dynamical friction, but not as drastically as the merged satellite: after completing 3 orbits, its apocentric distance has only dropped from ~ 250 kpc at turnaround ($t_{ta} \sim 3$ Gyr) to ~ 180 kpc at $z = 0$. The stars in the satellite survive almost unscathed; more than 85% of stars remain bound to the satellite at the end of the simulation, although only $\sim 45\%$ of the dark matter is still attached to the satellite then.

As expected from simple dynamical friction arguments, the final fate of a satellite regarding merging or survival depends mainly on its mass and on the eccentricity of its orbit. The "merged" satellite in Figure 27 is ~ 6 times more massive than the

"surviving" one and is on a much more eccentric orbit: its first pericentric radius is just ~ 20 kpc, compared with 45 kpc for the surviving satellite. More massive satellites on eccentric orbits spiral in faster than low−mass ones, making themselves more vulnerable to tides and full disruption.

This is confirmed in Figure 28, where we show the orbital decay timescale of all satellites identified in our simulations as a function of their mass. Satellite masses are shown in units of the mass of the primary galaxy at the time of accretion, and decay timescales, τ, are normalized to the orbital period of the satellite, measured at the same time. (The timescale τ is computed by fitting the evolution of the apocentric distance of the satellite, a good proxy for the orbital energy, to an exponential law.)

Surviving satellites are shown as filled circles in Figure 28, whereas open circles denote merged satellites. More massive satellites clearly spiral in faster: τ is typically less than an orbital period for a satellite whose mass exceeds $\sim 20\%$ of the primary. On the other hand, decay timescales are often larger than ~ 10 orbital periods for satellites with masses below 1% of the primary. The dotted line shows the $\tau \propto m^{-1}$ relation expected from simple dynamical friction arguments Binney & Tremaine (1987) . Most satellites follow this trend, except perhaps for the most massive systems, but this may just reflect difficulties estimating τ for systems on very rapidly decaying orbits, because of poor time sampling. The main result of these trends is a severe underrepresentation of surviving satellites amongst massive satellites, as shown by the distribution of satellite masses in the bottom panel of Figure 28.

Orbital circularization

As they are dragged inwards by dynamical friction, the orbital energy of the satellites is affected more than its angular momentum and, as a result, the satellites' orbits become gradually more circular. This is shown in Figure 29, where we plot the ratio between apocentric and pericentric distance, r_{per}/r_{apo}, at the time of accretion versus the same quantity, but measured after dynamical friction has eroded r_{apo} to e^{-1} of its value at accretion.

As in Figure 28, open and filled circles indicate "merged" and "surviving" satellites at $z = 0$. The vast majority of the points lie above the 1:1 line, indicating that the orbits have become significantly less eccentric with time. Some points lie below the dotted line, indicating the opposite effect; however, most of these cases correspond to complex accretion where the satellite comes as a member of a pair of satellites and is subject to three−body interactions during accretion (we address this issue in the next Chapter).

The large open and filled squares indicate the median r_{per}/r_{apo} for merged and surviving satellites, respectively. Clearly, the eccentricity of the orbit is important for the chances of survival of a satellite: most satellites originally on very eccentric orbits have merged with the primary by $z = 0$, and the reverse is true for surviving satellites (see bottom panel in Figure 29).

Satellites that merge with the primary by $z = 0$ experience on average a more substantial circularization of their orbits; the median r_{per}/r_{apo} evolves from 0.06 to roughly 0.15 in the time it takes their orbital energies to decrease by e^{-1}. Further circularization may be expected by the time that the satellite merges with the primary

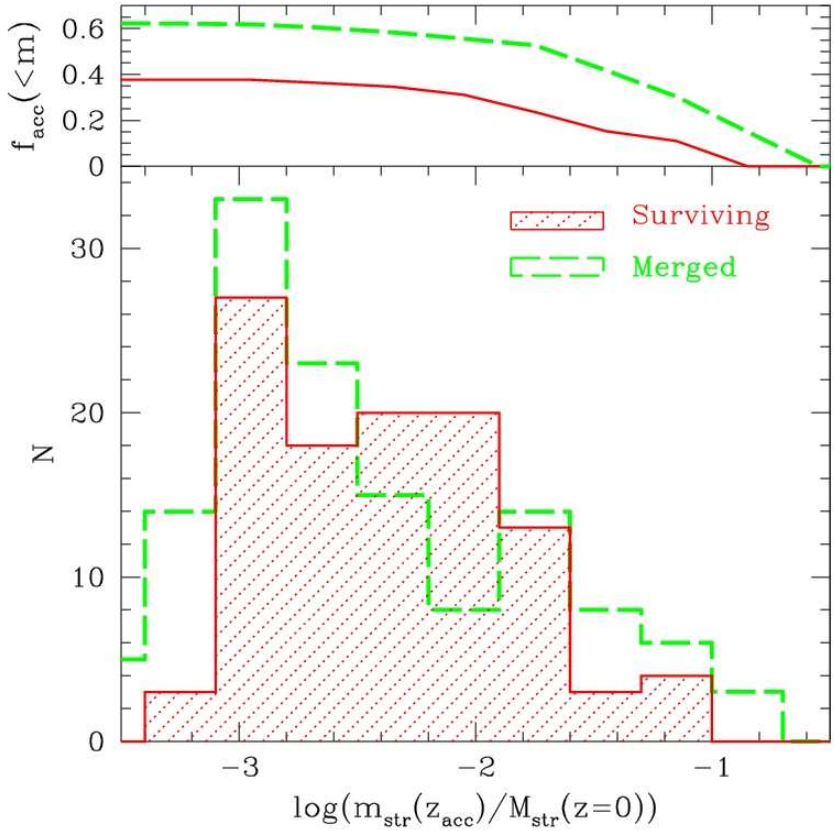

Figure 30. Distribution of satellite stellar masses measured at the time of accretion into the host halo, and normalized to the stellar mass of the primary at $z = 0$ (bottom panel). The shaded histogram corresponds to satellites that remain self−bound at $z = 0$; the other histogram corresponds to satellites that merge with the primary before $z = 0$. The curves in the top panel indicate the cumulative fraction of all *accreted stars* contributed by each of these two populations. Note that the "building blocks" of the stellar halo are significantly more massive than the average surviving satellite. On average, accretion events bring about 25% of the total number of stars into the primary, 40% of which remains attached to satellites until $z = 0$. The remainder belongs to "merged" satellites, the majority of which make up the stellar halo. The total number of stars contributed by disrupted satellites exceed those locked in surviving satellites by $\sim 50\%$.

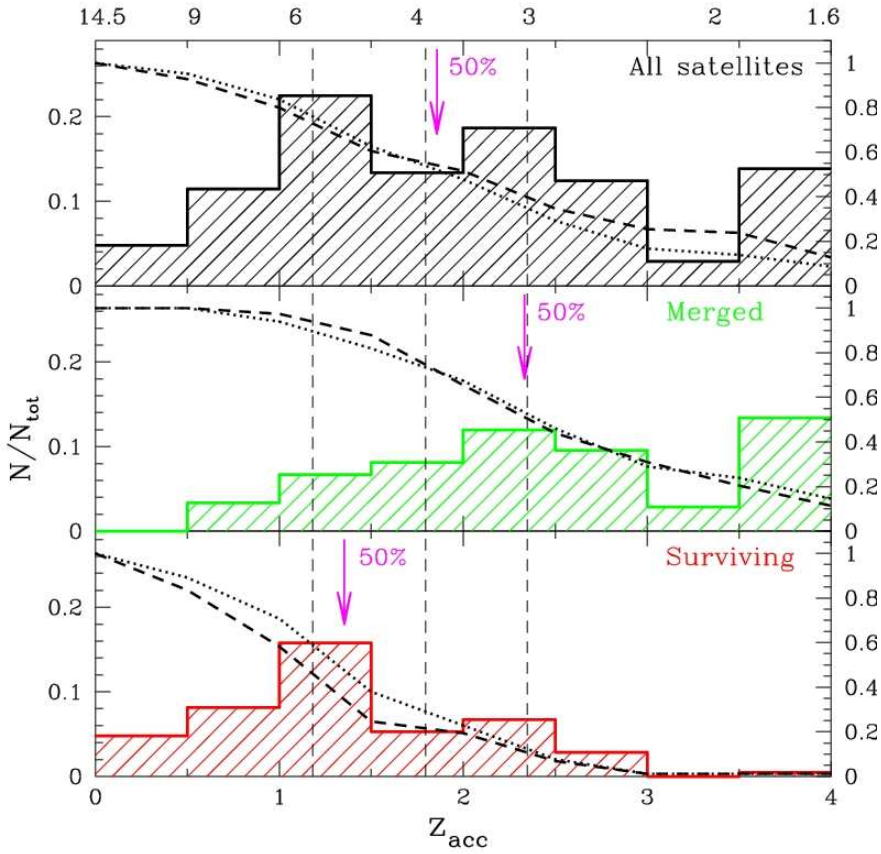

Figure 31. Accretion redshift distribution of surviving (bottom panel), merged (middle) and all (top) satellites in our simulations. All histograms are scaled to the total number of satellites for ease of comparison between panels. Dashed vertical lines indicate the (average) redshift where the primary galaxy has accreted 25%, 50% and 75% of its *total* mass at $z = 0$. In each panel the arrow shows the median satellite accretion redshift. The dotted curves trace the cumulative distribution of satellites (by number) as a function of $z_{\rm acc}$ (scale on right). Solid lines are like dotted ones, but by mass.

and, under the right circumstances, a satellite may even reach a nearly circular orbit before merging (see, e.g., Abadi et al 2003b, Meza et al 2005).

Orbital circularization has been proposed as an important factor to consider when interpreting the effects of satellite accretion events (although see Colpi et al 1999 for a different viewpoint). Abadi et al (2003b) argue, for example, that a satellite on a circularized orbit might have contributed a significant fraction of the thick−disk stars (and perhaps even some old thin−disk stars) of the Milky Way. A further example is provided by the "ring" of stars discovered by the SDSS in the anti−galactic center direction (Newberg et al. 2002; Yanny et al. 2003; Helmi et al. 2003), which has been successfully modeled as debris from the recent disruption of a satellite on a nearly circular orbit in the outskirts of the Galactic disk (Peñarrubia et al. 2006). Since it is unlikely that the satellite formed on such orbit (otherwise it would have been disrupted much earlier) its orbit has probably evolved to become more bound and less eccentric as dynamical friction brought the satellite nearer the Galactic disk, in agreement with the trend shown in Figure 29.

4.4.6 *Satellites and stellar halo: similarities and differences*

The main result of the trends discussed in the preceding secction is the obvious mass bias present in the population of surviving satellites: massive satellites merge too quickly to be fairly represented amongst satellites present at any given time. This is shown in the bottom panel of Figure 28; although the accretion of satellites with masses exceeding 10% of the host (at the time of accretion) is not unusual, few have survived self−bound until $z = 0$.

This is also true when expressed in terms of the total stellar mass that these accretion events have contributed to the simulated galaxy. As shown in Figure 30, merged satellites dominate the high−mass end of the distribution of accreted satellites, and make up on average $\sim 60\%$ of all accreted stars. Half of this contribution comes in just a few massive satellites exceeding 10% of the final mass in stars of the host (see upper panel in Figure 30). On the other hand, surviving satellites contribute on average $\sim 40\%$ of all accreted stars and have a combined stellar mass of about 12% of the host at $z = 0$. Half of them are contributed by satellites less than $\sim 3\%$ as massive as the host at $z = 0$.

Because of the strong orbital decay dependence on mass, surviving satellites are also biased relative to the overall population of accreted material in terms of accretion time. This is shown quantitatively in Figure 31, which shows the $z_{\rm acc}$ distribution for all satellites accreted since $z = 4$ (top panel). The bottom and middle panels, respectively, split this sample between satellites that have either survived or merged with the host by $z = 0$. The vertical lines in this figure illustrate the average mass accretion history of the hosts in our simulation series: from left to right, the vertical lines indicate the average redshift when the last 25%, 50%, and 75% of the mass were assembled into the virial radius of the host.

The accreted satellites, as a whole, trace very well this accretion history, as may be seen from the histogram in the top panel, or by the dotted line, which indicates the cumulative accretion history (scale on right). Just like the total mass, half of all

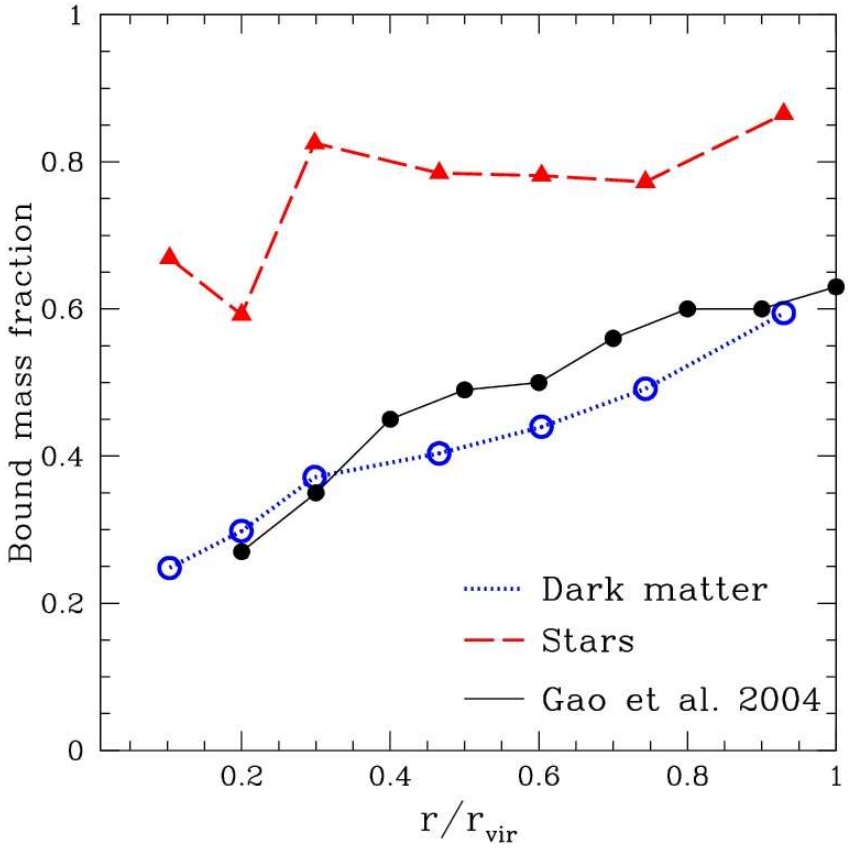

Figure 32. Mass fraction attached to surviving satellites at $z = 0$, shown as a function of radius, normalized to the virial radius of the host. The open circles are the results of the dark matter–only simulations of (Gao et al. 2004b), which are in very good agreement with ours. This figure shows that, although surviving satellites have lost a significant fraction of their dark mass to tides, their stellar components have survived almost unscathed. Overall, satellites inside the virial radius have conserved about 40% of their original dark mass, and ~ 75% of their stars. This suggests that stars stripped off surviving satellites are in general an unimportant contributor to the stellar halo, and highlights the need for simulations that include gas cooling and star formation to estimate the importance of tidal stripping in the satellite population.

satellites were accreted before $z \sim 1.8$ (see arrow labelled "50%"). The results are quite different for "merged satellites"; half of them were actually accreted before $z = 2.4$, which corresponds to a lookback time of ~ 2.7 Gyr. Essentially no satellite accreted after $z = 0.5$ has merged with the primary. Surviving satellites, on the other hand, are substantially biased towards late accretion. Half of them were only accreted after $z = 1.4$, and the last 25% since $z \sim 1$.

Since stars brought into the galaxy by merged satellites contribute predominantly to the stellar halo (see, e.g., Abadi et al 2006), this result shows convincingly that substantial differences must be expected between the stellar halo and surviving satellite population in a galaxy built hierarchically. *The "building blocks" of the stellar halo were on average more massive and were accreted and disrupted much earlier than the population of satellites that survive until the present.*

Our results provide strong support for the semianalytic modeling results of Bullock & Johnston (2005). Despite the differences in modeling techniques (these authors use theoretical merger trees to simulate Monte Carlo accretion histories and a semianalytic approach to dinstinguish stars and dark matter within accreted satellites), our results agree well. For example, they find that $\sim 80\%$ of the stellar halo is contributed by the ~ 15 most massive disrupted satellites; we find, on average, 70%. The median accretion time for disrupted satellites is ~ 9 Gyr ago; we find ~ 10.5 Gyr. Lastly, they find that the median accretion time of surviving satellites was as recently as ~ 5 Gyr in the past; we find ~ 8.5 Gyr.

As discussed by Font et al. (2006a,b), these results may help to explain the differences between the abundance patterns of halo stars in the solar neighbourhood and in Galactic dwarfs (Fuhrmann 1998; Shetrone et al. 2001,2003; Venn et al. 2004). Although stars in both the halo and satellites are metal−poor, the stellar halo is, at fixed [Fe/H], more enhanced in α elements than stars in the dwarfs, suggesting that its star formation and enrichment proceeded more quickly and thoroughly than in Galactic satellites. This is qualitatively consistent with the biases in the surviving satellite population mentioned above. Because of the limited numerical resolution of our simulations and our inefficient feedback recipe, we are unable to follow accurately the metal enrichment of stars in our simulations. Although this precludes a more detailed quantitative comparison between simulations and observations, we regard the distinction between satellite and stellar halo reported here as certainly encouraging.

One final issue to consider is that, in principle, stars may also end up in the stellar halo as a result of partial stripping of surviving satellites. If substantial, this process might make stars in the stellar halo difficult to differentiate from those attached to satellites, despite the biases in mass and accretion time discussed above. As it turns out, stripping of surviving satellites adds an insignificant fraction of stars to the halo in our simulations; stars stripped from surviving satellites make up a small fraction ($\sim 6\%$) of all halo stars.

This is shown in Figure 32, where we plot the fraction of stars and dark matter that remains attached to surviving satellites as a function of the distance to the center of the galaxy. As shown by the filled triangles, more than 75% of the stars brought into the system by surviving satellites remain attached to them at $z = 0$. We conclude that the bulk of the halo population is not affected by stars stripped from existing satellites,

and that the substantial difference between the stellar population of Galactic dwarfs and of the stellar halo predicted above is robust.

4.5 Conclusions from this Chapter

We have analyzed the properties of satellite galaxies formed in a suite of eight N−body/gasdynamical simulations of galaxy formation in a ΛCDM universe. Our simulations are able to resolve, at $z = 0$, the ~ 10 most luminous satellites orbiting around $\sim L_*$ galaxies. We also track satellites that have merged with, or been disrupted fully by, the primary galaxy at earlier times, giving us a full picture of the contribution of accreted stars to the various dynamical components of the galaxy.

As discussed in an earlier paper of our group (Abadi et al 2006), the stellar halo consists of stars stripped from satellites that have been fully disrupted by the tidal field of the primary. Our analysis here focuses on the spatial distribution, kinematics, and merging history of the population of surviving and merged satellites, and on their significance for the formation of the stellar halo. Our main results may be summarized as follows.

- The spatial distribution of satellites at $z = 0$ is consistent with that of the dark matter in the primary galaxy's halo, and is significantly more extended than the stellar halo. On average, half of the ~ 10 brightest satellites are found within $0.37\, r_{vir}$, comparable to the half−mass radius of the dark matter component. The half−mass radius of the stellar halo is, on the other hand, only $0.05\, r_{vir}$.

- The kinematics of the satellite population is also similar to the dark matter's. Satellite velocities are mildly anisotropic in the radial direction, with $\beta_{sat} \sim 0.3 - 0.4$, but not as extreme as stars in the halo, which are found to have $\beta_{halo} \sim 0.6 - 0.8$ in the outskirst of the system. Satellite velocity dispersions drop from the center outwards, and decrease by about a factor of two at the virial radius from their central value. Overall, the velocity dispersion of the satellite population is found to provide a resonable estimate of the halo's virial velocity: $\sigma_{sat}/V_{vir} \sim 0.9 \pm 0.2$, where the uncertainty is the rms of the eight simulations.

- The orbits of satellites evolve strongly after accretion as a result of dynamical friction with the host halo and of mass stripping by tides. More massive satellites spiral in faster than less massive systems and are disrupted quickly as they merge with the primary, adding their stars mainly to the stellar halo. The orbits of satellites with masses exceeding 10% of the host mass decay on exponential timescales shorter than an orbital period, and merge shortly after accretion. Merged satellites typically make up $\sim 63\%$ of all accreted stars in a galaxy, a substantial fraction of which (57%) was contributed by these few most massive satellites.

- Surviving satellites are a substantially biased tracer of the whole population of stars accreted by a galaxy. In contrast with the "merged" satellites that build up the halo, surviving satellites are predominantly low−mass systems that have been accreted recently. Half of the stars in the stellar halo were accreted before

$z \sim 2.2$, and were in satellites more massive than $\sim 6\%$ of the host at the time of accretion. In contrast, half of the stars in surviving satellites were brought into the system as recently as $z \sim 1.6$, and formed in systems with masses less than 3% of the host.

- Satellite orbits are continuosly circularized by dynamical friction as they orbit within the primary's halo. The pericenter−to−apocenter ratio typically doubles once the orbital binding energy of the satellite has increased by a factor of e.
- Stars stripped from satellites that remain self−bound until the present make up an insignificant fraction of all stars accreted by a galaxy, showing that, once started, the disruption process of the stellar component of a satellite progresses on a very short timescale. Surviving satellites conserve at $z = 0$ about 75% of the stars they had at accretion time. Their surrounding dark halos, on the other hand, have been stripped of more than $\sim 40\%$ of their mass.

Our results offer a framework for interpreting observations of the satellite population around luminous galaxies and for extracting information regarding their dark matter halos. They also show that hierarchical galaxy formation models may explain naturally the differences in the properties of stars in the stellar halo and in Galactic satellites highlighted by recent observational work. Although our modeling of star formation is too simplistic (and our numerical resolution too poor) to allow for a closer, quantitative assessment of this issue, it is encouraging to see that, despite their differences, stellar halos and satellites may actually be both the result of the many accretion events that characterize galaxy formation in a hierarchically clustering universe.

5

THE ORIGIN OF EXTREME HIGH−VELOCITY SATELLITES

5.1 Abstract

We examine in more detail the orbits of the satellite galaxies analyzed in Chapter 4. Most satellites follow conventional orbits; after turning around, they accrete into their host halo and settle on orbits whose apocentric radii are steadily eroded by dynamical friction. As a result, satellites associated with the primary are typically found within its virial radius, r_{vir}, and have velocities consistent with a Gaussian distribution with mild radial anisotropy. However, a number of outliers are also present. We find that a surprising number (about one−third) of satellites identified at $z = 0$ are on unorthodox orbits, with apocenters that exceed their turnaround radii. These include a number of objects with extreme velocities and apocentric radii at times exceeding $\sim 3.5\, r_{vir}$ (or, e.g., $\geqslant$ 1 Mpc when scaled to the Milky Way). This population of satellites on extreme orbits consists typically of the faint member of a satellite pair whose kinship is severed by the tidal field of the primary during first approach. Under the right circumstances, the heavier member of the pair remains bound to the primary, whilst the lighter companion is ejected onto a highly−energetic orbit. Since the concurrent accretion of multiple satellite systems is a defining feature of hierarchical models of galaxy formation, a fairly robust prediction of this scenario is that at least some of these extreme objects should be present in the Local Group. We speculate that this three−body ejection mechanism may be the origin of (i) some of the newly discovered high−speed satellites around M31 (such as Andromeda XIV); (ii) some of the distant fast−receding Local Group members, such as Leo I; and (iii) the oddly isolated dwarf spheroidals Cetus and Tucana in the outskirts of the Local Group. Our results suggest that care must be exercised when using the orbits of the most weakly bound satellites to place constraints on the total mass of the Local Group.

5.2 Introduction

The study of Local Group satellite galaxies has been revolutionized by digital imaging surveys of large areas of the sky. More than a dozen new satellites have been discovered in the past couple of years (Zucker et al. 2004, 2006; Willman et al. 2005; Martin et al. 2006; Belokurov et al. 2006, 2007; Irwin et al. 2007; Majewski et al. 2007) , due in large part to the completion of the Sloan Digital Sky Survey (York et al. 2000; Strauss et al. 2002) and to concerted campaigns designed to image in detail the Andromeda galaxy and its immediate surroundings (Ibata et al. 2001; Ferguson et al. 2002; Reitzel

& Guhathakurta 2002; McConnachie et al. 2003; Rich et al. 2004; Guhathakurta et al. 2006; Gilbert et al. 2006; Chapman et al. 2006, Ibata et al. 2007 submitted).

At the same time, once velocities and distances are secured for the newly-discovered satellites, dynamical studies of the total mass and spatial extent of the Local Group will gain new impetus. These studies have a long history (Little & Tremaine 1987, Zaritsky et al. 1989, Kochanek 1996, Wilkinson & Evans 1999; Evans & Wilkinson 2000; Battaglia et al. 2005), but their results have traditionally been regarded as tentative rather than conclusive, particularly because of the small number of objects involved, as well as the sensitivity of the results to the inclusion (or omission) of one or two objects with large velocities and/or distances (Zaritsky et al. 1989, Kochanek 1996; Sakamoto et al. 2003). An enlarged satellite sample will likely make the conclusions of satellite dynamical studies more compelling and robust.

To this end, most theoretical work typically assumes that satellites are in equilibrium, and use crafty techniques to overcome the limitations of small−N statistics when applying Jeans' equations to estimate masses (see, e.g. Little & Tremaine 1987, Wilkinson & Evans 1999; Evans & Wilkinson 2000). With increased sample size, however, follow enhanced opportunities to discover satellites on unlikely orbits; i.e., dynamical "outliers" that may challenge the expectations of simple−minded models of satellite formation and evolution. It is important to clarify the origin of such systems, given their disproportionate weight in mass estimates.

One issue to consider is that the assumption of equilibrium must break down when considering outliers in phase space. This is because the finite age of the Universe places an upper limit to the orbital period of satellites observed in the Local Group; high-speed satellites have typically large apocenters and long orbital periods, implying that they cannot be dynamically well−mixed and casting doubts on the applicability of Jeans' theorem-inspired analysis tools.

To make progress, one possibility is to explore variants of the standard secondary infall model (Gunn & Gott 1972; Gott 1975; Gunn 1977; Fillmore & Goldreich 1984), where satellites are assumed to recede initially with the universal expansion, before turning around and collapsing onto the primary due to its gravitational pull. This is the approach adopted by Zaritsky & White (1994) in order to interpret statistically the kinematics of observed satellite samples without assuming well−mixed orbits and taking into account the proper timing and phase of the accretion process.

In the secondary infall accretion sequence, satellites initially farther away accrete later, after turning around from larger turnaround radii. The turn−around radius grows with time, at a rate the depends on the mass of the primary and its environment, as well as on the cosmological model. Three distinct regions surround a system formed by spherical secondary infall (see, e.g. Bertschinger 1985; Navarro & White 1993): (i) an outer region beyond the current turnaround radius where satellites are still expanding away, (ii) an intermediate region containing satellites that are approaching the primary for the first time, and (iii) an inner, "virialized" region containing all satellites that have turned around at earlier times and are still orbiting around the primary. To good approximation, the latter region is delineated roughly by the conventional virial radius of a system. The turnaround radius is of order $r_{ta} \sim 3\, r_{vir}$ (see, e.g. White et al. 1993).

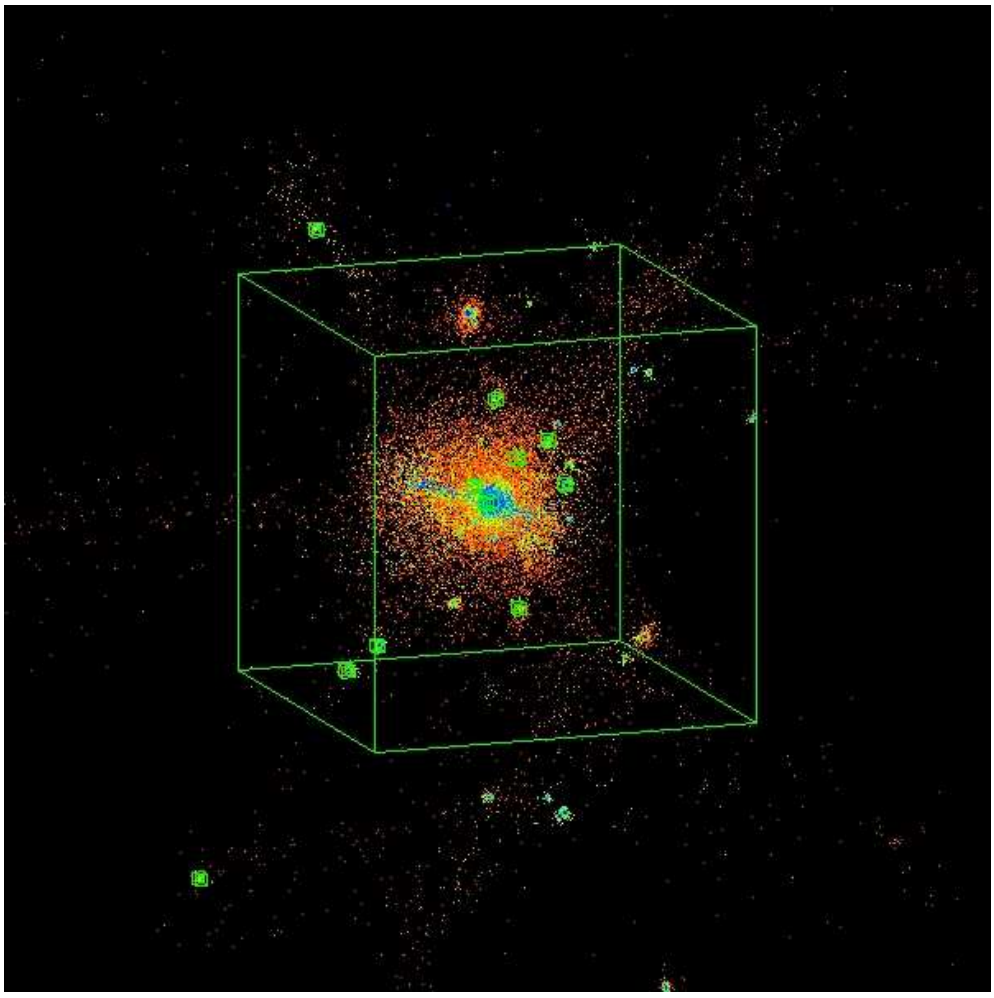

Figure 33. Star particles in one of our simulations, shown at $z = 0$. Particles are colored according to the age of the star; blue means a star is younger than $\simeq 1$ Gyr, red that it is older than $\simeq 10$ Gyr. The large box is $2\,r_{vir}$ (632 kpc) on a side and centered on the primary galaxy. More than 85% of all stars are in the inner regions of the primary, within about ~ 20 kpc from the center (for more details see Abadi et al. 2006). surround the satellites "associated" with the primary galaxy; i.e., satellites that have been within r_{vir} in the past. Note that a few "associated" satellites lie well beyond the virial boundary of the system. Two of these satellites are highlighted for analysis in Figures 34 and 38.

We note a few consequences of this model. (a) Satellites outside the virial radius are on their first approach to the system and thus have not yet been inside r_{vir}. (b) Satellites inside the virial radius have apocentric radii that typically do not exceed r_{vir}. (c) The farther the turnaround radius the longer it takes for a satellite to turn aroud and accrete and the higher its orbital energy. (d) Satellites with extreme velocities will, in general, be those completing their first orbit around the primary. Velocities will be maximal near the center, where satellites may reach speeds as high as $\sim 3\,V_{vir}$. (e) Since all satellites associated with the primary are bound (otherwise they would not have turned around and collapsed under the gravitational pull of the primary), the velocity of the highest−speed satellite may be used to estimate a lower limit to the escape velocity at its location and, thus, a lower bound to the total mass of the system.

Hierarchical galaxy formation models, such as the current ΛCDM paradigm, suggest further complexity in this picture. Firstly, although numerical simulations show that the sequence of expansion, turnaround and accretion of satellites described above is more or less preserved in hierarchical models, the evolution is far from spherically symmetric (Ghigna et al. 1998; Jing & Suto 2002; Navarro et al. 2004; Bailin & Steinmetz 2005; Knebe & Weiβner 2006). Much of the mass (as well as many of the satellites) is accreted through filaments of matter embedded within sheets of matter formation (Navarro et al. 2004) . The anisotropic collapse pattern onto a primary implies that the turnaround "surface" won't be spherical and that the virial radius may not contain *all* satellites that have completed at least one orbit around the primary (see, e.g. Balogh et al. 2000; Diemand et al. 2007) .

More importantly for the purposes of this Chapter, in hierarchical models galaxy systems are assembled by collecting smaller systems which themselves, in turn, were assembled out of smaller units. This implies that satellites will in general not be accreted in isolation, but frequently as part of larger structures containing multiple systems. This allows for complex many−body interactions to take place during approach to the primary that may result in substantial modification to the orbits of accreted satellites.

We address this issue in this Chapter using the population of simulated satellites described in Chapter 4. We analyze and discuss the results in § 5.3. We speculate on possible applications to the Local Group satellite population in §5.4 and conclude with a brief summary of this Chapter in § 5.5.

5.3 Results and Discussion

5.3.1 *Satellites on conventional orbits*

The evolution of satellites in our simulations follows roughly the various stages anticipated by our discussion of the secondary infall model; after initially receding with the universal expansion, satellites turn around and are accreted into the primary. Satellites massive enough to be well resolved in our simulations form stars actively before accretion and, by the time they cross the virial radius of the primary, much of their baryonic component is in a tighly bound collection of stars at the center of their own dark matter halos.

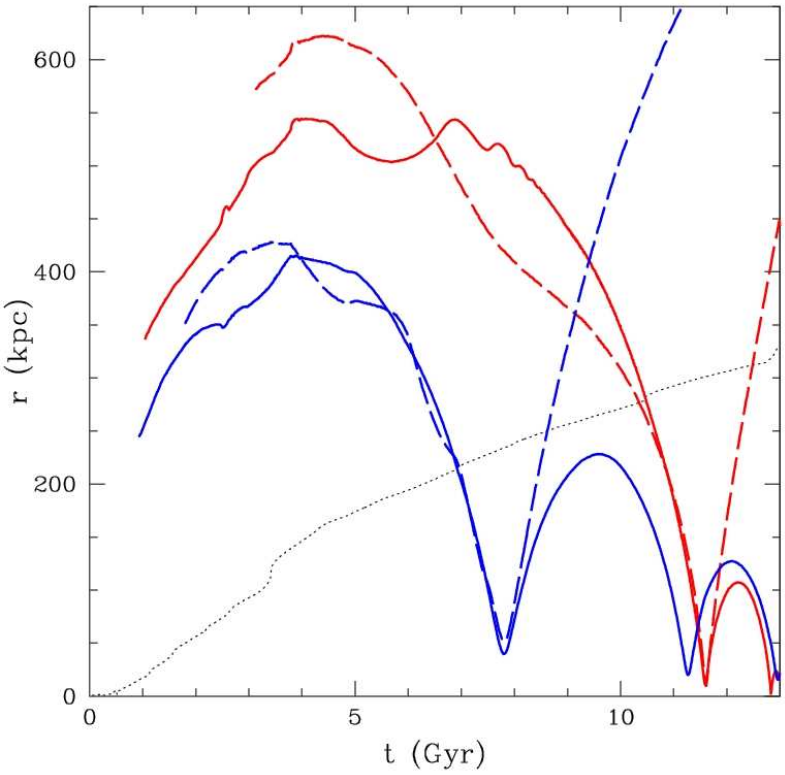

Figure 34. Distance to the primary as a function of time for four satellites selected in one of our simulations. The four satellites are accreted into the primary in two pairs of unequal mass. The heavier satellite of the pair, shown by solid lines, follows a "conventional" orbit: after turning around from the universal expansion, it accretes into the primary on a fairly eccentric orbit which becomes progressively more bound by the effects of dynamical friction. Note that, once accreted, these satellites on "conventional" orbits do not leave the virial radius of the primary, which is shown by a dotted line. The light member of the pair, on the other hand, is ejected from the system as a result of a three–body interaction between the pair and the primary during first approach. One of the ejected satellites shown here is the "escaping" satellite identified in Figure 35; the other is the most distant "associated" satellite in that Figure. The latter is still moving toward apocenter at $z = 0$, which we estimate to be as far as $\sim 3.5\, r_{vir}$.

The stellar component of a satellite is thus quite resilient to the effect of tides and can survive as a self−bound entity for several orbits. This is illustrated by the *solid lines* in Figure 34, which show, for one of our simulations, the evolution of the distance to the primary of two satellites that turn around and are accreted into the primary at different times. As expected from the secondary infall model, satellites that are initially farther away turn around later; do so from larger radii; and are on more energetic orbits. After accretion (defined as the time when a satellite crosses the virial radius of the primary), their orbital energy and eccentricity are eroded by dynamical friction, and these two satellites do not leave the virial radius of the primary, shown by the dotted line in Figure 34. Depending on their mass and orbital parameters, some of these satellites merge with the primary shortly after accretion, while others survive as self−bound entities until $z = 0$. For short, we shall refer to satellites that, by $z = 0$, have crossed the virial radius boundary at least once as satellites "associated" with the primary.

The ensemble of surviving satellites at $z = 0$ have kinematics consistent with the evolution described above. This is illustrated in Figure 35, where we show the radial velocities of all satellites as a function of their distance to the primary, scaled to virial units. Note that the majority of "associated" satellites (shown as circles in this figure) are confined within r_{vir}, and that their velocity distribution is reasonably symmetric and consistent with a Gaussian (see figure 25). The most recently accreted satellites tend to have higher−than−average speed at all radii, as shown by the "crossed" circles, which identify all satellites accreted within the last 3 Gyr.

Crosses (without circles) in this figure correspond to satellites that have not yet been accreted into the primary. These show a clear infall pattern outside r_{vir}, where the mean infall velocity decreases with radius and approaches zero at the current turnaround radius, located at about $3\,r_{vir}$. All of these properties agree well with the expectations of the secondary infall model discussed above.

5.3.2 *Three−body interactions and satellites on unorthodox orbits*

Closer examination, however, shows a few surprises. To begin with, a number of "associated" satellites are found outside r_{vir}. As reported in previous work (see, e.g. Balogh et al. 2000; Moore et al. 2004; Gill et al. 2005; Diemand et al. 2007), these are a minority ($\sim$ 15% in our simulation series), and have been traditionally linked to departures from spherical symmetry during the accretion process. Indeed, anisotropies in the mass distribution during expansion and recollapse may endow some objects with a slight excess acceleration or, at times, may push satellites onto rather tangential orbits that "miss" the inner regions of the primary, where satellites are typically decelerated into orbits confined within the virial radius.

These effects may account for some of the associated satellites found outside r_{vir} at $z = 0$, but cannot explain why $\sim$ 33% of all associated satellites are today on orbits whose apocenters exceed their turnaround radius. This is illustrated in Figure 36, where we show a histogram of the ratio between apocentric radius (measured at $z = 0$; r_{apo}) and turnaround radius (r_{ta}). The histogram highlights the presence of two distinct populations: satellites on "conventional" orbits with $r_{apo}/r_{ta} < 1$, and

satellites on orbital paths that lead them well beyond their original turnaround radius.

Intriguingly, a small but significant fraction ($\sim$ 6%) of satellites have extremely large apocentric radius, exceeding their turnaround radius by 50% or more. These systems have clearly been affected by some mechanism that propelled them onto orbits substantially more energetic than the ones they had followed until turnaround. This mechanism seems to operate preferentially on low−mass satellites, as shown by the dashed histogram in Figure 36, which corresponds to satellites with stellar masses less than $\sim$ 3% that of the primary.

We highlight some of these objects in Figure 35, using "filled" circles to denote "associated" satellites whose apocenters at $z = 0$ exceed their turnaround radii by at least 25%. Two such objects are worth noting in this figure: one of them is the farthest "associated" satellite, found at more than $\sim 2.5\, r_{vir}$ from the primary; the second is an outward−moving satellite just outside the virial radius but with radial velocity approaching $\sim 2\, V_{vir}$. The latter, in particular, is an extraordinary object, since its radial velocity alone exceeds the nominal escape velocity[1] at that radius. This satellite is on a trajectory which, for all practical purposes, will remove it from the vicinity of the primary and leave it wandering through intergalactic space.

The origin of these unusual objects becomes clear when inspecting Figure 34. The two satellites in question are shown with *dashed lines* in this figure; each is a member of a bound *pair* of satellites (the other member of the pair is shown with solid lines of the same color). During first pericentric approach, the pair is disrupted by the tidal field of the primary and, while one member of the pair remains bound and follows the kind of "conventional" orbit described in § 5.3.1, the other one is ejected from the system on an extreme orbit. The trajectories of these two "ejected" satellites in the $r - V_r$ plane are shown by the wiggly lines in Figure 35.

These three−body interactions typically involve the first pericentric approach of a bound pair of accreted satellites and tend to eject the lighter member of the pair: in the example of Figure 34, the "ejected" member makes up, respectively, only 3% and 6% of the total mass of the pair at the time of accretion. Other interaction configurations leading to ejection are possible, such as an unrelated satellite that approaches the system during the late stages of a merger event, but they are rare, at least in our simulation series. We emphasize that not all satellites that have gained energy during accretion leave the system; most are just put on orbits of unusually large apocenter but remain bound to the primary. This is shown by the filled circles in Figure 35; many affected satellites are today completing their second or, for some, third orbit around the primary.

The ejection mechanism is perhaps best appreciated by inspecting the orbital paths of the satellite pairs. These are shown in Figure 38, where the top (bottom) panels correspond to the satellite pair accreted later (earlier) into the primary in Figure 34.

1 The notion of binding energy and escape velocity is ill−defined in cosmology; note, for example, that the *whole universe* may be considered formally bound to any positive overdensity in an otherwise unperturbed Eistein−de Sitter universe. We use here the nominal escape velocity of an NFW model (Navarro et al. 1996, 1997) to guide the interpretation. This profile fits reasonably well the mass distribution of the primaries inside the virial radius, and has a finite escape velocity despite its infinite mass. Certainly satellites with velocities exceeding the NFW escape velocity are likely to move far enough from the primary to be considered true *escapers*.

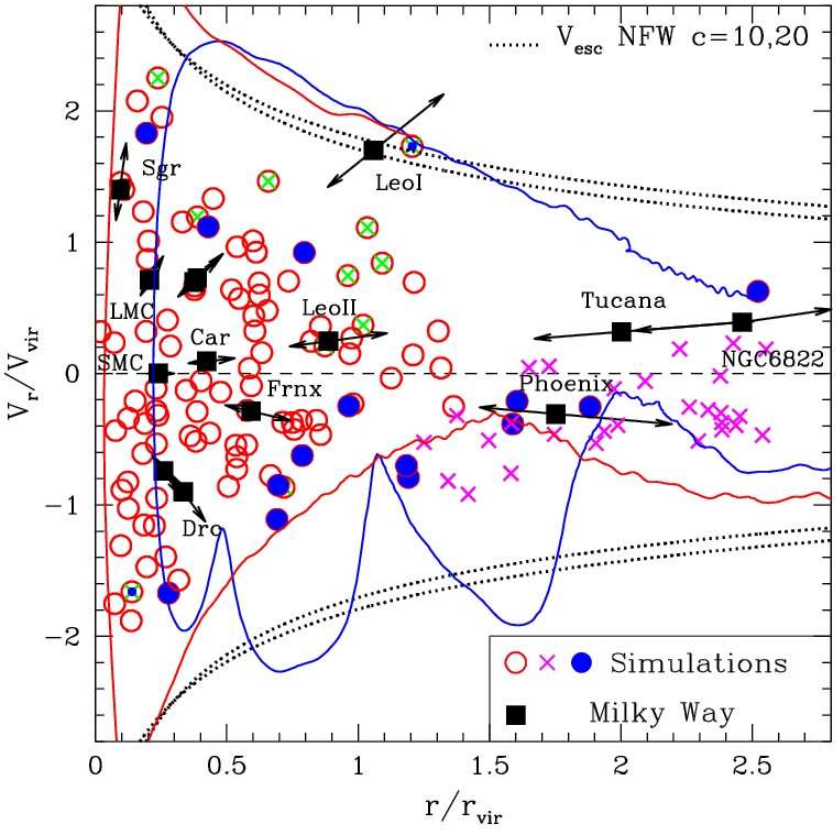

Figure 35. Radial velocity of satellites versus distance to the primary. Velocities are scaled to the virial velocity of the system, distances to the virial radius. Circles denote "associated" satellites; i.e., those that have been *inside* the virial radius of the primary at some earlier time. Crosses indicate satellites that are on their first approach, and have never been inside r_{vir}. Filled circles indicate associated satellites whose apocentric radii exceed their turnaround radius by at least 25%, indicating that their orbital energies have been substantially altered during their evolution. "Crossed" circles correspond to associated satellites that have entered r_{vir} during the last 3 Gyrs. The curves delineating the top and bottom boundaries of the distribution show the escape velocity of an NFW halo with concentration $c = 10$ and $c = 20$, respectively. Note that there is one satellite "escaping" the system with positive radial velocity. Filled squares correspond to the fourteen brightest Milky Way satellites, taken from van den Bergh (1999) (complemented with NED data for the Phoenix, Tucana and NGC6822), and plotted assuming that $V_{vir}^{MW} \sim 109$ km/s and $r_{vir}^{MW} = 237$ kpc as found in the previous Chapter. Arrows indicate how the positions of MW satellites in this plot would be altered if our estimate of V_{vir}^{MW} (and, consequently, r_{vir}^{MW}) is allowed to vary by $\pm 20\%$.

Note that in both cases, as the pair approaches pericenter, the lighter member (dashed lines) is also in the process of approaching the pericenter of its own orbit around the heavier member of the pair. This coincidence in orbital phase combines the gravitational attraction of the two more massive members of the trio of galaxies, leading to a substantial gain in orbital energy by the lightest satellite, effectively ejecting it from the system on an approximately radial orbit. The heavier member of the infalling pair, on the other hand, decays onto a much more tightly bound orbit.

Figure 38 also illustrates the complexity of orbital configurations that are possible during these three−body interactions. Although the pair depicted in the top panels approaches the primary as a cohesive unit, at pericenter each satellite circles about the primary in opposite directions: in the $y-z$ projection the heavier member circles the primary *clockwise* whereas the ejected companion goes about it *counterclockwise*. After pericenter, not only do the orbits of each satellite have different period and energy, but they differ even in the *sign* of their orbital angular momentum. In this case it would clearly be very difficult to link the two satellites to a previously bound pair on the basis of observations of their orbits after pericenter.

Although not all ejections are as complex as the one illustrated in the top panels of Figure 38, it should be clear from this figure that reconstructing the orbits of satellites that have been through pericenter is extremely difficult, both for satellites that are ejected as well as for those that remain bound. For example, the massive member of the late−accreting pair in Figure 34 sees its apocenter reduced by more than a factor of ~ 5 from its turnaround value in a single pericentric passage. Such dramatic variations in orbital energy are difficult to reproduce with simple analytic treatments inspired on Chandrasekhar's dynamical friction formula (Peñarrubia 2007, private communication).

5.4 Application to the Local Group

We may apply these results to the interpretation of kinematical outliers within the satellite population around the Milky Way (MW) and M31, the giant spirals in the Local Group. Although part of the discussion that follows is slightly speculative due to lack of suitable data on the three−dimensional orbits of nearby satellites, we feel that it is important to highlight the role that the concomitant accretion of multiple satellites may have played in shaping the dynamics of the dwarf members in the Local Group.

5.4.1 *Milky Way satellites*

The filled squares in Figure 35 show the galactocentric radial velocity of thirteen bright satellites around the Milky Way and compare them with the simulated satellite population. This comparison requires a choice for the virial radius and virial velocity of the Milky Way, which are observationally poorly constrained. We will assume the estimations we found in Chapter 4 based on the observed velocity dispersions of dwarf galaxies within 300 kpc region from the Galaxy: $V_{\rm vir}^{\rm MW} = 109 \pm 22$ km/s and $r_{\rm vir}^{\rm MW} = 237 \pm 50$ kpc.

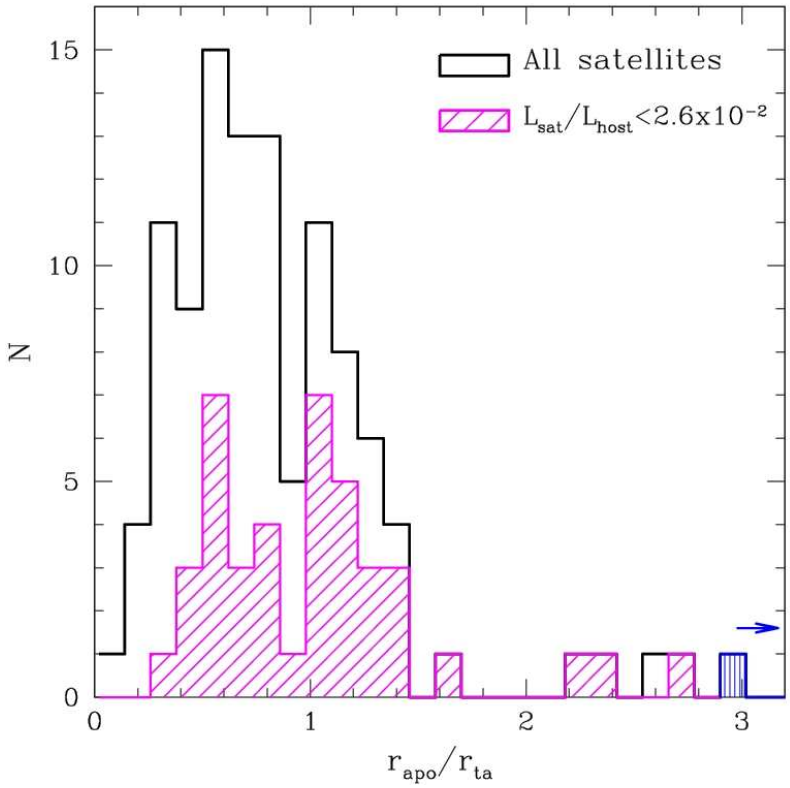

Figure 36. Distribution of the ratio between the apocentric radius of satellites (measured at $z = 0$) and their turnaround radius, defined as the maximum distance to the primary before accretion. Note the presence of two groups. Satellites on "conventional" orbits have $r_{apo}/r_{ta} < 1$, the rest have been catapulted into high−energy orbits by three−body interactions during first approach. The satellite marked with a rightward arrow is the "escaping" satellite identified by a dot−centered circle in Figure 35; this system has nominally infinite r_{apo}. The dashed histogram highlights the population of low−mass satellites; i.e., those with stellar masses at accretion time not exceeding 2.6% of the primary's final M_{str}. The satellite marked with an arrow is a formal "escaper" for which r_{apo} cannot be computed.

Figure 35 shows that, with this choice, the velocities and positions of all MW satellites are reasonably consistent with the simulated satellite population, with the possible exception of Leo I, which is located near the virial radius and is moving outward with a velocity clearly exceeding V_{vir}. Indeed, for $V_{vir}^{MW} = 109$ km/s, Leo I lies right on the escape velocity curve of an NFW profile with concentration parameter similar to those measured in the simulations. This is clearly a kinematical outlier reminiscent of the satellite expelled by three−body interactions discussed in the previous subsection and identified by a dot−centered circle in Figure 35. This is the *only* "associated" satellite in our simulations with radial velocity exceeding V_{vir} and located outside r_{vir}.

Could Leo I be a satellite that has been propelled into a highly−energetic orbit through a three−body interaction? If so, there are a number of generic predictions that might be possible to verify observationally. One is that its orbit must be now basically radial in the rest frame of the Galaxy, although it might be some time before proper motion studies are able to falsify this prediction. A second possibility is to try and identify the second member of the pair to which it belonged. An outward moving satellite on a radial orbit takes only $\sim 2-3$ Gyr to reach r_{vir} with escape velocity. Coincidentally, this is about the time that the Magellanic Clouds pair were last at pericenter, according to the traditional orbital evolution of the Clouds (see, e.g. Gardiner & Noguchi 1996; van der Marel et al. 2002).

Could Leo I have been a Magellanic Cloud satellite ejected from the Galaxy a few Gyrs ago? Since most satellites that are ejected do so during *first* pericentric approach, this would imply that the Clouds were accreted only recently into the Galaxy, so that they reached their first pericentric approach just a few Gyr ago. This is certainly in the spirit of the re−analysis of the orbit of the Clouds presented recently by Besla et al. (2007) and based on new proper motion measurements recently reported by Kallivayalil et al. (2006) . In this regard, the orbit of the Clouds might resemble the orbit of the companion of the "escaping" satellite located next to Leo I in Figure 35. The companion is fairly massive and, despite a turnaround radius of almost ~ 600 kpc and a rather late accretion time ($t_{acc} = 10.5$ Gyr, see Figure 34), it is left after pericenter on a tightly bound, short−period orbit resembling that of the Clouds today (Gardiner & Noguchi 1996; van der Marel et al. 2002). To compound the resemblance, this satellite has, at accretion time, a total luminosity of order $\sim 10\%$ of that of the primary, again on a par with the Clouds.

We also note that an ejected satellite is likely to have picked up its extra orbital energy through a rather close pericentric passage and that this may have led to substantial tidal damage. This, indeed, has been argued recently by Sohn et al. (2006) on the basis of asymmetries in the spatial and velocity distribution of Leo I giants (but see Koch et al. 2007 for a radically different interpretation).

On a final note, one should not forget to mention another (less exciting!) explanation for Leo I: that our estimate of V_{vir}^{MW} is a substantial underestimate of the true virial velocity of the Milky Way. The arrows in Figure 35 indicate how the position of the MW satellites in this plane would change if our estimate of V_{vir}^{MW} is varied by $\pm 20\%$. Increasing V_{vir}^{MW} by $\sim 20\%$ or more would make Leo I's kinematics less extreme, and closer to what would be expected for a high−speed satellite completing its first orbit.

This rather more prosaic scenario certainly cannot be discounted on the basis of available data (see, e.g., Zaritsky et al 1989, Kochanek 1996, Wilkinson & Evans 1999).

5.4.2 *M31 satellites*

A similar analysis may be applied to M31 by using the projected distances and line−of−sight velocities of simulated satellites, shown in Figure 37. Three orthogonal projections of the simulated satellites are overlapped in this figure, with symbols as defined in Figure 35. Following the same approach as in § 5.4.1, we use the fact that the line−of−sight satellite velocity dispersion is $\sigma_{los} \sim 0.8(\pm 0.2)\, V_{vir}$ in our simulations to guide our choice of virial velocity and radius for M31; $V_{vir}^{M31} = 138 \pm 35$ km/s and $r_{vir}^{M31} = 300 \pm 76$ kpc. (We obtain $\sigma_{los} = 111$ km/s for all 17 satellites within 300 kpc of M31.) This compares favourably with the $V_{vir}^{M31} \sim 120$ km/s estimate recently obtained by Seigar et al. (2006) under rather different assumptions.

With this choice, we show the 19 satellites around M31 compiled by McConnachie & Irwin (2006), plus two recently−discovered satellites for which positions and radial velocities have become available (And XII, Chapman et al 2007, and And XIV, Majewski et al. 2007). As in Figure 35, arrows indicate how the position of M31 satellites would change in this figure if V_{vir}^{M31} were allowed to vary by $\pm 20\%$. Note that projected distances are as if viewed from infinity along the direction joining the Milky Way with M31 and that the *sign* of the line−of−sight velocity in Figure 37 is chosen to be positive if the satellite is receding from the primary (in projection) and negative otherwise.

There are a few possible outliers in the distribution of M31 satellite velocities: And XIV (Majewski et al 2007), the Pegasus dwarf irregular (UGC 12613, Gallagher et al. 1998), And XII (Chapman et al 2007), and UGCA 092 (labelled U092 in Figure 37, McConnachie & Irwin 2006). And XIV and PegDIG seem likely candidates for the three−body "ejection" mechanism discussed above: they have large velocities for their position, and, most importantly, they are receding from M31; a *requirement* for an escaping satellite. Note, for example, that And XIV lies very close to the "escaping" satellite (dot−centered symbol in Figure 37) paired to Leo I in the previous subsection. Escapers should move radially away from the primary, and they would be much harder to detect in projection as extreme velocity objects, unless they are moving preferentially along the line of sight. It is difficult to make this statement more conclusive without further knowledge of the orbital paths of these satellites. Here, we just note, in agreement with Majewski et al (2007), that whether And XIV and PegDIG are dynamical "rogues" depends not only on the (unknown) transverse velocity of these galaxies, but also on what is assumed for M31's virial velocity. With our assumed $V_{vir}^{M31} = 138$ km/s, neither And XIV nor PegDIG look completely out of place in Figure 37; had we assumed the lower value of 120 km/s advocated by Seigar et al (2006) And XIV would be almost on the NFW escape velocity curve, and would certainly be a true outlier.

High−velocity satellites *approaching* M31 in projection are unlikely to be escapers, but rather satellites on their first approach. This interpretation is probably the most

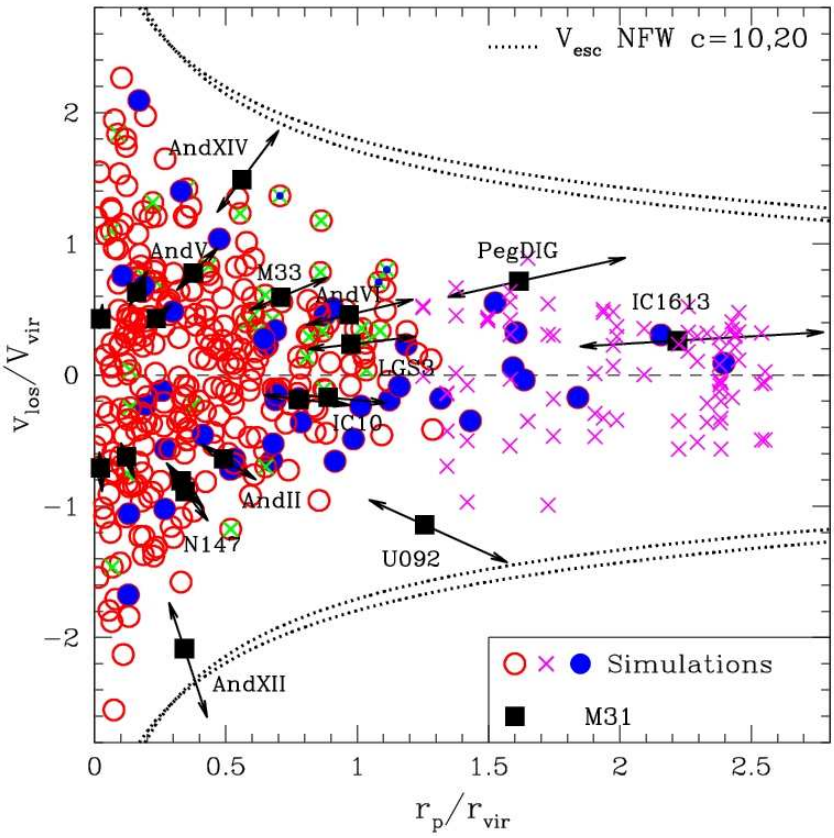

Figure 37. As Figure 35 but for *line–of–sight* velocities and *projected* distances. Three random orthogonal projections have been chosen for each simulated satellite system. Signs for V_{los} have been chosen so that it is positive if the satellite is receding away from the primary in projection, negative otherwise. The "escaping" satellite from Figure 35 is shown by a starred symbol. Filled squares correspond to the M31 satellites taken from McConnachie & Irwin 2006, plus And XIV (Majewski et al. 2007) and And XII (Chapman et al 2007, submitted) and assuming that $V_{vir}^{M31} \sim 138$ km/s and $r_{vir}^{M31} = 300$ kpc. Arrows indicate how the positions of M31 satellites in this plot would be altered if our estimate of V_{vir}^{M31} (and, consequently, r_{vir}^{M31}) is allowed to vary by 20%.

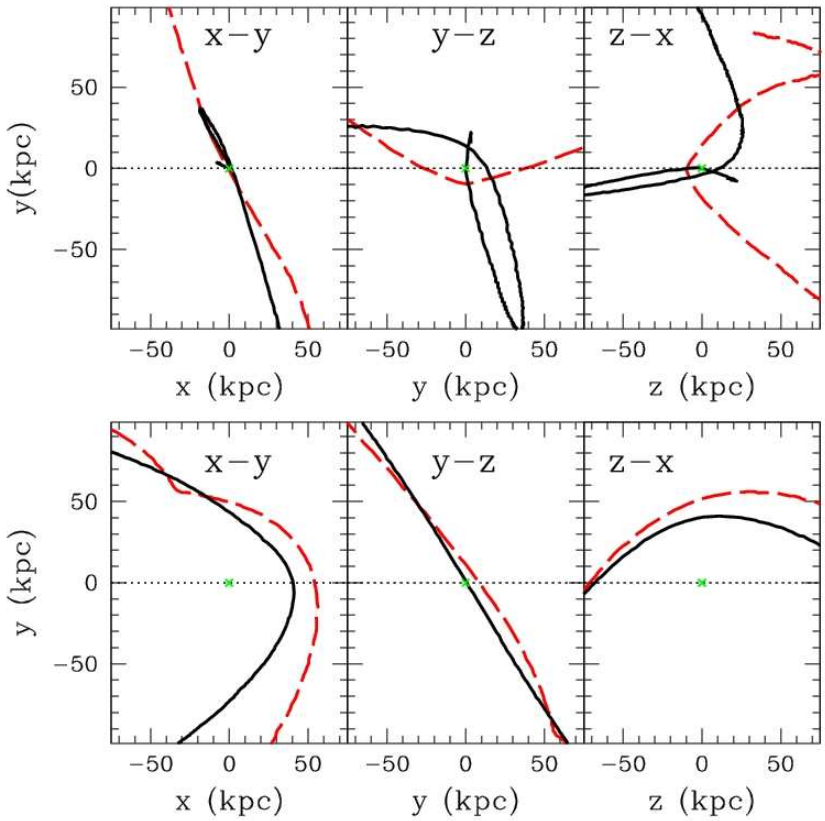

Figure 38. Orbital paths for both pair of satellites shown in Figure 34. Upper (bottom) panels show the pair that accretes later (earlier) in that figure and show its orbit in the rest frame of the primary. The coordinate system is chosen so that the angular momentum of the primary is aligned with the z axis. A solid curve tracks the path of the heavier satellite; a dashed line follows the satellite that is propelled into a highly energetic orbit after.

appropriate for And XII and UGCA 092. As discussed by Chapman et al (2007), And XII is almost certainly *farther* than M31 but is approaching us at much higher speed (~ 281 km/s faster) than M31. This implies that And XII is actually getting closer in projection to M31 (hence the negative sign assigned to its V_{los} in Figure 37), making the interpretation of this satellite as an escaping system rather unlikely.

Note, again, that although And XII (and UGCA 092) are just outside the loci delineated by simulated satellites in Figure 37, revising our assumption for V_{vir}^{M31} upward by 20% or more would render the velocity of this satellite rather less extreme, and would make it consistent with that of a satellite on its first approach to M31. As was the case for Leo I, this more prosaic interpretation of the data is certainly consistent with available data.

5.5 Conclusions of this Chapter

We examine the orbits of satellite galaxies in a series of Nbody/gasdynamical simulations of the formation of L_* galaxies in a ΛCDM universe. Most satellites follow orbits roughly in accord with the expectations of secondary infall−motivated models. Satellites initially follow the universal expansion before being decelerated by the gravitational pull of the main galaxy, turning around and accreting onto the main galaxy. Their apocentric radii decrease steadily afterwards as a result of the mixing associated with the virialization process as well as of dynamical friction. We find in the previous Chapter that, at $z = 0$ most satellites associated with the primary are found within its virial radius, and show little spatial or kinematic bias relative to the dark matter component.

A number of satellites, however, are on rather unorthodox orbits, with present apocentric radii exceeding their turnaround radii, at times by a large factor. The apocenters of these satellites are typically beyond the virial radius of the primary; one satellite is formally "unbound", whereas another is on an extreme orbit and is found today more than $2.5\, r_{vir}$ away, or $\geqslant 600$ kpc when scaling this result to the Milky Way.

These satellites owe their extreme orbits to three−body interactions during first approach: they are typically the lighter member of a pair of satellites that is disrupted during their first encounter with the primary. This process has affected a significant fraction of satellites: a full one−third of the simulated satellite population identified at $z = 0$ have apocentric radii exceeding their turnaround radii. These satellites make up the majority (63%) of systems on orbits that venture outside the virial radius.

We speculate that some of the kinematical outliers in the Local Group may have been affected by such process. In particular, Leo I might have been ejected $2 - 3$ Gyr ago, perhaps as a result of interactions with the Milky Way and the Magellanic Clouds. Other satellites on extreme orbits in the Local Group may have originated from such mechanism. Cetus and Tucana—two dwarf spheroidals in the periphery of the Local Group—may owe their odd location (most dSphs are found much closer to either M31 or the Galaxy) to such ejection mechanism.

If this is correct, the most obvious culprits for such ejection events are likely to be the largest satellites in the Local Group (M31 and the LMC/SMC), implying that their possible role in shaping the kinematics of the Local Group satellite population should

be recognized and properly assessed. In this regard, the presence of kinematical oddities in the population of M31 satellites, such as the fact that the majority of them lie on "one side" of M31 and seem to be receding away from it (McConnachie & Irwin 2006), suggest the possibility that at least some of the satellites normally associated with M31 might have actually been brought into the Local Group fairly recently by M33. Note, for example, that two of the dynamical outliers singled out in our discussion above (And XII and And XIV) are close to each other in projection; have rather similar line-of-sight velocities (in the heliocentric frame And XII is approaching us at 556 km/s, And XIV at 478 km/s); and belong to a small subsystem of satellites located fairly close to M33.

The same mechanism might explain why the spatial distribution of at least some satellites, both around M31 and the Milky Way, seem to align themselves on a "planar" configuration (Majewski 1994; Libeskind et al. 2005; Koch & Grebel 2006) , as this may just reflect the orbital accretion plane of a multiple system of satellites accreted simultaneously in the recent past (Kroupa et al. 2005; Metz et al. 2007) .

From the point of view of hierarchical galaxy formation models, it would be rather unlikely for a galaxy as bright as M33 to form in isolation and to accrete as a single entity onto M31. Therefore, the task of finding out *which* satellites (rather than *whether*) have been contributed by the lesser members of the Local Group, as well as what dynamical consequences this may entail, should be undertaken seriously, especially now, as new surveys begin to bridge our incomplete knowledge of the faint satellites orbiting our own backyard.

6

GENERAL CONCLUSIONS

Studies of satellites are a very powerful tool of galaxy formation models. Whether satellites merge with the host or survive until the present, they provide valuable insights on: i) the dark matter distribution of host halos, ii) the mass surrounding isolated galaxies, iii) the accretion and disruption events that characterized the history of their primaries in the past. In this Thesis we study the role of satellites during the formation process of galaxies using both numerical simulations and semi−analytic models. We provide robust predictions for the relation between the satellite population and the (dark and luminous) halos of the host galaxy.

We have analyzed the evolution of the satellite galaxy populations around L_* primaries using a suite of N−body/gasdynamical simulations. We find that after entering the virial radius of the host, the masses and orbits of satellites are substantially altered; in some cases driving their final disruption by tides. This naturally split the sample into a *merged* and a *surviving* satellite population. Our results highlight the differences between both: *merged* satellites were on average more massive, were accreted earlier and on more eccentric orbits than the *surviving* counterparts. The bulk of the stellar halo stars in a galaxy is brought by these *merged* satellites, predicting that satellites that remain self−bound until the present are dynamically distinct from halo stars.

On the other hand, using numerical simulations we find that *surviving* satellites are fairly good tracers of the dark matter spatial distribution of host halos. Satellites follow an NFW profile that matches that of the dark matter particles for distances larger than $0.2r_{vir}$. Moreover, these findings are in good agreement with our analysis of satellite radial distributions in the semi−analytical catalog of galaxies from the *Millennium Run* simulation. This suggests that satellites are our most reliable tracer of the external regions of host halos and we aim to apply this idea on observational samples. We find that *in projection*, the satellite radial distribution in simulations is well fitted by a power law of slope $\alpha \sim -1.5$. This was compared to a sample of satellite galaxies selected from the Sloan DR4 catalog finding $\alpha \sim -1.4$, in reasonable agreement with theoretical predictions.

Our results show that the kinematics of satellites is also a good indicator of the velocities of the host dark halo. The orbits of surviving satellites approximately reproduce those of dark matter particles and substantially differ from that of the stellar halo stars. This is a result of the stellar halo build−up process that, as above mentioned, is based on the preferential accretion of satellites in eccentric orbits. The satellite velocity dispersions can be used to infer the virial velocity of the hosts according to: $\sigma_{sat}/V_{vir} = 0.9 \pm 0.2$. Applied to the Local Group galaxies and their dwarfs this gives: $V_{vir}^{MW} \sim 109 \pm 22$ km/s and $V_{vir}^{M31} \sim 138 \pm 35$ km/s for the Milky Way

and Andromeda galaxy respectively. These values are in good agreement with recent estimates from the literature and suggest that the virial velocities of galaxies might be substantially lower than the rotation speed of their disk components (contrary to the expectations from current semi−analytical modelling).

A closer inspection to the *surviving* satellite kinematic reveals a small (1/3), but non−negligible population of objects on unorthodox orbits. These extreme orbits are characterized by apocenters that exceed their turnaround radius, some times associated with high−speed motions. This puzzling population of satellites consists typically of the faint member of a pair that was expelled onto their highly energetic orbits as a result of three−body interaction mechanisms during the first pericenter approach to the primary. We speculate that processes of this type might have been involved in some dwarfs of the Local Group, such as LeoI, the isolated Cetus and Tucana as well as the newly−discovered high−speed satellites around Andromeda: AndXII and AndXIV. Our results suggest that care must be exercised when using the orbits of the most weakly bound satellites to place constrains on the total mass of the Local Group.

Satellite galaxies are indispensable pieces in our hierarchical picture of galaxy formation. They play a major role either as "building−blocks" if they merge, or as "lighthouses" if they survive, guiding our understanding of the external regions of dark halos. We find also an extra population: those that escape the systems revealing that, sometimes, they also interact with their siblings. Data from many observational programs are coming in the next future, all aimed at carefully surveying our Galaxy. The interplay between numerical models and observations becomes fundamental in order to improve our understanding of how galaxies form and evolve. Each satellite has a story to tell, it is up to us to listen to them.

BIBLIOGRAPHY

[1] Abadi M. G., Navarro J. F., Steinmetz M., 2006, MNRAS, 365, 747

[2] Abadi M. G., Navarro J. F., Steinmetz M., Eke V. R., 2003a, ApJ, 591, 499

[3] Abadi M. G., Navarro J. F., Steinmetz M., Eke V. R., 2003b, ApJ, 597, 21

[4] Adelman-McCarthy J. K., Agüeros M. A., Allam S. S., Anderson K. S. J., Anderson S. F., Annis J., Bahcall N. A., and 135 coauthors 2006, ApJS, 162, 38

[5] Agustsson I., Brainerd T. G., 2006, ApJL, 644, L25

[6] Athanassoula E., Fady E., Lambert J. C., Bosma A., 2000, MNRAS, 314, 475

[7] Azzaro M., Zentner A. R., Prada F., Klypin A. A., 2006, ApJ, 645, 228

[8] Bahcall N. A., 1973, ApJ, 186, 1179

[9] Bailin J., Steinmetz M., 2005, ApJ, 627, 647

[10] Balogh M. L., Navarro J. F., Morris S. L., 2000, ApJ, 540, 113

[11] Barnes J., Efstathiou G., 1987, ApJ, 319, 575

[12] Battaglia G., Helmi A., Morrison H., Harding P., Olszewski E. W., Mateo M., Freeman K. C., Norris J., Shectman S. A., 2005, MNRAS, 364, 433

[13] Baugh C. M., 2006, Reports of Progress in Physics, 69, 3101

[14] Bell E. F., de Jong R. S., 2001, ApJ, 550, 212

[15] Bellazzini M., Newberg H. J., Correnti M., Ferraro F. R., Monaco L., 2006, A&A, 457, L21

[16] Belokurov V., Zucker D. B., Evans N. W., Kleyna J. T., Koposov S., Hodgkin S. T., Irwin M. J., and 27 coauthors 2007, ApJ, 654, 897

[17] Belokurov V., Zucker D. B., Evans N. W., Wilkinson M. I., Irwin M. J., Hodgkin S., Bramich D. M., and 26 coauthors 2006, ApJL, 647, L111

[18] Benson A. J., Frenk C. S., Sharples R. M., 2002, ApJ, 574, 104

[19] Bertschinger E., 1985, ApJS, 58, 39

[20] Besla G., Kallivayalil N., Hernquist L., Robertson B., Cox T. J., van der Marel R. P., Alcock C., 2007, ArXiv Astrophysics e-prints

[21] Binney J., Tremaine S., 1987, Galactic dynamics. Princeton, NJ, Princeton University Press, 1987, 747 p.

[22] Bower R. G., Benson A. J., Malbon R., Helly J. C., Frenk C. S., Baugh C. M., Cole S., Lacey C. G., 2006, MNRAS, 370, 645

[23] Brainerd T. G., 2004a, ArXiv Astrophysics e-prints

[24] Brainerd T. G., 2004b, in Allen R. E., Nanopoulos D. V., Pope C. N., eds, AIP Conf. Proc. 743: The New Cosmology: Conference on Strings and Cosmology Vol. 743 of American Institute of Physics Conference Series, Constraints on Field Galaxy Halos from Weak Lensing and Satellite Dynamics. pp 129–156

[25] Brainerd T. G., 2005, ApJL, 628, L101

[26] Bryan G. L., Norman M. L., 1998, ApJ, 495, 80

[27] Bullock J. S., Johnston K. V., 2005, ApJ, 635, 931

[28] Bullock J. S., Kravtsov A. V., Weinberg D. H., 2000, ApJ, 539, 517

[29] Chapman S. C., Ibata R., Lewis G. F., Ferguson A. M. N., Irwin M., McConnachie A., Tanvir N., 2006, ApJ, 653, 255

[30] Chen J., Kravtsov A. V., Prada F., Sheldon E. S., Klypin A. A., Blanton M. R., Brinkmann J., Thakar A. R., 2006, ApJ, 647, 86

[31] Colless M., Dalton G., Maddox S., Sutherland W., Norberg P., Cole S., Bland-Hawthorn J., and 22 coauthors 2001, MNRAS, 328, 1039

[32] Colpi M., Mayer L., Governato F., 1999, ApJ, 525, 720

[33] Croton D. J., Springel V., White S. D. M., De Lucia G., Frenk C. S., Gao L., Jenkins A., Kauffmann G., Navarro J. F., Yoshida N., 2006, MNRAS, 365, 11

[34] De Lucia G., Kauffmann G., Springel V., White S. D. M., Lanzoni B., Stoehr F., Tormen G., Yoshida N., 2004, MNRAS, 348, 333

[35] Diemand J., Kuhlen M., Madau P., 2007, ApJ, 657, 262

[36] Diemand J., Madau P., Moore B., 2005, MNRAS, 364, 367

[37] Diemand J., Moore B., Stadel J., 2004, MNRAS, 352, 535

[38] Dinescu D. I., Girard T. M., van Altena W. F., López C. E., 2005, ApJL, 618, L25

[39] Dinescu D. I., Martínez-Delgado D., Girard T. M., Peñarrubia J., Rix H.-W., Butler D., van Altena W. F., 2005, ApJL, 631, L49

[40] D'Onghia E., Sommer-Larsen J., Romeo A. D., Burkert A., Pedersen K., Portinari L., Rasmussen J., 2005, ApJL, 630, L109

[41] Eggen O. J., 1996, AJ, 112, 1595

[42] Eke V. R., Baugh C. M., Cole S., Frenk C. S., Navarro J. F., 2006, MNRAS, 370, 1147

[43] Evans N. W., Wilkinson M. I., 2000, MNRAS, 316, 929

[44] Faltenbacher A., Diemand J., 2006, MNRAS, 369, 1698

[45] Faria D., Feltzing S., Lundström I., Gilmore G., Wahlgren G. M., Ardeberg A., Linde P., 2007, A&A, 465, 357

[46] Ferguson A. M. N., Irwin M. J., Ibata R. A., Lewis G. F., Tanvir N. R., 2002, AJ, 124, 1452

[47] Fillmore J. A., Goldreich P., 1984, ApJ, 281, 1

[48] Font A. S., Johnston K. V., Bullock J. S., Robertson B. E., 2006a, ApJ, 638, 585

[49] Font A. S., Johnston K. V., Bullock J. S., Robertson B. E., 2006b, ApJ, 646, 886

[50] Fuhrmann K., 1998, A&A, 338, 161

[51] Fukushige T., Makino J., 2001, ApJ, 557, 533

[52] Gallagher J. S., Tolstoy E., Dohm-Palmer R. C., Skillman E. D., Cole A. A., Hoessel J. G., Saha A., Mateo M., 1998, AJ, 115, 1869

[53] Gao L., De Lucia G., White S. D. M., Jenkins A., 2004, MNRAS, 352, L1

[54] Gao L., White S. D. M., Jenkins A., Stoehr F., Springel V., 2004, MNRAS, 355, 819

[55] Gardiner L. T., Noguchi M., 1996, MNRAS, 278, 191

[56] Ghigna S., Moore B., Governato F., Lake G., Quinn T., Stadel J., 1998, MNRAS, 300, 146

[57] Ghigna S., Moore B., Governato F., Lake G., Quinn T., Stadel J., 2000, ApJ, 544, 616

[58] Gilbert K. M., Guhathakurta P., Kalirai J. S., Rich R. M., Majewski S. R., Ostheimer J. C., Reitzel D. B., Cenarro A. J., Cooper M. C., Luine C., Patterson R. J., 2006, ApJ, 652, 1188

[59] Gill S. P. D., Knebe A., Gibson B. K., 2005, MNRAS, 356, 1327

[60] Gilmore G., Wyse R. F. G., 1998, AJ, 116, 748

[61] Gnedin N. Y., 2000, ApJ, 542, 535

[62] Gnedin O. Y., Weinberg D. H., Pizagno J., Prada F., Rix H.-W., 2006, ArXiv Astrophysics e-prints

[63] Gott J. R. I., 1975, ApJ, 201, 296

[64] Guhathakurta P., Rich R. M., Reitzel D. B., Cooper M. C., Gilbert K. M., Majewski S. R., Ostheimer J. C., Geha M. C., Johnston K. V., Patterson R. J., 2006, AJ, 131, 2497

[65] Gunn J. E., 1977, ApJ, 218, 592

[66] Gunn J. E., Gott J. R. I., 1972, ApJ, 176, 1

[67] Harbeck D., Grebel E. K., Holtzman J., Guhathakurta P., Brandner W., Geisler D., Sarajedini A., Dolphin A., Hurley-Keller D., Mateo M., 2001, AJ, 122, 3092

[68] Hartwick F. D. A., 2000, AJ, 119, 2248

[69] Hayashi E., Navarro J. F., Taylor J. E., Stadel J., Quinn T., 2003, ApJ, 584, 541

[70] Helmi A., Navarro J. F., Meza A., Steinmetz M., Eke V. R., 2003, ApJL, 592, L25

[71] Hernquist L., 1993, ApJS, 86, 389

[72] Ibata R., Chapman S., Ferguson A. M. N., Lewis G., Irwin M., Tanvir N., 2005, ApJ, 634, 287

[73] Ibata R., Irwin M., Lewis G., Ferguson A. M. N., Tanvir N., 2001, Nature, 412, 49

[74] Ibata R. A., Gilmore G., Irwin M. J., 1994, Nature, 370, 194

[75] Irwin M. J., Belokurov V., Evans N. W., Ryan-Weber E. V., de Jong J. T. A., Koposov S., Zucker D. B., and 20 coauthors 2007, ApJL, 656, L13

[76] Jing Y. P., Suto Y., 2000, ApJL, 529, L69

[77] Jing Y. P., Suto Y., 2002, ApJ, 574, 538

[78] Johnston K. V., Sigurdsson S., Hernquist L., 1999, MNRAS, 302, 771

[79] Jones L. R., Ponman T. J., Horton A., Babul A., Ebeling H., Burke D. J., 2003, MNRAS, 343, 627

[80] Kallivayalil N., van der Marel R. P., Alcock C., Axelrod T., Cook K. H., Drake A. J., Geha M., 2006, ApJ, 638, 772

[81] Kashikawa N., Sekiguchi M., Doi M., Komiyama Y., Okamura S., Shimasaku K., Yagi M., Yasuda N., 1998, ApJ, 500, 750

[82] Kauffmann G., White S. D. M., Guiderdoni B., 1993, MNRAS, 264, 201

[83] Kawata D., Arimoto N., Cen R., Gibson B. K., 2006, ApJ, 641, 785

[84] Kazantzidis S., Mayer L., Mastropietro C., Diemand J., Stadel J., Moore B., 2004, ApJ, 608, 663

[85] Kennicutt Jr. R. C., 1998, ApJ, 498, 541

[86] Kleyna J. T., Wilkinson M. I., Evans N. W., Gilmore G., 2004, MNRAS, 354, L66

[87] Klypin A., Nolthenius R., Primack J., 1997, ApJ, 474, 533

[88] Klypin A., Zhao H., Somerville R. S., 2002, ApJ, 573, 597

[89] Knebe A., Gill S. P. D., Gibson B. K., Lewis G. F., Ibata R. A., Dopita M. A., 2004, ApJ, 603, 7

[90] Knebe A., Wießner V., 2006, Publications of the Astronomical Society of Australia, 23, 125

[91] Koch A., Grebel E. K., 2006, AJ, 131, 1405

[92] Koch A., Wilkinson M. I., Kleyna J. T., Gilmore G. F., Grebel E. K., Mackey A. D., Evans N. W., Wyse R. F. G., 2007, ApJ, 657, 241

[93] Kochanek C. S., 1996, ApJ, 457, 228

[94] Kravtsov A. V., Gnedin O. Y., Klypin A. A., 2004, ApJ, 609, 482

[95] Kroupa P., Theis C., Boily C. M., 2005, A&A, 431, 517

[96] Lewis G. F., Babul A., Katz N., Quinn T., Hernquist L., Weinberg D. H., 2000, ApJ, 536, 623

[97] Libeskind N. I., Frenk C. S., Cole S., Helly J. C., Jenkins A., Navarro J. F., Power C., 2005, MNRAS, 363, 146

[98] Little B., Tremaine S., 1987, ApJ, 320, 493

[99] Łokas E. L., 2001, MNRAS, 327, L21

[100] Lynden-Bell D., 1982, The Observatory, 102, 202

[101] Macciò A. V., Moore B., Stadel J., Diemand J., 2006, MNRAS, 366, 1529

[102] Majewski S. R., 1994, ApJL, 431, L17

[103] Majewski S. R., Beaton R. L., Patterson R. J., Kalirai J. S., Geha M. C., Muñoz R. R., Seigar M. S., Guhathakurta P., Bullock J., Rich R. M., Gilbert K. M., Reitzel D. B., 2007, ArXiv Astrophysics e-prints

[104] Martin N. F., Ibata R. A., Bellazzini M., Irwin M. J., Lewis G. F., Dehnen W., 2004, MNRAS, 348, 12

[105] Martin N. F., Ibata R. A., Irwin M. J., Chapman S., Lewis G. F., Ferguson A. M. N., Tanvir N., McConnachie A. W., 2006, MNRAS, 371, 1983

[106] Mateo M. L., 1998, ARA&A, 36, 435

[107] Mathews W. G., Chomiuk L., Brighenti F., Buote D. A., 2004, ApJ, 616, 745

[108] Mayer L., Governato F., Colpi M., Moore B., Quinn T., Wadsley J., Stadel J., Lake G., 2001a, ApJ, 559, 754

[109] Mayer L., Governato F., Colpi M., Moore B., Quinn T., Wadsley J., Stadel J., Lake G., 2001b, ApJL, 547, L123

[110] McConnachie A. W., Irwin M. J., 2006, MNRAS, 365, 902

[111] McConnachie A. W., Irwin M. J., Ibata R. A., Ferguson A. M. N., Lewis G. F., Tanvir N., 2003, MNRAS, 343, 1335

[112] McKay T. A., Sheldon E. S., Johnston D., Grebel E. K., Prada F., Rix H.-W., Bahcall N. A., Brinkmann J., Csabai I., Fukugita M., Lamb D. Q., York D. G., 2002, ApJL, 571, L85

[113] Metz M., Kroupa P., Jerjen H., 2007, MNRAS, 374, 1125

[114] Meza A., Navarro J. F., Abadi M. G., Steinmetz M., 2005, MNRAS, 359, 93

[115] Meza A., Navarro J. F., Steinmetz M., Eke V. R., 2003, ApJ, 590, 619

[116] Mohayaee R., Colombi S., Fort B., Gavazzi R., Shandarin S., Touma J., 2006, in Mamon G. A., Combes F., Deffayet C., Fort B., eds, EAS Publications Series Vol. 20 of EAS Publications Series, Caustics in dark matter haloes. pp 19–24

[117] Mohayaee R., Shandarin S. F., 2006, MNRAS, 366, 1217

[118] Moore B., 2001, in Spooner N. J. C., Kudryavtsev V., eds, Identification of Dark Matter Caustics and Cold Dark Matter. pp 93–+

[119] Moore B., Diemand J., Madau P., Zemp M., Stadel J., 2006, MNRAS, 368, 563

[120] Moore B., Ghigna S., Governato F., Lake G., Quinn T., Stadel J., Tozzi P., 1999, ApJL, 524, L19

[121] Moore B., Kazantzidis S., Diemand J., Stadel J., 2004, MNRAS, 354, 522

[122] Muñoz R. R., Majewski S. R., Zaggia S., Kunkel W. E., Frinchaboy P. M., Nidever D. L., Crnojevic D., Patterson R. J., Crane J. D., Johnston K. V., Sohn S. T., Bernstein R., Shectman S., 2006, ApJ, 649, 201

[123] Nagai D., Kravtsov A. V., 2005, ApJ, 618, 557

[124] Natarajan A., Sikivie P., 2005, PhRvD, 72, 083513

[125] Navarro J. F., Abadi M. G., Steinmetz M., 2004, ApJL, 613, L41

[126] Navarro J. F., Frenk C. S., White S. D. M., 1994, MNRAS, 267, L1+

[127] Navarro J. F., Frenk C. S., White S. D. M., 1996, ApJ, 462, 563

[128] Navarro J. F., Frenk C. S., White S. D. M., 1997, ApJ, 490, 493

[129] Navarro J. F., Helmi A., Freeman K. C., 2004, ApJL, 601, L43

[130] Navarro J. F., White S. D. M., 1993, MNRAS, 265, 271

[131] Newberg H. J., Yanny B., Rockosi C., Grebel E. K., Rix H.-W., Brinkmann J., Csabai I., Hennessy G., Hindsley R. B., Ibata R., Ivezić Z., Lamb D., Nash E. T., Odenkirchen M., Rave H. A., Schneider D. P., Smith J. A., Stolte A., York D. G., 2002, ApJ, 569, 245

[132] Peñarrubia J., Just A., Kroupa P., 2004, MNRAS, 349, 747

[133] Peñarrubia J., McConnachie A., Babul A., 2006, ApJL, 650, L33

[134] Peebles P. J. E., 1969, ApJ, 155, 393

[135] Peebles P. J. E., 1980, The large-scale structure of the universe. Research supported by the National Science Foundation. Princeton, N.J., Princeton University Press, 1980. 435 p.

[136] Penarrubia J., McConnachie A., Navarro J. F., 2007, ArXiv Astrophysics e-prints

[137] Piatek S., Pryor C., Bristow P., Olszewski E. W., Harris H. C., Mateo M., Minniti D., Tinney C. G., 2005, AJ, 130, 95

[138] Piatek S., Pryor C., Bristow P., Olszewski E. W., Harris H. C., Mateo M., Minniti D., Tinney C. G., 2006, AJ, 131, 1445

[139] Piatek S., Pryor C., Bristow P., Olszewski E. W., Harris H. C., Mateo M., Minniti D., Tinney C. G., 2007, AJ, 133, 818

[140] Piatek S., Pryor C., Olszewski E. W., Harris H. C., Mateo M., Minniti D., Tinney C. G., 2003, AJ, 126, 2346

[141] Pracy M. B., De Propris R., Driver S. P., Couch W. J., Nulsen P. E. J., 2004, MNRAS, 352, 1135

[142] Pracy M. B., Driver S. P., De Propris R., Couch W. J., Nulsen P. E. J., 2005, MNRAS, 364, 1147

[143] Prada F., Vitvitska M., Klypin A., Holtzman J. A., Schlegel D. J., Grebel E. K., Rix H.-W., Brinkmann J., McKay T. A., Csabai I., 2003, ApJ, 598, 260

[144] Pritzl B. J., Venn K. A., Irwin M., 2005, AJ, 130, 2140

[145] Reitzel D. B., Guhathakurta P., 2002, AJ, 124, 234

[146] Rich R. M., Reitzel D. B., Guhathakurta P., Gebhardt K., Ho L. C., 2004, AJ, 127, 2139

[147] Sakamoto T., Chiba M., Beers T. C., 2003, A&A, 397, 899

[148] Sales L., Lambas D. G., 2005, MNRAS, 356, 1045

[149] Searle L., Zinn R., 1978, ApJ, 225, 357

[150] Seigar M. S., Barth A. J., Bullock J. S., 2006, ArXiv Astrophysics e-prints

[151] Shetrone M., Venn K. A., Tolstoy E., Primas F., Hill V., Kaufer A., 2003, AJ, 125, 684

[152] Shetrone M. D., Côté P., Sargent W. L. W., 2001, ApJ, 548, 592

[153] Smith M. C., Ruchti G. R., Helmi A., Wyse R. F. G., Fulbright J. P., Freeman K. C., Navarro J. F., and 16 coauthors 2006, ArXiv Astrophysics e-prints

[154] Sohn S. T., Majewski S. R., Muñoz R. R., Kunkel W. E., Johnston K. V., Ostheimer J. C., Guhathakurta P., Patterson R. J., Siegel M. H., Cooper M. C., 2006, ArXiv Astrophysics e-prints

[155] Somerville R. S., Primack J. R., Faber S. M., 2001, MNRAS, 320, 504

[156] Sommer-Larsen J., 2006, MNRAS, 369, 958

[157] Spergel D. N., Bean R., Doré O., Nolta M. R., Bennett C. L., Dunkley J., Hinshaw G., and 15 coauthors 2006, ArXiv Astrophysics e-prints

[158] Spergel D. N., Verde L., Peiris H. V., Komatsu E., Nolta M. R., Bennett C. L., Halpern M., Hinshaw G., Jarosik N., Kogut A., Limon M., Meyer S. S., Page L., Tucker G. S., Weiland J. L., Wollack E., Wright E. L., 2003, ApJS, 148, 175

[159] Springel V., 2005, MNRAS, 364, 1105

[160] Springel V., White S. D. M., Jenkins A., Frenk C. S., Yoshida N., Gao L., Navarro J., Thacker R., Croton D., Helly J., Peacock J. A., Cole S., Thomas P., Couchman H., Evrard A., Colberg J., Pearce F., 2005, Nature, 435, 629

[161] Springel V., White S. D. M., Tormen G., Kauffmann G., 2001, MNRAS, 328, 726

[162] Steinmetz M., 1996, MNRAS, 278, 1005

[163] Steinmetz M., Navarro J. F., 2002, New Astronomy, 7, 155

[164] Stoehr F., White S. D. M., Tormen G., Springel V., 2002, MNRAS, 335, L84

[165] Strauss M. A., Weinberg D. H., Lupton R. H., Narayanan V. K., Annis J., Bernardi M., Blanton M., and 29 coauthors 2002, AJ, 124, 1810

[166] Strigari L. E., Bullock J. S., Kaplinghat M., 2007, ApJL, 657, L1

[167] Strigari L. E., Kaplinghat M., Bullock J. S., 2007, PhRvD, 75, 061303

[168] Taylor J. E., Babul A., 2001, ApJ, 559, 716

[169] Taylor J. E., Silk J., Babul A., 2005, in Jerjen H., Binggeli B., eds, IAU Colloq. 198: Near-fields cosmology with dwarf elliptical galaxies Clues to Dwarf galaxy Formation from Clustering and Kinematics. pp 185–188

[170] Tolstoy E., Irwin M. J., Helmi A., Battaglia G., Jablonka P., Hill V., Venn K. A., Shetrone M. D., Letarte B., Cole A. A., Primas F., Francois P., Arimoto N., Sadakane K., Kaufer A., Szeifert T., Abel T., 2004, ApJL, 617, L119

[171] Unavane M., Wyse R. F. G., Gilmore G., 1996, MNRAS, 278, 727

[172] van den Bergh S., 1999, A&ARv, 9, 273

[173] van den Bosch F. C., Weinmann S. M., Yang X., Mo H. J., Li C., Jing Y. P., 2005, MNRAS, 361, 1203

[174] van der Marel R. P., Alves D. R., Hardy E., Suntzeff N. B., 2002, AJ, 124, 2639

[175] Venn K. A., Irwin M., Shetrone M. D., Tout C. A., Hill V., Tolstoy E., 2004, AJ, 128, 1177

[176] Vitvitska M., Klypin A. A., Kravtsov A. V., Wechsler R. H., Primack J. R., Bullock J. S., 2002, ApJ, 581, 799

[177] Wang X., Woodroofe M., Walker M. G., Mateo M., Olszewski E., 2005, ApJ, 626, 145

[178] Warnick K., Knebe A., 2006, MNRAS, 369, 1253

[179] Weinberg D. H., Colombi S., Davé R., Katz N., 2006, ArXiv Astrophysics e-prints

[180] White S. D. M., Navarro J. F., Evrard A. E., Frenk C. S., 1993, Nature, 366, 429

[181] White S. D. M., Rees M. J., 1978, MNRAS, 183, 341

[182] Wilkinson M. I., Evans N. W., 1999, MNRAS, 310, 645

[183] Willman B., Dalcanton J. J., Martinez-Delgado D., West A. A., Blanton M. R., Hogg D. W., Barentine J. C., Brewington H. J., Harvanek M., Kleinman S. J., Krzesinski J., Long D., Neilsen Jr. E. H., Nitta A., Snedden S. A., 2005, ApJL, 626, L85

[184] Wojtak R., Łokas E. L., Gottlöber S., Mamon G. A., 2005, MNRAS, 361, L1

[185] Yang X., van den Bosch F. C., Mo H. J., Mao S., Kang X., Weinmann S. M., Guo Y., Jing Y. P., 2006, MNRAS, 369, 1293

[186] Yanny B., Newberg H. J., Grebel E. K., Kent S., Odenkirchen M., Rockosi C. M., Schlegel D., Subbarao M., Brinkmann J., Fukugita M., Ivezic Ž., Lamb D. Q., Schneider D. P., York D. G., 2003, ApJ, 588, 824

[187] Yepes G., Dominguez-Tenreiro R., del Pozo-Sanz R., 1991, ApJ, 373, 336

[188] York D. G., Adelman J., Anderson Jr. J. E., Anderson S. F., Annis J., Bahcall N. A., Bakken J. A., Barkhouser R., Bastian S., and 135 coauthors 2000, AJ, 120, 1579

[189] Zaritsky D., Olszewski E. W., Schommer R. A., Peterson R. C., Aaronson M., 1989, ApJ, 345, 759

[190] Zaritsky D., White S. D. M., 1994, ApJ, 435, 599

[191] Zhao H., 2004, MNRAS, 351, 891

[192] Zucker D. B., Belokurov V., Evans N. W., Wilkinson M. I., Irwin M. J., Sivarani T., Hodgkin S., and 26 coauthors 2006, ApJL, 643, L103

[193] Zucker D. B., Kniazev A. Y., Bell E. F., Martínez-Delgado D., Grebel E. K., Rix H.-W., Rockosi C. M., and 15 coauthors 2004, ApJL, 612, L121